BOSTON UNIVERSITY

GRADUATE SCHOOL OF ARTS AND SCIENCES

Dissertation

MORPHODYNAMICS OF SHALLOW COASTAL BAYS

by

GIULIO MARIOTTI

B.S., University of Florence (Italy), 2006
M.S., University of Florence (Italy), 2008

Submitted in partial fulfillment of the

requirements for the degree of

Doctor of Philosophy

2013

Approved by

First Reader _____

Sergio Fagherazzi, Ph.D.

Associate Professor of Earth Sciences

Second Reader _____

Guido D. Salvucci, Ph.D.

Professor of Earth Sciences

MORPHODYNAMICS OF SHALLOW COASTAL BAYS

(Order No.)

GIULIO MARIOTTI

Boston University School of Arts and Sciences, 2013

Major professor: Sergio Fagherazzi, Associate Professor of Earth Sciences

ABSTRACT

This thesis investigates the processes governing the hydro-morphodynamics of shallow coastal bays, through field investigations and numerical modeling. Particular attention is devoted to understand the coupling between three morphological units: salt marshes, tidal flats and tidal channels. This study demonstrates that sea level rise and sediment supply have a significant and complex control on the morphological evolution of coastal bays.

Erosive processes in the lagoons of Virginia Coast Reserve (VA) are explored through a detailed model for tidal currents and the dynamics of wind waves. The model reveals that both wave-induced erosion of the marsh boundary and tidal flat bed erosion increase with sea level rise. Both positive and negative feedbacks between wave energy at the boundaries and bottom shear stresses are predicted, depending on the fate of the sediments eroded from the salt marsh boundaries. A 1D morphological model for the coupled evolution of marshes and tidal flats shows that both an increase in sea level and

a decrease in sediment supply enhance marsh boundary erosion, suggesting that this erosion mechanism is a leading cause of marsh deterioration. In addtion, the model predicts that the scarp between salt marsh and tidal flat is a distinctive feature of marsh retreat, suggesting the use of this geometry as an indicator for ongoing erosion.

Field investigations in Willapa Bay (WA) shed light on the transport of water and sediments in a channel – tidal flat complex. During calm weather suspended sediment concentration is higher in the channel than on the tidal flat, leading to a sediment flux toward the latter, while the opposite flux occurs during stormy weather. A “two-points” dynamical model shows that the morphology of a costal bay stems from a dynamical equilibrium between currents in the channels and wind waves on the tidal flats. Because multiple equilibria are present, abrupt morphological changes can be triggered by small changes in wind regime, sea level or sediment supply.

Preface

Shallow coastal bays are characterized by extensive tidal flats and salt marshes, which provide habitats for a wide range of plant and animal species, improve water quality, and reduce erosion (Mitsch and Gosselink, 1986; Brampton, 1992). An understanding of the main physical processes governing these environments provides a tool for the prediction of morphological responses to environmental forcing (e.g. Vogel, 1994), and in particular, for quantifying the risk of erosion induced by Relative Sea Level Rise (RSLR).

Shallow costal bays are found in areas characterized by low energy settings. For example, they can be separated from the sea by barrier islands, which shelter them from the direct action of open sea processes. However, these environments can also form wherever there is a large supply of fine sediment irrespective of tidal range and wave conditions, for example close to major rivers' deltas (Woodroffe, 2003).

Tidal flats, which occupy a large part of many coastal bays, are sub-horizontal surfaces usually found below mean sea level, dissected by a network of channels. Salt marshes are vegetated surfaces usually found close to the highest astronomical tide level. Similar to tidal flats, they are dissected by a network of creeks which favors drainage.

Coastal bays are complex systems, where a variety of physical processes takes place. Stive et al. (1990) claimed that the morphodynamic behavior of a tidal basin is a degree more complex and less well understood than the one of uninterrupted coastlines and rivers. Tidal hydrodynamics are affected by the articulated structure of tidal channels

and flats, salt marshes and creeks. The distortion of the tidal signal in shallow water induces ebb-flood asymmetries, which influence net fluxes of water and sediments (Friedrichs and Aubrey, 1988). Residual circulations are presents between tidal channels and tidal flats (Li and O'Donnel, 2005). River discharge controls external sediment inputs and it affects currents and stratification (Banas et al., 2004). Wind waves, which depend on basin geometry, water level and wind characteristics, increase sediment resuspention and sediment fluxes (Green and Coco, 2007). In addition, sediment erodability in tidal flats depends on biological, and hence seasonal, factors, such as the presence of seagrass (Abdelrhman, 2007) and biofilms (Ruddy et al., 1998). Also, in salt marshes biota strongly interacts with sediment dynamics, affecting the morphology of intertidal landscapes (Le Hir et al., 2007). Finally, salt marsh boundaries are eroded by wind waves (Schwimmer and Pizzuto, 2000), and hence they constitute a sediment source for tidal flats and the marsh interior (van de Koppel et al., 2005; Yang et al., 2003).

Even if many aspects of coastal bays dynamics have been studied, a comprehensive understanding is not yet achieved, and the capability to predict their morphological evolution is still incomplete. The purpose of this thesis is to contribute to further developments in understanding the hydro-morphodynamics of coastal bays and to propose new conceptual and quantitative models for tidal flats and salt marsh morphological evolution at the long-term scale. In particular, this thesis aims to understand the effects of Relative Sea Level Rise (RSLR) on hydrodynamics (i.e. currents and waves), sediment transport, and eventually basin morphology. In order to

fulfill these goals, a combined use of numerical modeling and field investigations is undertaken.

The present dissertation consists of four chapters. These chapters are manuscripts that are either published or submitted to peer-reviewed scientific journals, and therefore they have only been altered in order to fit the format and regulations of dissertations filed with Boston University Graduate School of Arts and Sciences.

Chapter 1 focuses on wind waves in shallow lagoons. A detailed model for wind waves's dynamics, WWTM2D (Carinello et al., 2005), is applied to the lagoon of the Virginia Coast Reserve (VA). Measured wind waves are used to validate the model. Model simulations are then used to predict the effects of RSLR on the two major wave-induced erosive processes in tidal lagoons: tidal flat bed erosion and marsh boundary retreat.

Chapter 2 presents a coupled eco-hydro-morphodynamics model for tidal flats and salt marshes. The model takes into account the sediment exchange between these different compartments, and simulates the process of salt marsh boundary erosion. The model is used to explore the effect of RLSR and changes in sediment supply on tidal flat and salt marsh long-term morphological evolution.

Chapter 3 focuses on tidal current dynamics and sediment fluxes on tidal channels and tidal flats, based on an extensive field measurement campaign in the mudflat of Willapa Bay (WA). This study explores the interactions between tidal channels and tidal flats, and specifically the sediment exchange between these two units.

Finally, Chapter 4 describes a “two-points” morphological model for the coupled evolution of channels and tidal flats under the combined effects of tides and waves. Dynamical system tools are used to reveal the system equilibria and the bifurcations induced by changes in the control parameters: RSLR, sediment availability, and wind regime.

Final remarks are presented at the end of thesis, which is closed by a compiled reference list, including the references for this Preface and all the chapters.

Table of Contents

List of Tables

List of Figures

Chapter 1. Influence of storm surges and sea level on shallow tidal basin erosive processes

The contents of this chapter were published in 2010 in Journal of Geophysical Research – Oceans. This paper was co-authored with S. Fagherazzi (Department of Earth Science, Boston University), P. L. Wiberg, K. J. McGlathery, (Department of Environmental Sciences, University of Virginia), L. Carniello, and A. Defina (Department IMAGE, University of Padova, Italy).

Abstract

The finite-element model WWTM is applied to a system of lagoons at the Virginia Coast Reserve, USA. The model solves the shallow water equations to compute tidal fluxes, and is equipped with a wave propagation module to calculate wave height during local wind events. The model is validated using measured water elevations, wave heights, and periods at five locations within the lagoon system. Scenarios with different wind conditions, storm surges, and relative sea level are simulated. Results are analyzed in terms of bottom shear stresses on the tidal flats, a measure of sediment resuspension potential, and total wave energy impacting the marsh boundaries, which is the chief process driving lateral marsh erosion. Results indicate that wave energy at the marsh boundaries is more sensitive to wind direction than are bottom shear stresses. Wave energy on marsh boundaries and bottom shear stresses on the tidal flats increase with

sea level elevation, with the former increasing almost ten times more than the latter. Both positive and negative feedbacks between wave energy at the boundaries and bottom shear stresses are predicted, depending on the fate of the sediments eroded from the salt marsh boundaries.

1.1 Introduction

Wind waves are critical for the morphological and ecological equilibrium of shallow tidal basins. Two distinct erosional mechanisms are associated with wind waves. Wave-generated shear stresses, combined with tidal currents, are the main mechanism responsible for sediment resuspension on tidal flats (Carniello et al., 2005; Fagherazzi et al., 2006; Fagherazzi et al., 2007; Marani et al., 2007), and regulate both sediment concentration in the water column (and hence light availability at the bed, e.g. Lawson et al., 2007) and sediment export to salt marshes and to the ocean (Mariotti and Fagherazzi, 2010). Waves impacting salt marsh boundaries produce intermittent forces that promote marsh edge erosion and salt marsh regression. Even though marsh boundary erosion is a complex geotechnical problem that is dependent on a variety of processes (unsaturated filtration, root effects, soil characteristics, bioturbation), evidence shows that waves are the chief driver (Schwimmer, 2001; Moeller 1996; 1999).

Measurements of waves inside shallow tidal basins are generally rare; therefore a direct statistical analysis of the wave climate is seldom possible. A more profitable approach is to model wave fields as a function of forcing parameters, such as tidal elevation and

wind characteristics, that are more readily available. In addition, by using a model-based approach we can estimate the wave regime response to changes in forcing factors, such as sea level oscillations or variations in storminess (e.g. Fagherazzi and Wiberg 2009).

Wave generation depends on the transfer of energy from the wind to the water surface, which is a function of wind characteristics (duration, direction and speed), water depth, and fetch (the unobstructed distance over which the wind can blow). Fetch itself is a function of the water depth, since at low tide large areas of the tidal basin emerge and reduce the extent of open water available for wave formation. Water depth is a function of bathymetry and water level, the latter of which is primarily a function of tidal forcing and storm surge. It is thus clear that waves, tides, and basin morphology are tightly interconnected.

Fagherazzi and Wiberg (2009) used a simplified model to relate wave conditions to fetch and water depth in shallow tidal basins, in which water level was imposed throughout the whole basin, allowing water depth at each point of the basin to be determined as a function of bathymetry only. The fetch was then calculated for each fixed direction and a semi-empirical relationship (Young and Verhagen, 1996; CERC, 1984) was used to compute wave height for each wind direction and speed. This simplified model allows a characterization of the wave conditions over the entire basin without the need for a hydrodynamic model, but it is subject to some limitations, including assumptions of : i) uniform water level throughout the basin; ii) steady wave

conditions; iii) constant water depth along the fetch during wave propagation; and iv) no interaction between waves and currents.

A full hydrodynamic model is needed to unravel the complex interactions between tidal basin morphology, tides, waves and storms. The two-dimensional finite element model WWTM (Wind Wave Tidal Model) is used herein. The model solves the shallow water equations together with the formation and propagation of local wind waves based on the wave action conservation equation (see Defina, 2000; Carniello et al., 2005; D'Alpaos and Defina, 2007; Carniello et al., 2009a). The model is applied to a system of shallow lagoons and salt marshes in Virginia, USA, and it is validated with measurements of water levels and waves collected at five different locations within the lagoons. The model is then run with different hydrodynamic forcings (winds and tides) to calculate synthetic parameters that describe the erosion of the tidal flats and marsh boundaries. Finally, the model is used to infer the effects of Relative Sea Level Rise (RSLR) on these erosional parameters, as well as to predict the morphological evolution of the entire tidal basin.

1.2 Site Description

The study site is a system of shallow lagoons within the Virginia Coast Reserve (VCR), located on the Atlantic side of the Delmarva Peninsula, USA. The VCR hosts a Long Term Ecological Research (LTER) facility (www.vcrlter.virginia.edu/). The VCR includes a number of shallow lagoons, characterized by shallow tidal flats (about 1 m below MLLW) and deep channels (about 10 m below MSL), and is bordered by

emergent salt marshes (above MSL). The lagoons comprise intertidal and subtidal basins located between the barrier islands and the Delmarva Peninsula. Each basin is connected to the Atlantic Ocean through tidal inlets. The VCR is typical of shallow coastal barrier-lagoon-marsh systems that dominate the Atlantic and Gulf coasts of the USA. According to the hypsographic analysis of Oertel (2001), the lagoon is covered by salt marshes (30%), tidal flats (61%), and channels (9%).

Tides are semidiurnal, with a mean tidal range of 1.2 m. Mean higher-high water (MHHW) at Wachapreague channel (NOAA station 8631044, Fig. 1.1) is 0.68 m above mean sea level, whereas mean lower-low water (MLLW) is -0.70 m. During storm surges both high water and low water are modified, depending on wind intensity and direction, and on atmospheric pressure variations. The highest water level on record is 2.02 m above MSL (February 5 1998) whereas the lowest is -1.56 m above MSL (March 16 1980) (Wachapreague NOAA station, from Jun 28 1978 to present). The current rate of relative sea-level rise in the region is 3.8 – 4.0 mm yr^{-1} (Nerem et al., 1998; Oertel et al., 1989; Emory and Aubrey, 1991), and is among the highest rates recorded along the Atlantic Coast.

Storms are the primary agent of short-term disturbance in this coastal region. On average, over 20 extra-tropical storms rework the landscape each year (Hayden et al., 1995). Marsh vegetation on the salt marshes is dominated by *Spartina alterniflora*, with an average stem height of 30 cm and a height range between 50 and 100 cm. The shallow depths of the VCR make lagoon-bottom sediment ($D50 \approx 63\mu m$ with sorting coefficient $(D84/D50)^{1/2} \approx 2$) susceptible to wind-driven waves and currents, thus

promoting sediment resuspension (Lawson et al., 2007; Lawson, 2004); tides alone are generally insufficient to resuspend sediment from the lagoon bottom.

1.3 Model description

The hydrodynamic model WWTM solves the shallow water equations modified through the introduction of a refined sub-grid model of topography to deal with flooding and drying processes in irregular domains (Defina, 2000; D'Alpaos and Defina, 2007). The numerical model, which uses a finite-element technique and discretizes the domain with triangular elements, has been tested extensively in recent years in the Venice lagoon, Italy (Carniello et al., 2005; D'Alpaos and Defina, 2007; Defina et al, 2007; Carniello et al., 2009a).

The governing equations for the hydrodynamic model are:

$$\frac{\partial q_x}{\partial t}+\frac{\partial}{\partial x}\left(\frac{q_x^2}{Y}\right)+\frac{\partial}{\partial y}\left(\frac{q_y q_x}{Y}\right)-\left(\frac{\partial R_{xx}}{\partial x}+\frac{\partial R_{xy}}{\partial y}\right)+\frac{\tau_{bx}}{\rho}-\frac{\tau_{wx}}{\rho}+gY\frac{\partial h}{\partial x}=0$$

$$\frac{\partial q_y}{\partial t}+\frac{\partial}{\partial x}\left(\frac{q_x q_y}{Y}\right)+\frac{\partial}{\partial y}\left(\frac{q_y^2}{Y}\right)-\left(\frac{\partial R_{xy}}{\partial x}+\frac{\partial R_{yy}}{\partial y}\right)+\frac{\tau_{by}}{\rho}-\frac{\tau_{wy}}{\rho}+gY\frac{\partial h}{\partial y}=0 \quad \text{, (Eq. 1.1)}$$

$$\eta\frac{\partial h}{\partial t}+\frac{\partial q_x}{\partial x}+\frac{\partial q_y}{\partial y}=0$$

where t denotes time, q_x and q_y are the flow rates per unit width in the x and y horizontal directions, R_{ij} are the Reynolds stresses (i,j denoting either the x or y coordinates), $\tau_b=(\tau_{bx}, \tau_{by})$ is the bottom stress produced by tidal currents, $\tau_w=(\tau_{wx}, \tau_{wy})$

is the wind shear stress at the water surface, ρ is fluid density, h is the free surface elevation, g is the gravity. Y is the equivalent water depth, defined as the volume of water per unit area actually ponding the bottom, η is the local fraction of wetted domain, accounting for the actual area that can be wetted or dried during a tidal cycle. More details on the wetting and drying scheme are given in Defina (2000). In Eq. 1.1, the bottom shear stress τ_b is computed as

$$(\tau_{bx}, \tau_{by}) = \frac{\sqrt{q_x^2 + q_y^2}}{K_S^2 Y^{4/3}} (q_x, q_y), \text{ (Eq. 1.2)}$$

where K_S is the Strickler bed roughness coefficient.

For the wind-wave model, the wave action conservation equation is solved following a parameterized approach (Holthuijsen et al., 1989) and using a finite volume scheme. The wind-wave model is fully coupled with the hydrodynamic module (see Carniello et al., 2005; Carniello et al., 2009a). Assuming the direction of wave propagation adjusts instantaneously to the wind direction, the parameterized wave action conservation equation reads:

$$\frac{\partial N}{\partial t} + \frac{\partial}{\partial x} c_{gx} N + \frac{\partial}{\partial y} c_{gy} N = S \text{ , (Eq. 1.3)}$$

where N is the zero-order moment of the wave action spectrum, defined as the ratio between wave energy E and the relative wave frequency σ, averaged over frequency, and c_{gx} and c_{gy} are the group celerity components. S is the source term which takes into

account all the physical processes contributing to wave energy, and it is described by the following equation:

$$S = S_w - S_{bf} - S_{wc} - S_{brk}\text{ , (Eq. 1.4)}$$

where S_w is the wave growth by wind action on the water surface, and the other terms describe the dissipation of wave energy by bottom friction (S_{bf}), white-capping (S_{wc}) and depth-induced breaking (S_{brk}). The source term can be expressed as a function of wind speed, water depth, and wave energy as:

$$S = \alpha + \beta N - 2C_f \frac{k}{\sinh(2kY)} N - c\sigma\left(\frac{\gamma}{\gamma_{PM}}\right)^m N - \frac{2a}{T_p} Q_b \left(\frac{H_{max}}{H}\right)^2 N \text{ . (Eq. 1.5)}$$

The values of the parameters α and β depend on the wind speed U , C_f is a friction coefficient, γ is the integral wave steepness parameter, i.e. $\gamma = E\sigma^4 / g^2$, γ_{PM} is the theoretical value of γ for a Pearson-Moskowitz spectrum, Q_b is the probability that waves with height H will break, Tp is the wave period, c, m and α are empirical parameters. The numerical values of the parameters used to solve Eq. 1.5 are reported in Carniello et al. (2005) and Fagherazzi et al. (2006).

Following the approach suggested in Carniello et al. (2009a), the space and time variation of the peak wave period T_p (which was assumed to be constant in Carniello et al., 2005) is related to the local and instantaneous water depth and wind speed. The peak wave period is then computed, at each time step and at each grid point with the

following empirical equation relating the wave period to the local water depth and wind speed (Young and Verhagen, 1996; Breugem and Holthuijsen, 2007)

$$\tilde{T} = 5\tilde{Y}^{0.375}, \text{ (Eq. 1.6)}$$

where $\tilde{T} = gT_p / U_{wind}$ and $\tilde{Y} = gY / U_{wind}^2$ are the dimensionless wave period and water depth and U_{wind} is wind speed (measured at an elevation of 10 m above still water level).

The model mesh consists of 68000 triangular elements and 35000 nodes, and covers an area of approximately 60 km x 20 km (Fig 1.1). The area inside the bay is approximately 500 km^2. Element size ranges on average from 100 to 200m, with the smallest elements close to 10m. As a boundary condition, we impose the water elevation at the seaward boundary of the model domain; zero flux conditions are imposed at the landward boundary. Wind characteristics (speed and direction) are imposed uniformly throughout the whole basin. Three different values for the Strickler roughness coefficient are used in Eq. 1.2: 15 $m^{1/3}/s$ for the salt marsh, 20 $m^{1/3}/s$ for the tidal flats, 25 $m^{1/3}/s$ for the channels and the shelf outside the barrier islands. The drag coefficient C_d is related to the Strickler coefficient K_S by $C_d = gY^{-1/3}K_S^{-2}$, resulting in the following values of C_d for the given K_s (fixing the water depth Y equal to 1m): 0.043, 0.024, and 0.016. Similar values have been used for the Venice lagoon (Defina, 2000; Umgiesser et al. 2004; D'Alpaos and Defina, 2007) a similar tidal environment located in the north-east of Italy. Neither river discharge nor atmospheric precipitation are taken into account in our simulations.

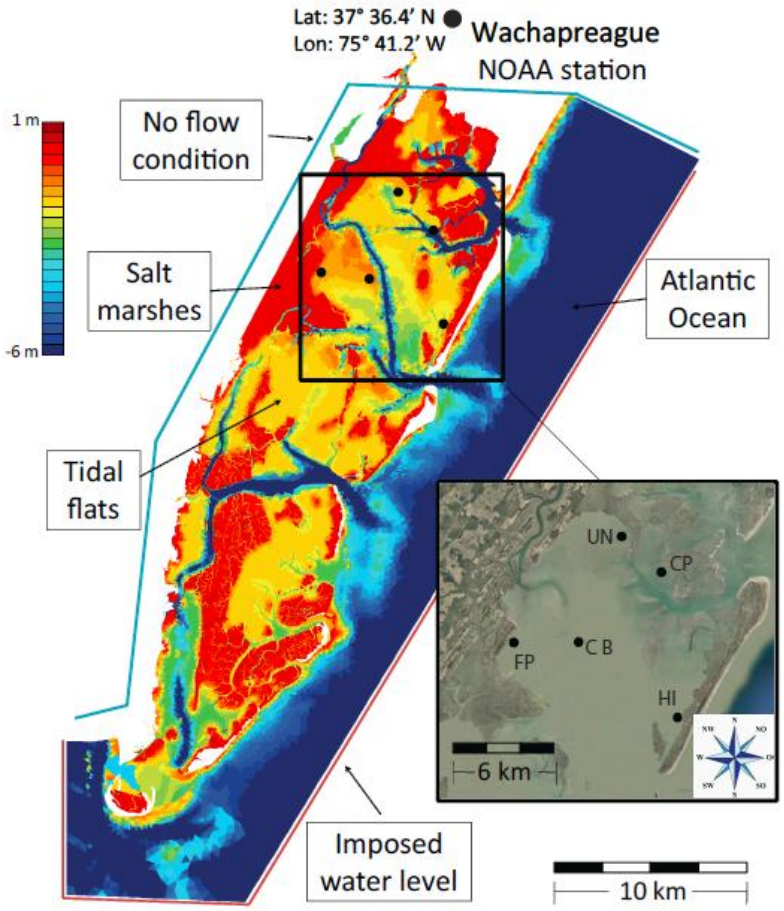

Figure 1.1: Bathymetry of the VCR-LTER lagoons. Color indicates ground elevation. Inset shows our measurement sites within Hog Island Bay: FP Fowling Point, UN Upshur Neck, CP Chimney Pole, HI Hog Island, CB Center Bay. Position and coordinates of the Wachapreague NOAA station.

1.4 Model testing

To test the model, we compare its results to field measurements. Two periods are considered for the model testing: Period #1 from 1/31/09 to 2/5/09 (a total of 144 consecutive hours), and Period #2 from 3/1/09 to 3/2/09 (a total of 72 consecutive hours). Wave events characterized by different wind speeds and directions were present

during these periods, permitting us to evaluate the model response, particularly the wave module performance, under different conditions.

Water level was measured with high resolution piezoresistive transducers (RBR© TGR 2050P and Nortek© Aquadopp profilers). The instruments were deployed at five sites (Fig. 1.1): four of them close to the marsh boundary (Upshur Neck, UN, Chimney Pole, CP, Fowling Point, FP, Hog Island, HI), and one close to the main channel that dissects the basin (Center Bay, CB). We used RBR sensors at UN, FP and CB and Nortek Aquadopps at HI and CP. During Period #1, all the instruments were recording; during Period #2, only the RBR instruments were recording. Water level is computed as the average over a sampling interval (RBR instruments recorded every 30 min, averaging over 300 s; Nortek current profilers record every 10 min, averaging over 60 s). Wave data were recorded every 30 minutes, sampling 512 bursts with a frequency of 2 Hz. From each wave burst a significant wave height (H_s) and peak period (T_p) are calculated from the power spectral density estimate via Welch's periodogram method (Press et al., 1992).

The model is set up to simulate the same hydrodynamic conditions that were present during the measurement periods. The water level in time is imposed at the seaward boundary (Fig. 1.1). Since no records of tidal oscillations exist in that area, the water level is set equal to the value measured inside the basin shifted by a lag time (location HI, just near the tidal inlet, for Period #1, and location CB for Period #2). The lag time is determined by measuring the delay of the water level propagation from the seaward boundary to the instrument location. The wind input data are taken from the NOAA

station at Wachapreague station (ID 8631044), where wind speed and direction are collected every 6 minutes. The wind field is applied uniformly throughout the domain with the same time resolution as the available data. Analysis of the effect of wind speed and direction measured in different locations within the lagoon of Venice in the application of WWTM suggests that assuming a uniform wind field is acceptable, especially in stormy conditions (i.e. $U_{wind} \geq 10$ m/s). However, in some cases, non-uniformity of wind speed and direction can have some impact especially on the wind wave distribution (Carniello et al., 2009a,b).

Two statistics are used to provide an objective evaluation of model performance: the Model Efficiency (ME)

$$ME = 1 - \frac{\sum (D - M)^2}{\sum (D - \overline{D})^2} \text{ , (Eq. 1.7)}$$

which measures the ratio of the model error to variability in observational data, and the Root Mean Squared Error (RMSE)

$$RMSE = \sqrt{\sum \frac{(D - M)^2}{n}} \text{ (Eq. 1.8)}$$

where D is the observational data, $\overline{D}$ is the mean of the observational data and M is the corresponding model estimate (Allen et al., 2007).

Period #1 is characterized by approximately 11 full tidal cycles with a mean tidal amplitude of 1.3 m (Fig. 1.2A). The maximum water level excursion is 1.9 m and is due to the combined effect of the astronomical tide and storm surge. During Period #1 there

are three main wind events (Fig. 1.2B): in the first event the wind blows from north (300°-360°) and has a maximum speed of 6 m/s; in the second event the wind blows from southeast (220°) with a maximum speed of 7 m/s; in the third event the wind blows again from north with maximum speed of 7 m/s.

Water levels computed with the model generally are in agreement with measured values (Fig. 1.2A). Water-level oscillations are similar at each measurement site within the basin, and are similar to the water level imposed at the seaward boundary. The tidal signal does not change significantly in shape as it propagates within the basin (the difference between measurement sites is less than 1 cm, on the order of measure error), and only a phase shift is present. From the model simulation the phase shift between the seaward boundary and the measurement sites are: HI 1 hour, CP 0.8 hours, CB 1.1 hours, UN 1.2 hours, and FP 1.4 hours. For all the station the RMSE is between 7 and 11 cm, while the ME is close to 1.0. The large value of ME is governed by the forcing at the seaward boundary, which strongly controls the water level. Since the difference between the measured and predicted water level has no correlation with the water level, we conclude that the model reproduces correctly the tide oscillation phase lag among the different stations. Also the range of tidal amplitude is well reproduced: both measured and predicted values do not change significantly (few %) inside the basin. The remaining error in the water level is probably due to some additional overharmonics present in the basin not reproduced by the model.

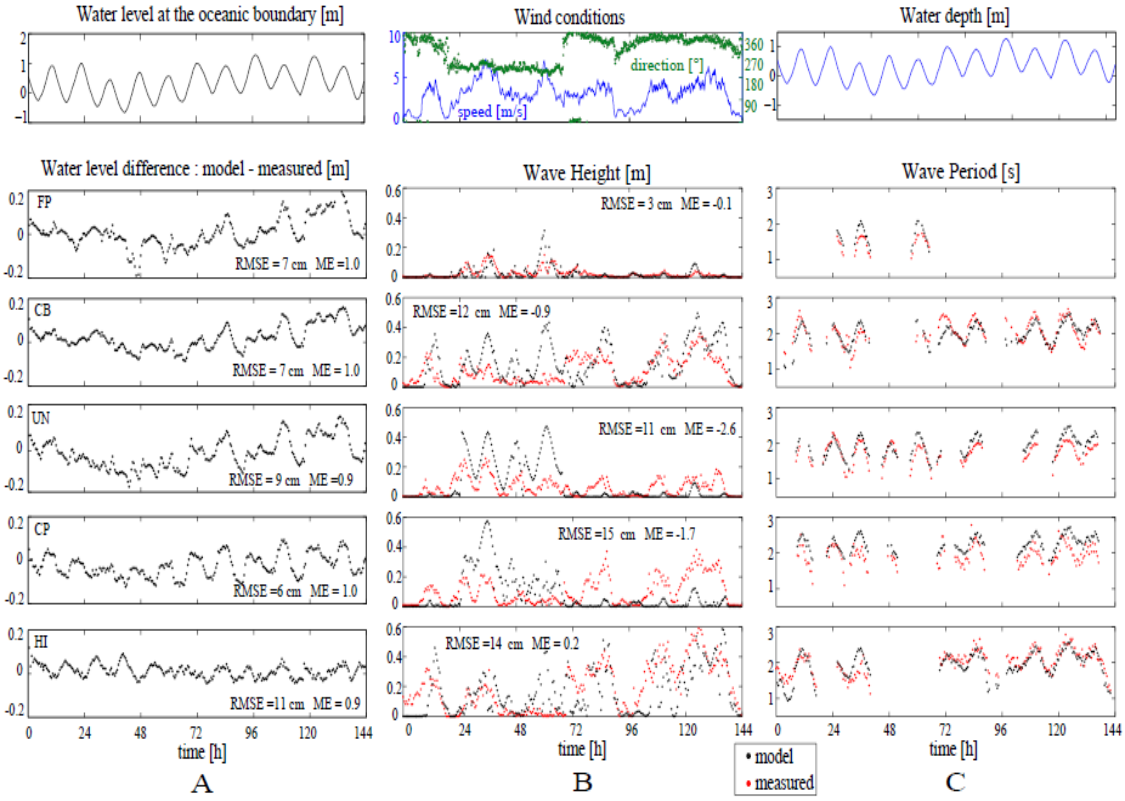

Figure 1.2: Simulation of Period #1 (from 1/31/09 to 2/5/09). Water level (referred to MSL) imposed at the seaward boundary, water depth (A), wave height (B) and period (C) measured and computed at the five study sites. Wave period is reported only for measured wave height greater than 0.1m. On top of figure 1.2B: wind speed from the NOAA Wachapreague station ID 8631044.

The agreement between computed and measured wave height varies from site to site (Fig. 1.2B). At the CB site, the wave regime is mainly determined by wind speed, since the fetch is approximately constant in every direction and the water depth is not a strong limiting factor (the minimum water depth is 1 m). Wave height variations are reasonably well represented by the model, with a few wave peaks underestimated in the first half of Period #1. At FP, the wave regime is strongly affected by water depth, since the tidal flats emerge at low water levels. Simulated wave heights at this location are

similar to measured values. At the other three sites, HI UN and CP, all located close to the marsh boundary, the wave regime is controlled strongly by wind speed and direction, and less by water depth. When the wind blows from the salt marsh, the fetch is almost zero and very small waves form even if the wind speed is high. When the wind blows from the open bay toward the salt marsh, the wave height is determined mainly by wind speed. At HI, where relatively higher waves are present, ME is positive, meaning that the model forecast is a better predictor of wave height than the average value of observed wave height. ME is negative for CB and for three of the four sites near the marsh edge (FP, UN and CP), suggesting that in this case the average value of observed wave height is a better predictor of wave height than the model forecast. We believe that these poor values for ME can be ascribed partly to an inadequate description of the wind field over the lagoon (wind data are measured at the NOAA station which is not located within the lagoon, see Fig. 1). In fact most of the wave peaks are reproduced by the model, except for the middle part of Period #1 at UN and CP, where the measured wave height is almost zero and computed values are between 10 and 40 cm. Since the wind intensity is not zero during that period, the discrepancy between simulations and measurements is probably due wind non-uniformity over the entire basin. Note that during Period #1 wind speed is moderately low and, as stated above, in these conditions wind uniformity is questionable. Waves computed by the model are compared to measured values only where the wave height is greater than 0.1 m.

Measured wave period falls in the range of 1.5-2.5 s, with variations in phase with water depth. The model follows these variations with good agreement.

Period #2 is characterized by approximately 4 tidal oscillations (Fig. 1.3). Wind direction was relatively constant (around 0°N) and wind speed varied between 5 and 10 m/s, except for several hours when the wind blew at 15 m/s. The model reproduces correctly the tidal oscillations (ME=1, not reported in the figure). Wave height is reproduced better than during Period #1: ME is between 0.2 and 0.5 in the sites where waves are present, CB and FP (Fig. 1.3A). This result indicates that the model performs better when wind speed is ≥10 m/s, which is significant for the following simulations. Also in this case the period is well predicted by the model.

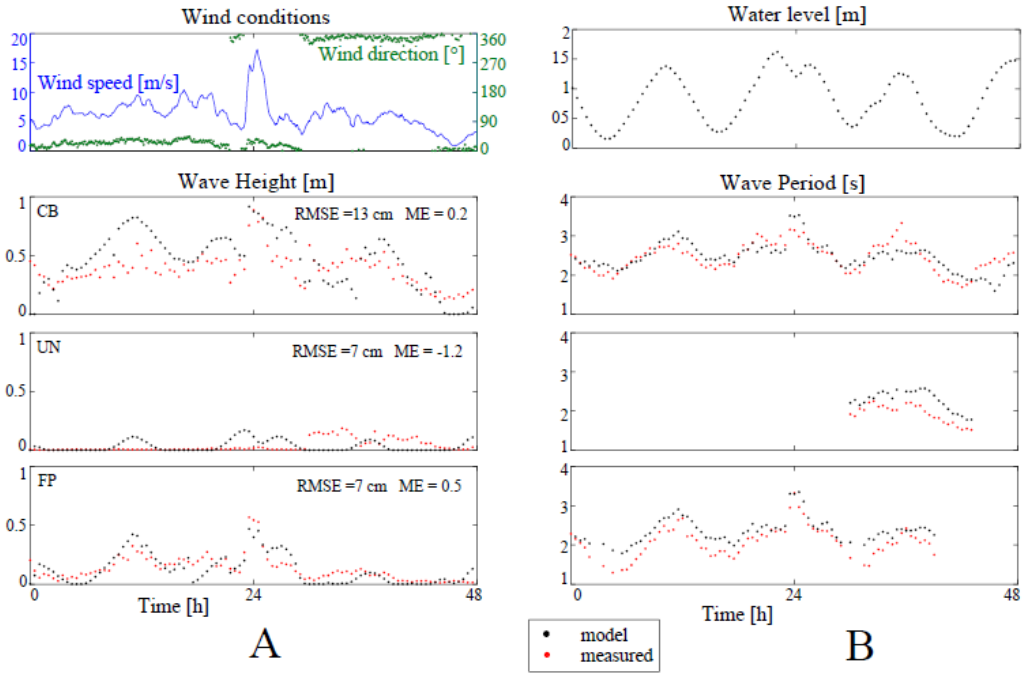

Figure 1.3: Simulation of Period #2 (from 3/1/09 to 3/2/09). Wind speed from the NOAA Wachapreague station (ID 8631044). Wave height and wave period measured

and computed at the five reference sites. Wave period is reported only for measured wave height greater than 0.1m.

1.5 Model forecasting

We use the model to study the tidal basin response to a variety of hydrodynamic forcing conditions, namely variations in sea level, tides, and wind fields. Since the use of all possible combinations of tidal oscillations and wind conditions is not feasible, only few combinations are chosen. The next section focuses on the choice of the most significant hydrodynamic inputs for the model. In the model simulations described above, water level was imposed outside the basin at the seaward domain boundary (Fig. 1.2) using the data measured inside the lagoon and shifted appropriately in time. To determine the water level to impose on the seaward boundary for the model forecasts, astronomical tidal components measured at the Wachapreague station are used to create a synthetic tidal signal. Since the goal is to simulate the tide outside the lagoon, tidal harmonics deriving from shallow water effects are neglected. All other 27 components are considered (the 6 greatest components are reported in Table 1). The synthetic tide generated with this method has a very long periodicity, at least equal to the lunar cycle. For computational reasons, is not feasible to run each simulation for such a long period. Therefore, a window of 72 hours is used, and is chosen to avoid both extremely high and extremely low oscillations in order to be representative of the whole signal. In addition, the first 24 hours of simulations are discarded form the analysis in order to eliminate the transient effect of the initial conditions. Therefore each simulation gives 48 hours, i.e., four full tidal cycles, of usable results.

Component	M2	S2	N2	K1	M4	O1
Speed [degree/hour]	28.984	30.000	28.440	15.041	57.968	13.943
Amplitude [m]	0.590	0.102	0.126	0.084	0.025	0.087
Phase [degree]	26.8	63.2	16.9	204.0	221.8	216.7

Table 1.1: Values of the 6 largest astronomical tide components at Wachapreague station (NOAA).

Winds are variable, seldom maintaining a constant speed and direction for longer than several hours. However, the results of a set of numerical experiments performed to assess the impact of wind transients on the wave field show that the impact is moderate because the adaptation time is relatively short (i.e., shorter than 10-15 minutes). Therefore, for simplicity, all simulations are run with constant wind speed and direction, using four classes of wind (5, 10, 15 and 20 m/s), and twelve directions. Using a constant wind during the simulations allows us to isolate the basin response to each specific wind condition. The results obtained with these simulations can be easily combined with wind statistics (frequency and duration distribution) to infer the basin response to more realistic meteorological conditions.

Although the tide is the main factor controlling water levels, storm surges contribute significantly to water elevation during storms. Storm surge is the temporary and local change in water-surface elevation along a shore due to a storm (Boon 2004). Tilburg and Garvine (2004) showed that up to 65% of storm surge in Atlantic City, NJ, could be

explained considering just three processes: inverse barometric effect, wind and wave set up, and Ekman transport. The first is due to a change in the atmospheric pressure, the second is induced by the wind blowing across shore, while the third is produced by the wind blowing along shore for an unconfined shoreline.

We perform a statistical analysis to correlate storm surge to three variables: atmospheric pressure, wind speed, and wind direction. For the analysis we use the storm surge data of the Wachapreague station and the meteorological data of the NOAA Station CHLV2 - Chesapeake Light, VA, taken in the period from 1996 to 1999. First we obtain the pressure corrected storm surge (PCSS) applying an inverse barometric correction (IBC). The IBC assumes that each mBar of pressure higher (lower) than the average atmospheric pressure, 1018mBar, decreases (increases) the sea level of 1 cm. Then we classify the average PCSS binned by 12 wind directions and 4 wind speed categories (Fig. 1.4A). We perform the same classification (wind speed and direction) for the pressure (Fig. 1.4B). The PCSS is clearly correlated to the wind direction: the highest storm surge occurs when the wind blows from 50°N, while extremely low water levels occur with wind from 230°N. Because pressure gradients drive winds, it is not surprising to find the barometric effect correlated with wind conditions. However the barometric effect is correlated mainly on wind speed, and only slightly on wind direction.

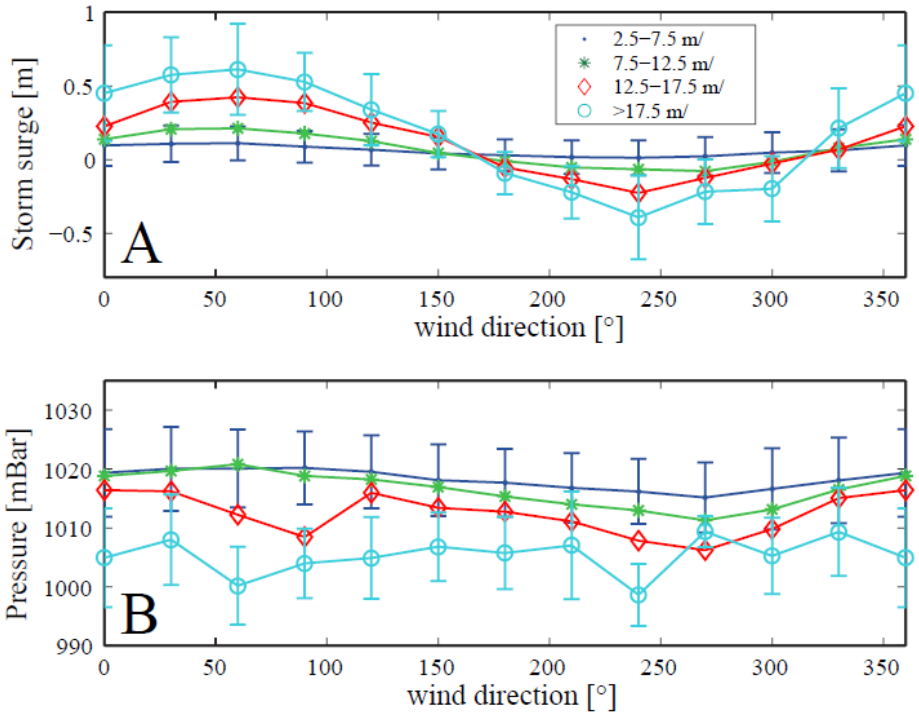

Figure 0.4: A) Average pressure corrected storm surge (PCSS); B) Average atmospheric pressure. Data are binned by 12 wind direction and 4 wind speed categories. The total storm surge can be calculated by adding the inverse barometric correction (IBC) to the PCSS. For visual clarity error bar are reported only for wind speed of 5 and 20 m/s. Data are from NOAA Station CHLV2, during 1996 to 1999.

For any given wind speed and direction, Figure 1.4 gives the expected PCSS and atmospheric pressure, which can be combined with the IBC to give the expected total storm surge. This procedure is used for each simulation, in order to associate to each wind event its most probable storm surge. Operatively, the storm surge is added as a constant term to the tidal signal at the seaward boundary.

1.6 Wave energy and bottom shear stresses

Wind waves and tidal currents produce bottom shear stresses that resuspend sediments in tidal basins. Bottom shear stress is a non-linear combination of shear stress from currents (τ_{curr}) and wave (τ_{wave}), which, according to Soulsby (1995, 1997)

$$\tau_m = \tau_{wave} + \tau_{curr}\left[1+1.2\left(\frac{\tau_{wave}}{\tau_{wave}+\tau_{curr}}\right)^{3.2}\right], \text{(Eq. 1.9)}$$

where τ_m is the mean total bottom shear stress. Limiting the analysis to monochromatic waves, under the assumption of linear wave theory the maximum velocity of wave-induced water motion at the bottom is given by:

$$u_b = \frac{\pi H_s}{T_p \sinh(kY)} \quad \text{(Eq. 1.10)}$$

and the wave bottom shear stress is given by:

$$\tau_{wave} = \frac{1}{2} f_w \rho u_b^2 \text{ , (Eq. 1.11)}$$

with

$$f_w = 0.04\left[\frac{u_b T_p}{2\pi k_b}\right]^{-0.25} \text{ , (Eq. 1.12)}$$

where k is wave number and f_w is a friction factor that depends on the roughness length scale of the sediment bed k_b (Fredsoe and Deigaard, 1993). Herein, we let $k_b = 2D_{90}$ (e.g., Kamphius, 1975), so that Eq. 1.8 estimates the skin friction stress, and set D_{90} =

0.25 mm based on grain size data from Hog Island Bay (Lawson, 2004). The wave number k can be determined from the dispersion equation derived from linear wave theory:

$$\sigma = \sqrt{gk \tanh(kY)} \quad . \text{(Eq. 1.13)}$$

Bottom shear stress induced by tidal currents is calculated using an equation for uniform flow:

$$\tau_{curr} = C_f \rho U^2 \quad , \text{(Eq. 1.14)}$$

where C_f is a friction coefficient assumed equal to 0.01 (Fagherazzi et al. 2007). It is worth noting that C_f is not the same at that used in WWTM (C_d=0.024 for tidal flats) where the drag coefficient conceptualize all the processes responsible for energy dissipation (see D'Alpaos and Defina 2007). Sediment resuspension is instead related only to the friction induced by currents at the bottom.

The bottom shear stress is calculated only for the tidal flats inside the lagoon, discarding the elements of the mesh representing the creeks, the salt marshes, and the shelf offshore the barrier islands. For each simulation (4 wind speeds x 12 wind directions) bottom shear stresses are calculated at every point of the tidal flat (~20,000 elements) and recorded every 30 minutes for 48 hours. Examples of the wave induced and current induced bottom shear stress distributions, computed for four tide levels (low and high slack water, mid-flood and mid-ebb) are given in Figure 1.5. The wave induced bottom shear stress is quite uniform across the basin (Fig. 1.5C), and is slightly higher during high water because wave height increases with water depth for a given wind speed (see

also Fig. 1.5B). The current induced bottom shear stress is higher at mid-tide, when the water level displacement is fastest, and it is concentrated in the main channels (Fig. 1.5B,D). There are no major ebb/flood differences in current induced bottom shear stress either on the tidal flat or in the channels; minor differences are related to the diurnal modulation with greater shear stresses associated to higher tidal excursions (Fig. 1.5B). Shear stresses are higher during ebb than during flood at the southern inlet, while the opposite is true at the northern inlet. This asymmetry is due to a residual circulation with water entering the bay through the northern inlets and leaving through the southern one.

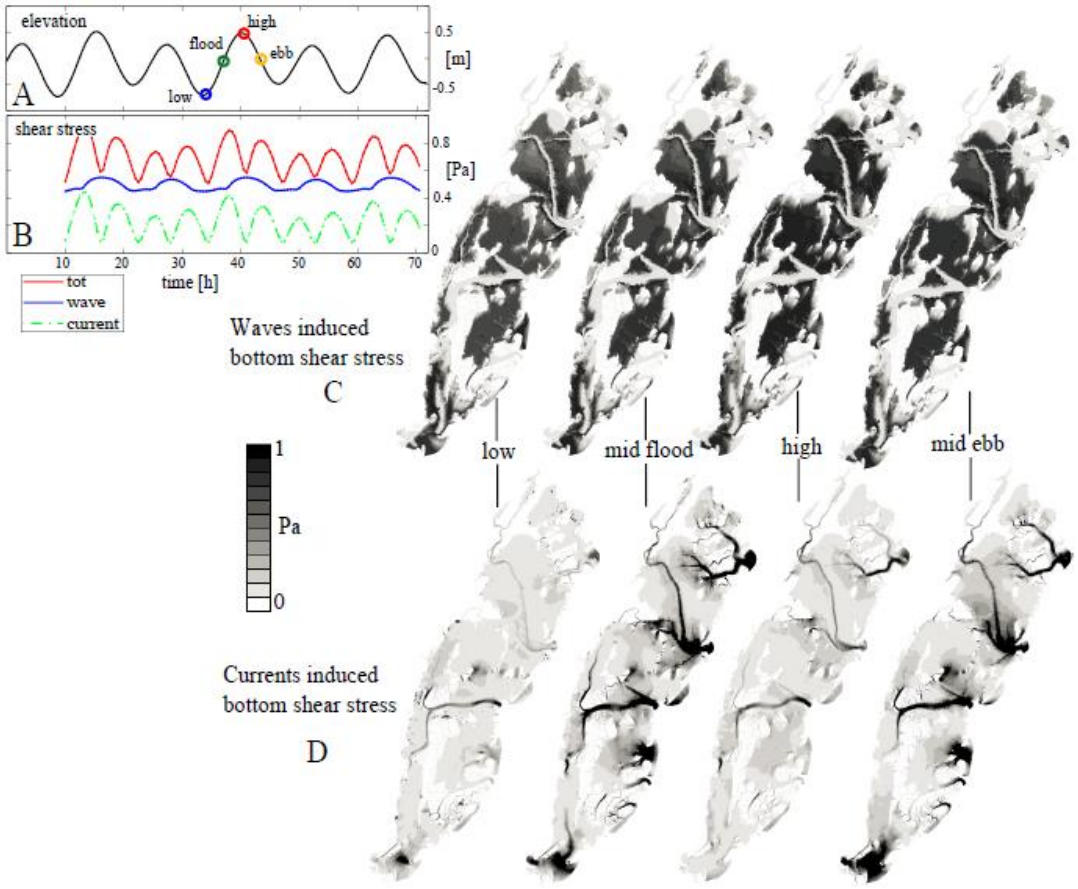

Figure 1.5: A)Water level imposed at the seaward boundary. B,C,D) Wave-induced and current induced bottom shear stress computed for a wind speed of 15 m/s blowing from 30° N, averaged over the tidal flat area (B), and reported at high and low slack water, and mid-ebb and mid-flood tide (C,D).

In order to aggregate the data from our simulations, we simultaneously compute the bottom shear stress distribution over time (i.e. over different water levels), for a fixed wind speed of 15 m/s. The same calculation is performed individually for the wave shear stress and the tidal current shear stress (Fig. 1.6). The spatial distribution of wave-induced shear stress is non-monotonic. The fractional area is almost constant for bottom stresses from 0 to ~0.6 Pa, then increases reaching a peak around 0.8 Pa, and then decreases to zero. No values greater than 1 Pa are present. This distribution reflects the

tendency of waves to reach a balance between energy input from the wind and dissipation, so that bottom shear stresses are relatively constant within the tidal flats. The distribution of tidal current shear stress has a negative exponential shape with more than 95% of the basin area under 0.35 Pa. However, the distribution includes locations where the shear stress is higher than the wave induced shear stress, as shown in Figure 1.5D. This reflects the fact that tidal currents tend to concentrate the flow in selected areas thus increasing shear stresses.

In conclusion, wave induced shear stress is relatively uniform in space and in time (see also Fig. 1.5B), while current induced shear stress is more variable. The distribution of the total shear stress depends on both, as indicated in Eq. 1.8; it has the same qualitative behavior as the wave shear stress, but it is broader because of the contribution of the current shear stresses. Wave- and current-induced bottom shear stresses are of the same order of magnitude, approximately 0-1 Pa, and therefore they both affect erosive processes on the tidal flats and need to be included in the analysis.

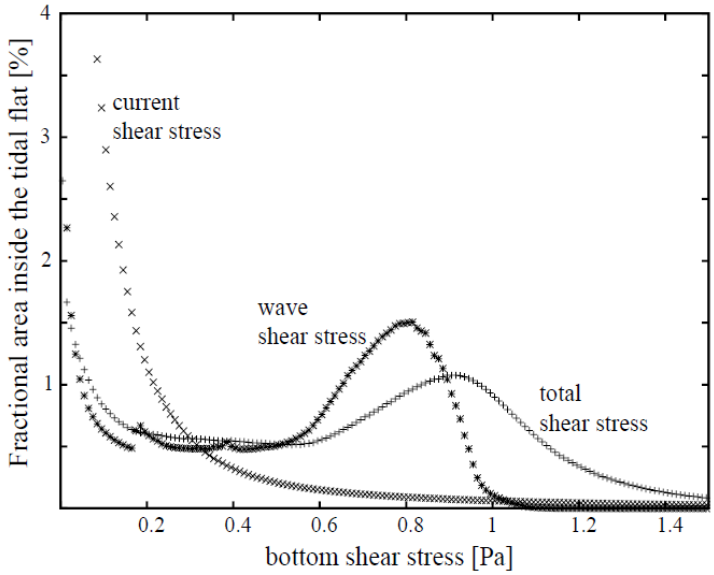

Figure 1.6: Spatial distribution inside the basin of current-induced, wave-induced and total mean bottom shear stress (Eqs. 7,9,12), calculated from the results of 12 simulations (wind direction every 30°) with wind speed equal to 15 m/s.

To better describe the erosion characteristics of the basin, a synthetic parameter is used to aggregate the information of the bottom shear stress. An erosion factor EF, similar to the one proposed by Fagherazzi and Wiberg (2009), is defined as follows:

$$EF = \frac{\sum_{t=1}^{T}\sum_{i=1}^{N_e} A_i\left(\tau_m(i,t) - \tau_{cr}\right)}{A_{tf}T} \quad \text{, (Eq. 1.15)}$$

where $\tau_m(i,t)$ is the mean bottom shear stress at time t at a location i which has an area equal to Ai ,τ_{cr} is a suitable value of critical shear stress for bottom erosion (values of $\tau_m(i,t)-\tau_{cr} < 0$ are set equal to zero). N_e is the number of mesh elements in the tidal flat, A_{tf} is the area of the tidal flat, and T is the length of the time averaging (48 hours). This parameter represents the excess shear stress integrated over the entire basin and averaged over time. The time average is needed to take into account the difference in

the bottom shear stress induced by tidal oscillations in water depth. For simplicity, we set τ_{cr} to 0.35 Pa based on measurements and modeling of sediment erosion and resuspension in the study area (Lawson 2008).

The Erosion Factor is first calculated considering the contribution of current bottom shear stresses (EFc) and wave bottom shear stresses (EFw) separately. EFc has a weak dependence on wind characteristics for wind speeds ≤ 15 m/s (Fig. 1.7A). Only for higher wind speeds (20 m/s) are the differences in EFc significant. In contrast, EFw depends strongly on wind speed (Fig. 1.7B): for a wind speed of 5m/s, EFw is zero, for wind speeds of 10-15 m/s, values of EFw are similar to EFc, and for a wind speed of 20 m/s EFw is 3 times EFc. EFw depends also on wind direction and is greater when the wind blows along the main axis of the basin (N-E to S-W) than when it blows along the minor axis (N-W to S-E). For low wind speed (10-15 m/s) EFw shows a central symmetry and is the same for each pair of opposite wind directions. For wind speeds of 20 m/s the symmetry is lost, especially along the major axis, EFw is greater for wind blowing from NE than from SW. The range of values assumed by EFc and EFw and by the current induced and wave induced bottom shear stresses (between 0 and 1 Pa) is comparable to values found in similar studies that employ models (Le Hir at al., 2000; Cappucci et al., 2004; Fagherazzi et al., 2007) and field measurements (Christie and Dyer, 1998; Whitehouse and Mitchener, 1998).

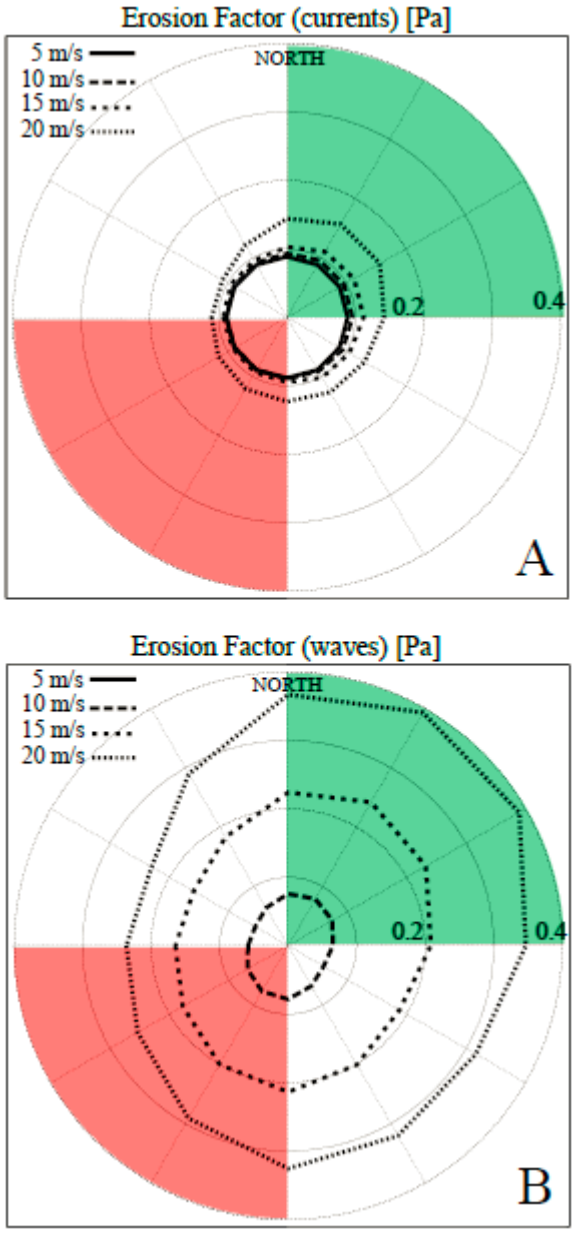

Figure 1.7: Erosion Factor (EF) calculated from current-induced (A) and from wave-induced (B) bottom shear stresses.

The total Erosion Factor (EF) reflects the contribution of both EFc and EFw. It strongly depends on wind speed and, in a minor way, on wind direction (Fig. 1.8A). For each

wind speed, the difference between the maximum and minimum value of EF is around 20%. EF values are greater when the wind blows along the main axis of the basin (N-E to S-W) than when it blows along the minor axis (N-W to S-E). The ratio between the maximum and minimum EF increases with increasing wind speed.

Schwimmer (2001) correlates marsh regression rate to averaged wave power, defined as:

$$P = c_g \frac{\gamma H^2}{8} \text{ , (Eq. 1.16)}$$

where γ is the water specific weight and c_g is the wave group celerity given by $c_g = \frac{\sigma}{k}\frac{1}{2}\left(1+\frac{2kY}{\sinh(2kY)}\right)$, which assumes value in the range 0-2 m/s.

In order to describe the erosion potential by impacting waves at the marsh boundary, we choose the wave power as the main variable. We introduce a Wave Factor at the marsh Boundary, WFB, similar to the erosion factor EF, to synthesize the information given by different hydrodynamic conditions:

$$WFB = \frac{\Sigma_{t=1}^{T}\Sigma_{i=1}^{M} L_i \left(P(i,t) - P_{cr}\right)}{L_{mb} T} \text{ (Eq. 1.17)}$$

where P(i,t) is the wave power at time t at a marsh boundary element i which has a length equal to Li, M is the number of marsh boundary elements, L_{mb} is the total length of the marsh boundary, and T is the length of the time averaging (48 hours). Similar to bed erosion by shear stresses, we assume that erosion by wave impact is a threshold process, which takes place when the incoming wave power P is greater than a critical

value P_{cr}. As for EF, the time average is needed to take into account the difference induced by the variable water level through a tidal cycle. This parameter represents the total amount of wave energy per unit of time that reaches the marsh boundary and is dissipated there. Therefore, assuming the erosion rate of the marsh boundary is proportional to this parameter, WFB is a proxy for total marsh boundary retreat within the basin.

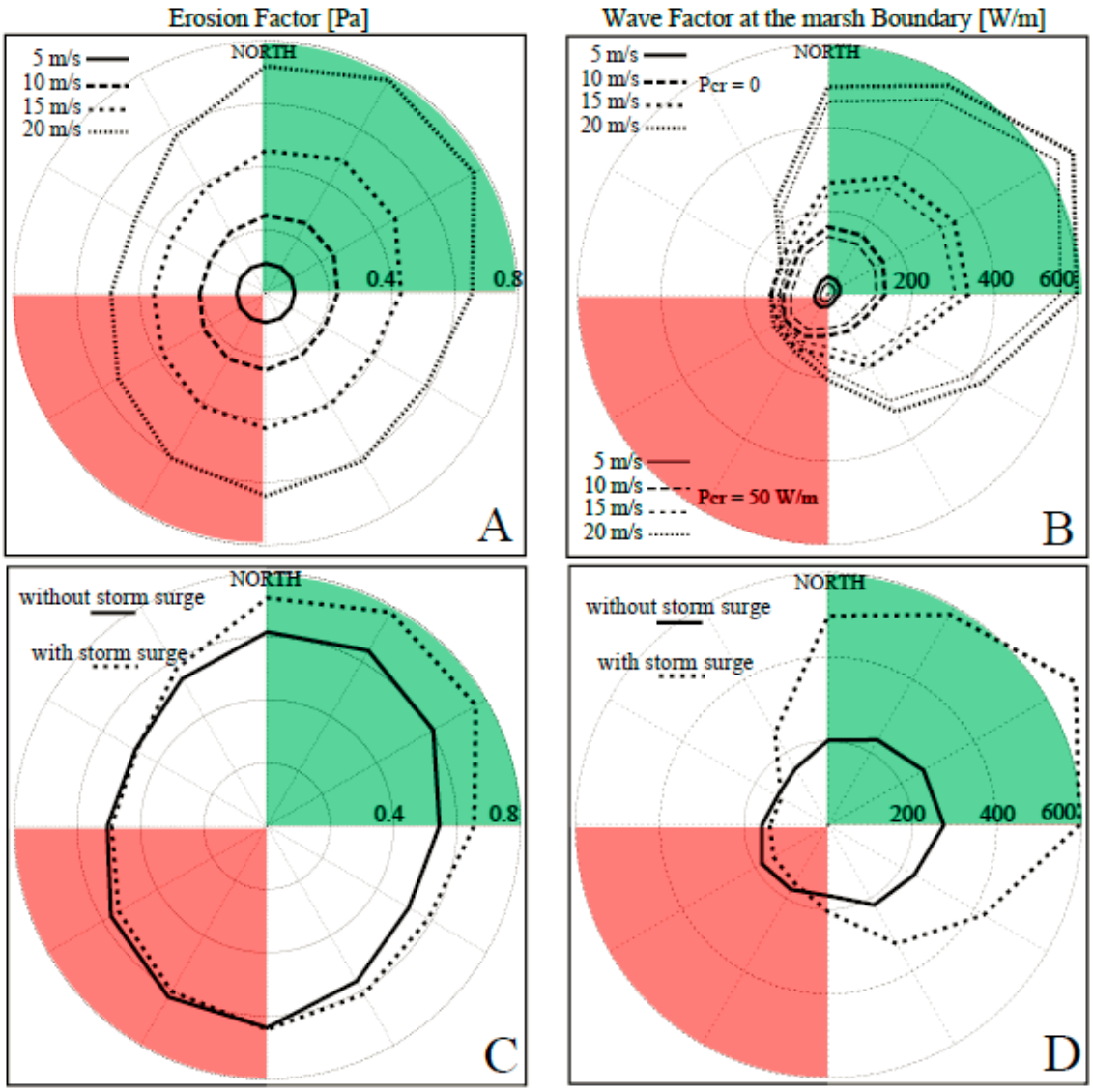

Figure 1.8: A) Erosion Factor (EF) and B) Wave Factor at the marsh Boundary (WFB) calculated for different wind speeds and reported as a function of wind direction. The critical value for bottom shear stress is set equal to 0.35 Pa. WFB is calculated without any threshold values (ticked lines) and with a threshold equal to 50 W/m (thinner lines).Green area represents direction associated predominantly with positive storm surges, red area represents directions associated predominantly with negative storm surges (see Fig. 1.4). In C) and D) EF and WFB calculated for a wind of 20 m/s are compared to simulations that neglect changes in sea level produced by storm surges.

We calculate the WFB for several wind speed and directions (Fig. 1.8B), and for two different values of the threshold P_{cr}: 0 and 50 W/m (corresponding approximately to a wave height of 0.2 m). The computed wave power range, from 0 to 600 W/m, is smaller than the range found in a similar work by Schwimmer (2001): 0 to 10000 W/m. This difference is probably due to the fact that WFB averages wave power during the full tidal cycle, taking into account very low water depths, when wave height is strongly reduced. For each fixed wind speed, WFB varies with wind direction. WFB, like EF, is greater when the wind blows along the main axis of the basin (N-E to S-W) than when it blows along the minor axis (N-W to S-E). However, WFB is consistently higher for wind blowing from N-E than for wind blowing from S-W. The difference is more evident when higher wind speeds are considered. Increasing the threshold value P_{cr} decreases values of WFB; however it does not significantly change the WFB dependence on wind regime (speed and direction).

An additional simulation is performed only for a wind speed of 20 m/s, neglecting the superimposition of the storm surge associated with the wind conditions, i.e. using the same water level for each wind direction. Without storm surges the EF is symmetric with respect to the wind direction, resulting in an ellipse with the major axis aligned to the basin main axis (Fig. 1.8C). The presence of a positive storm surge increases the EF up to 30% while a negative storm surge slightly affects it. Even the WFB is more symmetric without storm surges (Fig. 1.8D). The presence of a positive storm surge increases WFB up to 150%, while the presence of a negative storm surge decreases WFB at most by 10%.

The Erosion Factor EF and the Wave Factor at the marsh Boundary WFB permit us to synthesize the effects of waves on sediment mobilization and to understand the relative importance of different wind conditions. This notwithstanding, it is also important to determine the spatial distribution of waves across the tidal flats and at the marsh boundaries in order to define which areas are most prone to erosion. For simplicity we present the spatial distribution of the erosion stresses only for two wind speeds (10 and 20 m/s) and two wind directions (30° and 210° N). To provide an objective evaluation, for each wind condition WFB is calculated as a function of marsh boundary exposure.

The spatial distribution of the wave power at the marsh boundary depends strongly on wind direction (Fig. 1.9). The marsh boundaries facing the wind receive more wave power (quantified in W/m), while the marsh boundaries facing the opposite direction receive almost no wave power. Also the spatial distribution of the wave induced bottom shear stress depends on wind direction (Fig. 1.10A). This dependence is greater close to the marsh boundary where fetch, and consequently wave height, is strongly controlled by wind direction because of the presence of the marshes which prevent wave formation on their leeward sides. The dependence of wave shear stress on wind direction decreases moving away from the marsh boundary, and vanishes after 3-4 km. Wave shear stress is negligible inside the channels because of their large depth compared to the tidal flats. In contrast, the current-induced bottom shear stress is high inside the channels and is negligible on the tidal flat (Fig. 1.10B). The total shear stress, reflecting both contributions, is higher both far from the marsh boundaries and inside the channels (Fig. 1.10C).

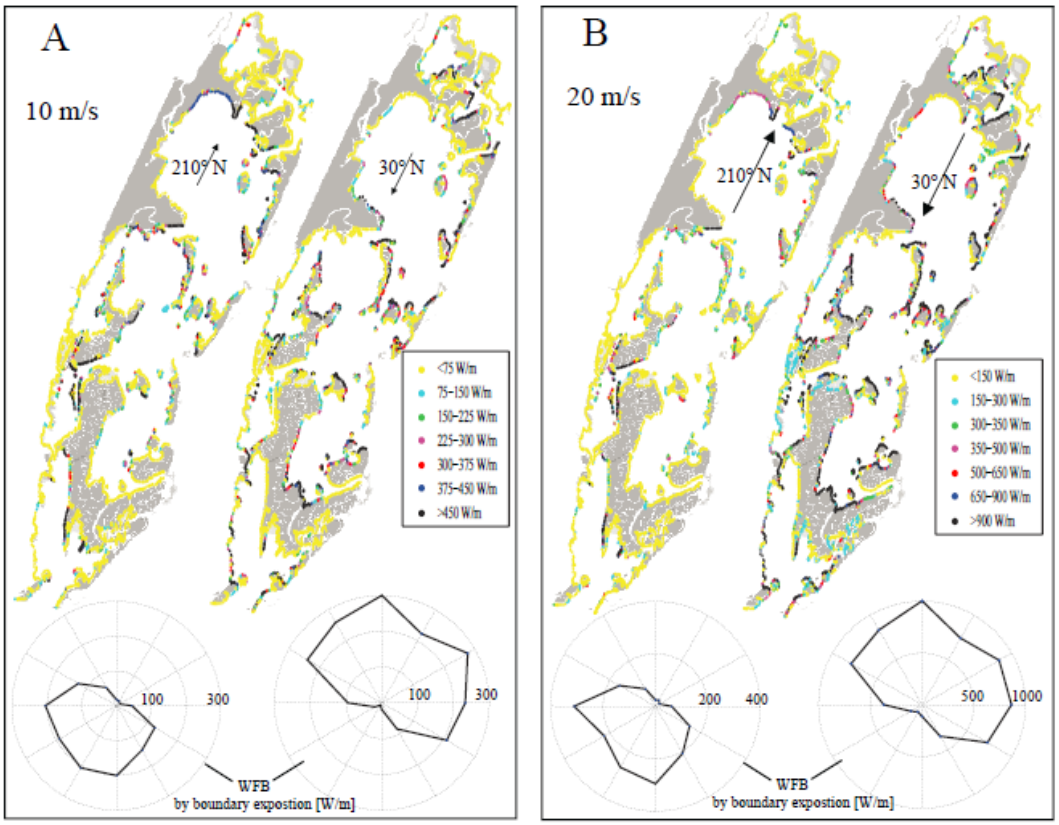

Figure 1.9: Wave power at the marsh boundary, averaged over 48 hours of simulations, calculated for different wind speeds and directions. A) wind speed of 10 m/s. B) wind speed 20 m/s. On the bottom WFB, for each wind condition, calculated as a function of marsh exposure.

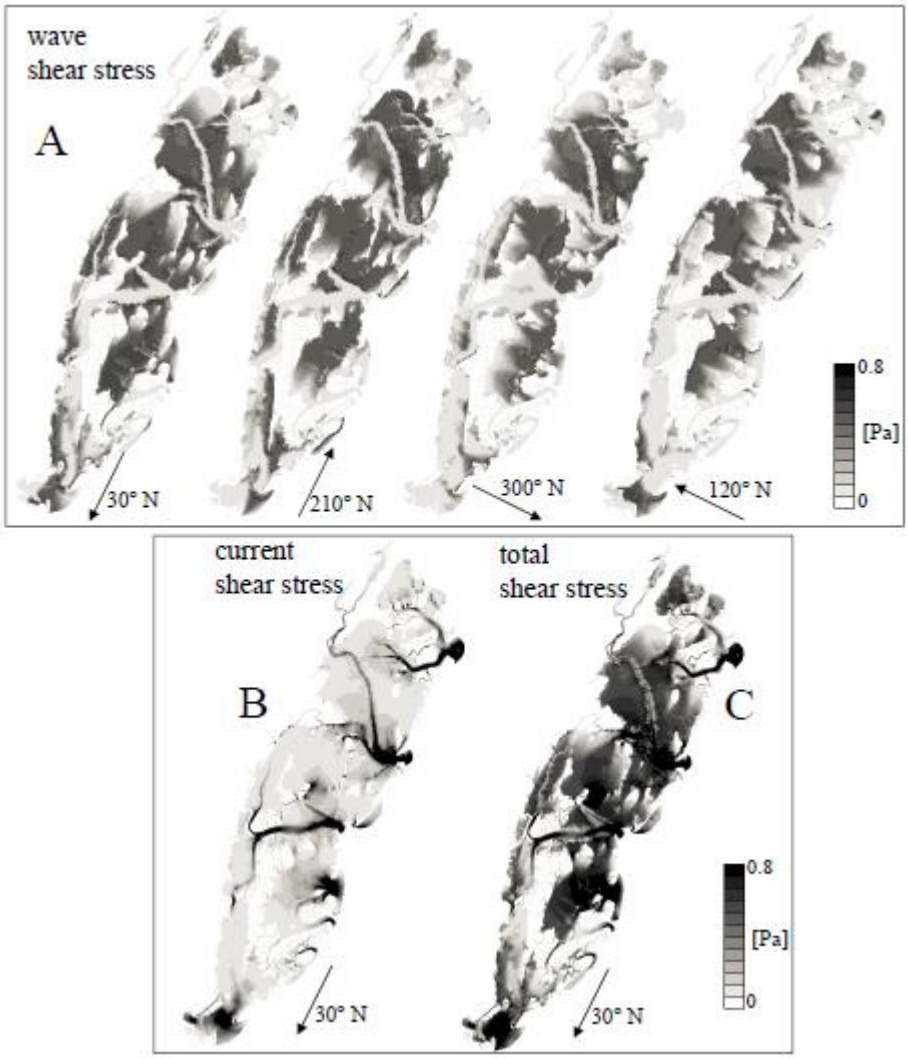

Figure 1.10: A) Wave induced bottom shear stress over the tidal flats, averaged over 48 hours of simulations, calculated for a wind speed of 10 m/s and four different directions (30, 120, 210 and 300 N). B) Current induced and C) total bottom shear stress for a wind speed of 10 m/s blowing from 30 N.

1.7 Wind statistics and wave action

Intertidal areas are subject to varying wind conditions and consequently to a range of erosion events, whose combination leads to their morphological evolution. To provide a

reliable estimate of the erosion stresses and wave energy to which the basin is subjected, it is necessary to correctly weight the relative importance of the different wind directions and intensities, according to their probability of occurrence at each coastal location.

We assume that the wind statistics in the years 1996-1999 are representative of the local meteorological conditions (Fig. 1.11A). The distribution of wind direction is not bimodal, with winds from 180-210° N and 330-60° N being more frequent.

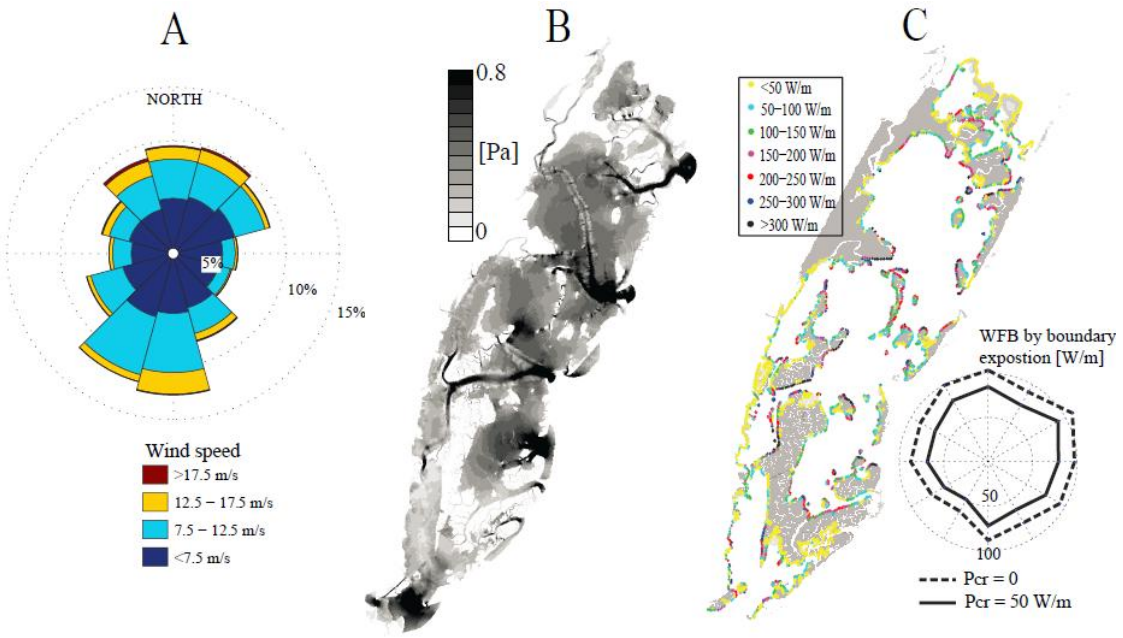

Figure 1.11: A) Wind statistics, binned by 4 speeds and 12 directions; data are from NOAA Station CHLV2 during 1996 to 1999. Total bottom shear stress on the tidal flats (B) and wave power at the marsh boundary with $P_{cr} = 0$ (C) weighted with the wind distribution in (A). Wave Factor at the marsh Boundary (WFB) as a function of marsh boundary exposure weighted with the wind distribution in (A), for P_{cr} equal to 0 and 50 W/m.

Values of bottom shear stress and wave power at the marsh boundary are weighted by the relative frequency of occurrence of the different wind conditions. This weighting

allows us to calculate the expected (or actual) erosion stresses, i.e. the most probable value of bottom shear stress and wave power in the basin. The expected bottom shear stress is greatest in the channels, especially near the inlets (Fig. 1.11B). Across the tidal flats, the expected bottom shear stress is quite homogeneous. Slightly higher values are found in the middle of the tidal flat, far from the marsh boundary. This happens because the EF is weighted over different wind directions, and therefore the area situated far from the boundary, which has the greatest fetch independently of wind direction, has on average higher waves.

The wave energy at the marsh boundary in contrast displays a clear pattern (Fig. 1.11C), with the highest values found on the marsh boundaries exposed toward the northeast. The asymmetry increases when the threshold value for wave erosion (P_{cr}) is set greater than zero. With a P_{cr} of 50 W/m the marsh boundary facing 0-90N receives 50% more wave power than the one facing 180 to 270 N.

1.8 Wave action and sea level rise

Our results indicate that the wave regime inside the lagoon is sensitive to water depth and therefore oscillations in sea level. The effect of RSLR is assessed herein by running a set of simulations with increased water elevations at the seaward boundary. As sea-level rises, both EF and WFB increase independent of wind direction (Fig. 1.12). However, the variation is almost negligible for EF while it is significant for WFB. For simplicity, we focus only on wind blowing from 30° N, which is typical for strong winds and produces high values for EF and WFB (Fig. 1.13). For every value of RSLR,

WFB increases almost 10 times more than EF. For example, for a RSLR of 20 cm, WFB increases by 30%, while EF increases less than 5% with respect to normal conditions.

We calculate the tidal prism by integrating the water discharge at the inlets over a tidal cycle. Tidal prism increases with RSLR (Fig. 1.12C): for example a RSLR of 15 cm increase the tidal prism by 5%, independently of wind direction.

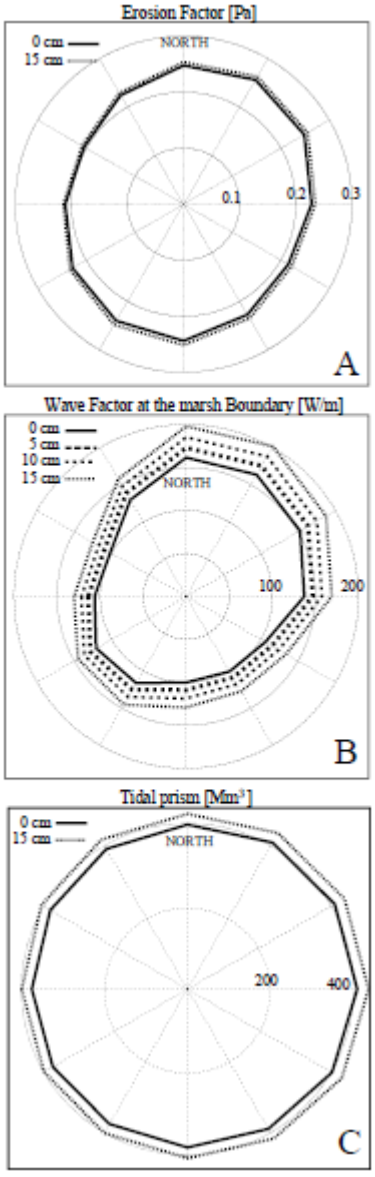

Figure 1.12: Erosion Factor and Wave Factor at the marsh Boundary calculated with a wind speed of 10 m/s and different values of RSLR.

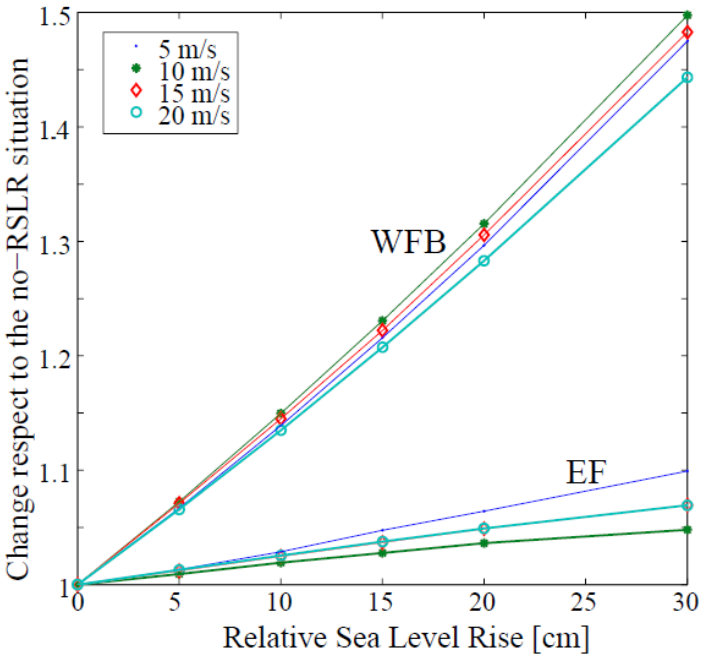

Figure 1.13: WFB and EF computed of a function of RSLR and normalized by the value of WFB and EF with no RSLR. The value are computed for 4 different wind speeds for one direction, 30° N.

1.9 Discussion

The model reproduces correctly water depth oscillations inside the lagoon. The best agreement between measured and calculated wave height is found at higher values of wind speed (Period #2, Fig. 1.3). Some disagreement in wave height is found at low wind speeds (Period #1, Fig 1.2), which could be explained by a higher spatial variability in the wind field that is characteristic of low wind conditions and is not detectable with a single wind measurement point.

The model assumes a steady wind forcing. For wind speed events with maximum winds speeds greater than 10 m/s and a maximum change in wind direction of ±30°, the average duration is 2.5 h (Table 2). This time interval is shorter than a tidal cycle (~12.4

hours), therefore averaging over a tidal cycle is not exact. However there is no correlation between water level and wind speed (r=0.04) which means that the same meteorological condition (i.e. wind speed) can occur at different moments during the tide oscillation when the basin is experiencing different water levels. Therefore we can assume that the average of the effect over the tidal cycle represents the ensemble average of different storm events forcing the lagoon at different moments.

Component		Wind angle defining an event [°]			
		30	60	90	180
Wind speed threshold defining an event [m/s]	5	2.9 h	4.3 h	5.1 h	14.1 h
	10	2.5 h	2.9 h	3.1 h	5.7 h

Table 1.2: Wind duration statistics. A wind event is defined as an uninterrupted sequence of wind conditions in which the wind speed does not go below the wind speed threshold and the direction does not change more than a specific angle respect to the initial direction.

Although wave-induced bottom shear stresses are larger than those induced by tidal currents, the latter plays a significant role in the bottom shear stress distribution by increasing the peak values of the bottom shear stress by up to 40% (Fig. 1.6). Therefore the use of a complete hydrodynamic model, which correctly reproduces tidal currents, is fundamental to study the morphological evolution of shallow water lagoons, and both components (waves and tidal currents) should always be taken into account.

The wave regime in shallow lagoons is controlled by wind conditions: wind speed determines the potential energy input to the waves, while wind direction determines the fetch, a proxy for the actual energy that can be transferred to the water body from the wind. Storm surge affects water level strongly in the lagoons (up to 0.6 m of super-elevation, Fig. 1.4) and wind-wave propagation and decay depend on water level (Eq 4). As a consequence, storm surge is a key factor controlling the wave regime in the lagoons. Because storm surge depends on wind conditions, (Fig 1.4), the global wave regime is correlated strongly with wind speed and direction. The dependence of EF on wind direction is mainly due to variations in fetch: EF is greatest for winds blowing along the main basin axis, which offers the longest fetch (Fig. 1.7B,1.8A). EF is also dependent on storm surge: positive (negative) storm surge results in higher (lower) EF. Storm surge has a dual effect on bottom shear stress. The effect of a positive (negative) storm surge is to increase (decrease) water depth, and to increase (decrease) wave height. Since higher (lower) wave heights augment bottom shear stresses, while higher (lower) water depths reduce them, the two processes compensate each other. The increase in EF associated with positive storm surge means that the wave effect is greater than the depth attenuation effect.

The dependence of WFB on wind direction is due to its association with storm surge: WFB is greatest for winds that produce the highest positive storm surge (Fig 1.8B,D), while lower values are found for negative storm surges. This tendency is explained by the monotonic relationship among water level, wave height, and wave power at the marsh boundary: positive (negative) storm surges increase water depth, which increases

(decreases) wave height leading to an increase (decrease) of wave power at the marsh boundary.

Computed wave energy is not uniform along the marsh boundary, but is greater where the boundaries are oriented toward the northeast (Fig. 1.11C). This result is in accordance with the distribution of WFB, which is maximal for wind blowing from NE (Fig 1.8B). This means that even if statistically there are two dominant winds blowing from opposite directions (Fig. 1.11A), the winds blowing from NE are predominant in determining the wave power at the marsh boundary. This distribution could induce an asymmetry in the marsh boundary erosion: assuming a constant erodibility over the whole marsh boundary, a higher erosion rate is expected on marsh boundaries that face the northeast. On the other hand, spatial variability in marsh erodibility, due to intrinsic differences in geotechnical properties as grain composition, compaction and vegetation, could induce a different trend in marsh boundary erosion. For example, marshes near barrier islands are likely to have a higher fraction of sand with respect to inner lagoon salt marshes. Further work will be done analyzing marsh characteristics and erosion rates at different sites.

The asymmetry in WFB is caused mainly by the asymmetry in storm surge (which is correlated with wind speed and direction, Fig. 1.4), rather than an asymmetry in basin geometry. Since storm surge is driven in part by regional upwelling/downwelling (e.g. Ekman transport), and not related specifically with this location, it is probable that other basins would experience the same asymmetry on WFB.

EF is more uniform across the basin than is WFB, with slightly higher values of EF far from the marsh boundaries than closer to them.

The effect of RSLR is to increase both EF and WFB (Fig. 1.12), however the response of WFB is about 10 times greater than that of EF (Fig. 1.13). The relationship among RSLR, water depth, wave height, WFB and EF is analogous to the case of storm surge. WFB increases monotically with wave height, which is enhanced by the greater water depth induced by RSLR. EF is affected positively by the increase in wave height, but negatively by the increase in water depth.

This dual behavior could affect the geomorphological evolution of the lagoon (Fig. 1.14). RSLR will increase the erosion at the marsh boundaries, accelerating their retreat. The effect on the tidal flats, even if small, is to increase erosion and thus deepen them. Since tidal flat deepening increases water depth, a positive feedback is established. On the other hand, an increase in WFB would accelerate marsh boundary retreat, thereby augmenting sediment availability in the basin. The fate of the eroded sediment is difficult to forecast because of the extreme mobility of the suspended sediment. However, we expect that an increase in sediment availability would increase the deposition rate in the tidal flats, creating a virtual decrease in RSLR and therefore a negative feedback.

The fate of the lagoon depends on the relative strength of these two feedbacks. If the erosion rate in the tidal flats is greater than the increased deposition rate, then a global positive feedback will be established and marsh retreat will accelerate until they disappear, while tidal flats will keep on deepening. A stable condition will eventually

occur only when tidal flats become deep enough to eliminate the effect of wave induced bottom shear stress (Fagherazzi et al., 2006; Marani et al., 2007; Carniello et al., 2009b).

On the other hand, if increased sediment availability increases deposition rates sufficiently to compensate for the increased bottom erosion, then a negative feedback will be established. This situation would lead to a temporary stable equilibrium, where the tidal flat depth is constant and RSLR is compensated by an increase in marsh boundary erosion rate. In this case, the morphologic evolution would again be characterized by marsh boundary retreat but at slower rate than for the previous scenario. The tidal flat equilibrium would last as long as the sediment supply by salt marsh retreatment balances tidal flat erosion.

Boundary erosion would also change the fetch distribution and therefore the wave field. However, since the waves are controlled more by water-depth than by fetch, and since the increase in fetch is small, this effect is not expected to be significant.

Positive RSLR increases the tidal prism (Fig. 1.12C). This is explained by the characteristic flat topographic profile of salt marshes: when they become flooded, a significant volume of water is added to the tidal prism. The enlarging of tidal prism by RSLR is in accordance with other studies (Mota Oliveira, 1970; O'Brien, 1969). In large estuaries, where hydrodynamics are controlled strongly by river discharge, an increase in water depth (by RSLR) results in lower currents (Meada, 1969), with a consequent reduction in sediment export and an increase in sedimentation, which compensate for the RSLR. In contrast, in shallow tidal bays lacking a significant source of freshwater

and sediment, like the VCR lagoons, an increase in tidal prism will strengthen the tidal currents and enlarge the size of the tidal inlet (Jarrett, 1976; D'Alpaos et al., 2010).

In the VCR offshore sources of sediment are small (Boon and Byrne, 1981; Nichols and Boon, 1994) from river discharge and associated sediment loads (Robinson, 1994; Nichols and Boon, 1994; Boynton et al., 1996). Sediment contributions from marsh erosion are larger, but still relatively small (Boon and Byrne, 1981; Nichols and Boon 1994): most of the sediment erosion, deposition and transport within the lagoons is associated with sediment redistribution. EF shows a little difference between flood and ebb (around few percent, result not reported), so sediment resuspension inside the lagoon will not differ significantly from flood to ebb. Given these conditions, an increase in the volume of water exchanged with the sea will increase sediment export. In addition, the increase in the tidal prism will increase the ebb-tidal delta volume (Walton and Adams, 1976), and remove sand from the lagoons system (FitzGerald et al., 2006). Therefore RSLR, through tidal prism increase, will enhance sediment export, which will add to the increase erosion of the tidal flat and marsh boundary.

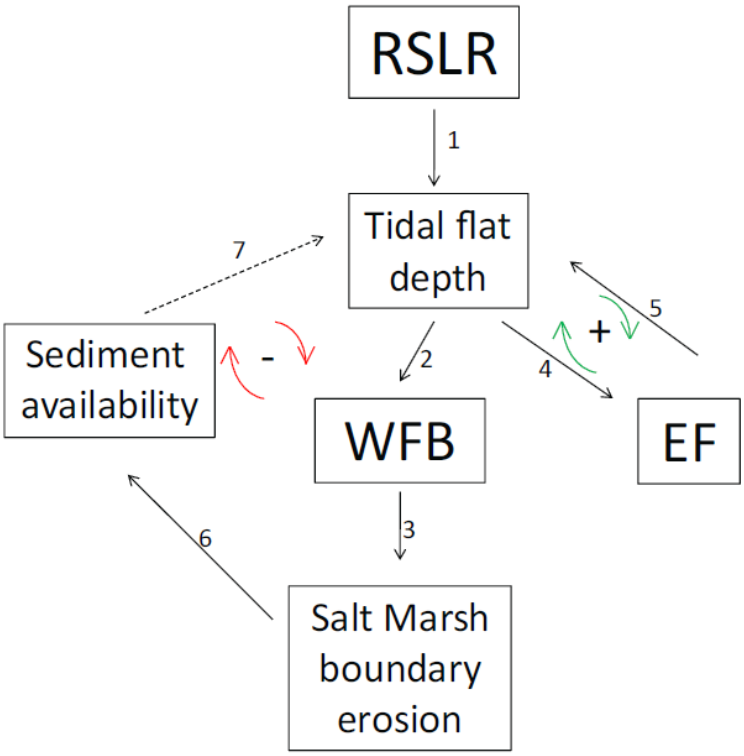

Figure 1.14: Effect of RSLR on basin morphology. RSLR increases water depth (1), which increases WFB (2), leading to marsh boundary erosion (3). Two feedbacks are present. Positive feedback: increasing water depth increases EF (4), which increases bottom erosion (5) Negative feedback: marsh erosion produces sediment (6), which deposit in the tidal flats and decrease water depth (7).

1.10 Conclusions

We applied the numerical hydrodynamic model WWTM to the lagoons of the Virginia Coast Reserve and we tested it with measured water levels and wave heights and periods. We used the model to forecast wave action within the lagoons for varying wind conditions and RSLR and drew the following conclusions:

1. For each wind speed, the total bottom shear stress over the tidal flats is driven by fetch, while the wave power at the marsh boundary is controlled by water depth. Storm

surge, by increasing water level inside the lagoons, plays a fundamental role in the marsh boundary erosion.

2. The expected wave power at the marsh boundary is greatest at the boundaries exposed toward the NE. Non-uniform marsh boundary erosion is therefore predicted in the lagoon system.

3. The effect of RSLR is to increase both tidal flat erosion (EF) and salt marsh boundary erosion (WFB). However, the relative increase in the latter is almost ten times greater than the former.

4. A positive feedback is expected between RSLR and lagoon bottom erosion because of the increase of EF, while a negative feedback is expected between RSLR and lagoon bottom erosion as a consequence of the sediment provided by marsh boundary deterioration. If the global feedback is positive, then salt marsh edges are eroded and tidal flats deepen in the basin. If the global feedback is negative, then the tidal flats find a temporary equilibrium state with RSLR thanks to the sediment supply from the marsh boundary erosion.

1.11 References

Allen, J., and P. Somerfield, and F. Gilbert, (2007), Quantifying uncertainty in high-resolution coupled hydrodynamic-ecosystem models. Journal of Marine Systems, 64, 1-4, 3-14.

Boon, J.D., (2004), Secrets of the tide, Horwood Publishing Limited, pp. 210.

Breugem, W.A., and L.H. Holthuijsen, (2007), Generalized Shallow Water Wave Growth from Lake George, Journal of Waterway, Port, Coastal, and Ocean Engineering, 133, 3.

Boon, J.D., and R.J. Byrne, (1981), On basin hypsometry and the morphodynamic response of coastal inlet systems, Marine Geology 40, 27-48.

Boynton, W.R., J.D. Hagy, L. Murray, C. Stokes, and W.M. Kemp, (1996), A comparative analysis of eutrophication patterns in a temperate coastal lagoon, Estuaries 19, 408-421

Cappucci S., C.L. Amos, T. Hosoe, and G. Umgiesser, (2004), SLIM: a numerical model to evaluate the factors controlling the evolution of intertidal mudflats in Venice Lagoon, Italy, Journal of Marine Sediments, 51, 257-280.

Carniello L., A. Defina, S. Fagherazzi, and L. D'Alpaos, (2005), A combined wind wave-tidal model for the Venice lagoon, Italy, Journal of Geophysical Research, 110, F04407.

Carniello, L., A. D'Alpaos, and A. Defina, (2009a), Simulation of wind waves in shallow microtidal basins: Application to the Venice Lagoon, Italy. Proceedings of 6th IAHR Symposium on River, Coastal and Estuarine Morphodynamics: RCEM 2009 – Vionnet C.A., Garcia M.H., Latrubesse E.M. and Perillo G.M.E. editors. Taylor & Francis Group, London, 2, 907-912.

Carniello, L., A. Defina, and L. D'Alpaos, (2009b), Morphological evolution of the Venice Lagoon: evidence from the past and trend for the future, Journal of Geophysical Research, 114, F04002.

CERC, Coastal Engineering Research Center, (1984), Shore Protection Manual, U.S. Army Coastal Engineering Research Center.

Christie, M.C., and Dyer, K.R., (1998), Measurements of the turbid edge over the Skeffling mudflats. In: Black, K.S., Paterson, D.M., Cramp, A. (eds) Sedimentary Processes in the Intertidal Zone. Geological Society, London, Special Publication 139, 45-55.

D'Alpaos, A., S. Lanzoni, M. Marani, and A. Rinaldo, (2010), On the tidal prism–channel area relations, Journal of Geophysical Research, 115, F01003.

D'Alpaos, L., and A. Defina, (2007), Mathematical modeling of tidal hydrodynamics in shallow lagoons: A review of open issues and applications to the Venice lagoon, Computers & Geosciences, 33, 476 – 496.

Defina, A., (2000), Two-dimensional shallow water equations for partially dry areas, Water Resource Research, 36, 3251– 3264.

Defina, A., L. Carniello; S. Fagherazzi, and L. D'Alpaos, (2007), Self organization of shallow basins in tidal flats and salt marshes, Journal of Geophysical Research, 112, F03001.

Emory, K.O., and D.G. Aubrey, (1991), Sea levels, land levels and tide gauges. Springer-Verlag, NY.

Fagherazzi S., L. Carniello, L. D'Alpaos, and A. Defina, (2006), Critical bifurcation of shallow microtidal landforms in tidal flats and salt marshes, Proceeding of the National Academy of Sciences, 103, 22, 8337-8341.

Fagherazzi, S., C. Palermo, M.C. Rulli, L. Carniello, and A. Defina, (2007), Wind waves in shallow microtidal basins and the dynamic equilibrium of tidal flats, Journal of Geophysical Research, 112, F02024.

Fagherazzi S., and P.L. Wiberg, (2009), The importance of wind conditions, fetch and water levels on wave generated shear stresses in a shallow intertidal basin, Journal of Geophysical Research, 114, F03022.

FitzGerald D.M., I.V. Buynevich, and B.A. Argow, (2006), Model of tidal inlet and barrier island dynamics in a regime of accelerated sea-level rise, Journal of Coastal Research, 39, 789–795.

Fredsoe, J., and R. Deigaard, (1993), Mechanics of Coastal Sediment Transport, Advanced Series Ocean Engineering, vol. 3, 392 pp., World Science, Singapore.

Emory, K.O., and D.G. Aubrey, (1991), Sea levels, land levels and tide gauges. Springer-Verlag, NY.

Jarrett, J.T., (1976), Tidal prism-inlet area relationships, General Investigation, Tidal Inlets Rep. 3, 32 pp., U.S. Army Coastal Engennering Research Center, Fort Belvoir, VA.

Hayden, B.P., M. Santos, G. Shao, and R. C. Kochel, (1995), Geomorphological controls on coastal vegetation at the Virginia Coast Reserve, Geomorphology, 13, 1– 4, 283 – 300.

Holthuijsen, L.H., N. Booij, and T.H.C. Herbers, (1989), A prediction model for stationary, short-crested waves in shallow water with ambient currents, Coastal Engineering, 13, 23-54.

Kamphuis, J.W., (1975), Friction factor under oscillatory waves, *Journal* of *Waterway*, Port, Coastal, and Ocean Engineering., 101, 135– 144.

Lawson, S.E., P.L. Wiberg, K.J. McGlathery, and D.C. Fugate, (2007), Wind-driven sediment suspension controls light availability in a shallow coastal lagoon, Estuaries and Coasts, 30, 1, 102-112.

Lawson, S.E., (2004), Sediment suspension as a control on light availability in a coastal lagoon, M.S. Thesis, University of Virginia, Charlottesville, VA, 119 pp.

Lawson, S.E., (2008), Physical and biological controls on sediment and nutrient fluxes in a temperate lagoon, Ph.D. Thesis, University of Virginia, Charlottesville, VA, 187 pp.

Le Hir, P., W. Roberts, O. Cazaillet, M. Christie, P. Bassoullet, and C. Bacher, (2000), Characterization of intertidal flat hydrodynamics, Continental Shelf Research, 20, 12-13, 1433-1459.

Marani, M., A. D'Alpaos, S. Lanzoni, L. Carniello, and A. Rinaldo, (2007), Biologically-controlled multiple equilibria of tidal landforms and the fate of the Venice lagoon, Geophysical Research Letter, 34, L11402.

Mariotti, G., and Fagherazzi S., (2010), A numerical model for the coupled long-term evolution of salt marshes and tidal flats, 115, F01004.

Moeller, I., T. Spencer, and J.R. French, (1996), Wave attenuation over salt marsh surfaces: Preliminary results from Norfolk, England, Journal of Coastal Research, 12, 4, 1009-1016.

Moller, I., T. Spencer, J.R French., D.J. Leggett, and M. Dixon, (1999), Wave transformation over salt marshes: A field and numerical modelling study from north Norfolk, England, Estuarine Coastal and Shelf Science, 49, 3, 411-426.

Mota Oliveira, I.B, (1970), Natural flushing ability in tidal inlets, Proceeding Coastal Engineering Conference, 12th, Washington, DC, 3, 1827–1845. Washington, DC.

Nerem R., T. van Dam, and M. Schenewerk, (1998), Chesapeake Bay subsidence monitored as wetland loss continues. EOS, 79, 156–157.

Nichols, M.M., and J.D. Boon, (1994), Sediment transport processes in coastal lagoons, in Coastal Lagoon Processes, B. Kjerfve editor, Elsevier, 157-217.

Oertel, G.F., G.T.F. Wong, and J.D. Conway, (1989), Sediment accumulation at a fringe marsh during transgression, Oyster, Virginia, Estuaries 12, 18-26.

Oertel, G.F., (2001), Hypsographic, hydro-hypsographic and hydrological analysis of coastal bay environments, Great Machipongo Bay, Virginia, Journal of Coastal Research, 17, 4, 775-783.

Press, W.H., S.A. Teukolsky, W.T. Vetterling and B.P. Flannery, (1992), Numerical Recipes (second ed.), Cambridge University Press, Cambridge, UK.

Robinson, S.E., (1994), Clay mineralogy and sediment texture of environments in a barrier island-lagoon system, M.S. Thesis, University of Virginia, 102pp.

Schwimmer, R.A., (2001), Rates and Processes of Marsh Shoreline Erosion in Rehoboth Bay, Delaware, U.S.A., Journal of Coastal Research, 17, 3, 672-683.

Schwimmer, R.A., and J.E. Pizzuto, (2000), A Model for the Evolution of Marsh Shorelines, Journal of Sedimentary Research, 70, 5, 1026-1035.

Soulsby, R.L., (1995), Bed shear-stresses due to combined waves and currents, in Advances in Coastal Morphodynamics, edited by M.J.F. Stive et al., pp. 4-20 – 4-23, Delft Hydraul., Delft, Netherlands.

Soulsby, R.L., (1997), Dynamics of Marine Sands: A Manual for Practical Applications, 248 pp., Thomas Telford, London.

Tilburg, C.E., and R.W. Garvine, (2004), A Simple Model for Coastal Sea Level Prediction, Weather and Forecasting, 19, 3, 511-519.

Umgiesser, G., D.M. Canu, A. Cucco, and C. Solidoro, (2004) A finite element model for the Venice Lagoon, Development, set up, calibration and validation. Journal of Marine Systems, 51, 1-4, 123-145.

Whitehouse, R.J.S., and H.J. Mitchener, (1998), In: Black, K.S., Paterson, D.M., Cramp, A. (eds) Sedimentary Processes in the Intertidal Zone. Geological Society, London, Special Publication 139, 45-55.

Young, I.R., and L.A. Verhagen, (1996), The growth of fetch-limited waves in water of finite depth. Part 1: Total energy and peak frequency, Coastal Engineering, 29, 1–2, 47–78.

Chapter 2. A numerical model for the coupled long-term evolution of salt marshes and tidal flats

The contents of this chapter were published in 2010 in Journal of Geophysical Research – Earth Surface. This paper was co-authored with S. Fagherazzi (Department of Earth Science, Boston University).

Abstract

A one dimensional numerical model for the coupled long-term evolution of salt marshes and tidal flats is presented. The model framework includes tidal currents, wind waves, sediment erosion and deposition, as well as the effect of vegetation on sediment dynamics. The model is used to explore the evolution of the marsh boundary under different scenarios of sediment supply and sea-level rise. Numerical results show that vegetation determines the rate of marsh progradation and regression, and plays a critical role in the redistribution of sediments within the intertidal area. Simulations indicate that the scarp between salt marsh and tidal flat is a distinctive feature of marsh retreat. For a given sediment supply the marsh can prograde or erode as a function of sea-level rise. A low rate of sea-level rise reduces the depth of the tidal flat increasing wave dissipation. Sediment deposition is thus favored and the marsh boundary progrades. A high rate of sea-level rise leads to a deeper tidal flat and therefore higher waves that

erode the marsh boundary, leading to erosion. When the rate of sea-level rise is too high the entire marsh drowns and is transformed into a tidal flat.

2.1 Introduction

Intertidal salt marshes are among the richest ecosystems in terms of productivity and species diversity, providing habitat to a diverse fauna population, important resources for fishing and recreation, and a storm buffer at the land-sea interface (Allen 2000; Fagherazzi et al., 2004). Salt marshes are increasingly threaten by sea-level rise, variations in storm activity, and land use. The extension of marshes in shallow coastlines is controlled by the repartition of sediments between tidal flats and marsh platform, and by the dynamics of the marsh boundary (van de Koppel et al., 2005). As a results salt marshes co-evolve with tidal flats in the intertidal area (Fagherazzi et al., 2006), and only a holistic approach encompassing the two landforms as well as the feedbacks between morphodynamics and ecology can determine the future trajectory of the system.

The processes that control sediment mobility are primarily physical: erosion, transportation and deposition induced by purely hydrodynamic forcing, like tidal currents and wind waves (see Fagherazzi et al., 2007). However, often biota interacts with sediment dynamics, strongly effecting the morphology of intertidal landscapes (Le Hir et al., 2007).

Physical and biological processes are non-linear and tightly coupled. Marsh elevation (Morris et al., 2002), as well as wave exposure (van de Koppel et al., 2005), influence

vegetation growth. Plants regulate sediment erodability and trapping (Le Hir et al., 2007), organogenic production (Blum and Christian, 2004), and wave dissipation (Möeller, 2006). These feedbacks produce complex dynamics in the coupled marsh-tidal flat evolution. One emergent feature from these dynamics is a vertical scarp separating salt marshes and tidal flats. Once the scarp is formed, local erosional processes such as piping, sapping, and bank failure take place, modifying the rate of marsh regression and ultimately the total extension of marsh surfaces along the coastline.

Several numerical models for the evolution of intertidal landforms have been proposed in the recent past. Pritchard et al. (2002) developed a cross-shore mudflat model that takes into account tidal effects; Waeles et al. (2004) incorporated in the same framework wind waves. Le Hir et al. (2007) focused on the effect of vegetation, introducing mud strengthening by microphytobenthos and hydrodynamic damping by saltmarshes. All these models utilize a very large spatial grid (elements larger than 100m), which is suitable to study the large scale profile of tidal flats, but it does not permit the description of local features, like a vertical scarp, whose horizontal characteristic length scale is on the order of meters. In recent years, a new generation of models coupling biology to morphodynamics has been developed for intertidal areas (Mudd et al., 2004). For example, the model proposed by Kirwan and Murray (2007) for the tidal marsh platform evolution couples erosion by tidal current and sediment deposition with vegetation. In a similar way D'Alpaos et al. (2006) modeled the cross section of a tidal channel coupling tidal flow, distributed shear stress, and vegetation. In

both cases the vegetation was a function of elevation and therefore was linked to the morphological evolution of the system.

In the context of marsh boundary erosion, van de Koppel (2005) presented a model that simulates the evolution of the scarp boundary as a function of vegetation biomass and waves. This simple model, based on few phenomenological equations, is extremely effective in capturing the long-term evolution of the system and paved the way to a new generation of high resolution models, which will include a physically based description of the processes at play. Here we expand this approach by including wave generation and propagation, tidal oscillations, sediment transport, and the feedbacks between vegetation and sediment deposition. The model couples two distinct modules for salt marsh and tidal flat morphodynamics through the exchange of sediments and the erosion/progradation of the marsh boundary.

We utilize a ecogeomorphic model of salt marsh evolution which includes feedbacks between marsh vegetation and sediment transport (see Fagherazzi and Sun, 2003; D'Alpaos et al., 2005; D'Alpaos et al., 2006). The model couples a hydrodynamic module to the vegetation framework delineated by Morris et al. (2002) and Mudd et al. (2004) to quantify the feedbacks between vegetation and sediment fluxes. Specifically, vegetation biomass, belowground production, and sediment trapping by plants are all implemented as a function of marsh elevation and allowed to co-vary over time with marsh landforms. In the tidal flats we use a previously developed model, which quantifies the influence of tidal currents and wind waves on tidal flat equilibrium (Fagherazzi et al., 2006; Fagherazzi et al., 2007; Defina et al., 2007). The model

accounts for sediment deposition and sediment resuspension by wind waves as a function of bottom characteristics, as well as for the erosion of the marsh scarp produced by breaking waves.

2.2 Coupled Salt Marsh-Tidal Flat Model

The numerical model is implemented on an intertidal transect perpendicular to the marsh boundary which includes both a tidal flat and a marsh platform (Fig. 2.1). The transect is divided into N cells of width Δx, set equal to 0.1 m to have enough spatial resolution. $z_g(i)$ and $y(i)$ are the bottom elevation and the water depth associated with the cell i (Fig. 2.1). An open ocean or tidal basin is assumed on the right boundary ($i = N$), from where wind and tides propagate into the domain. An impermeable wall is assumed on the left boundary, corresponding to upland ($i = 1$).

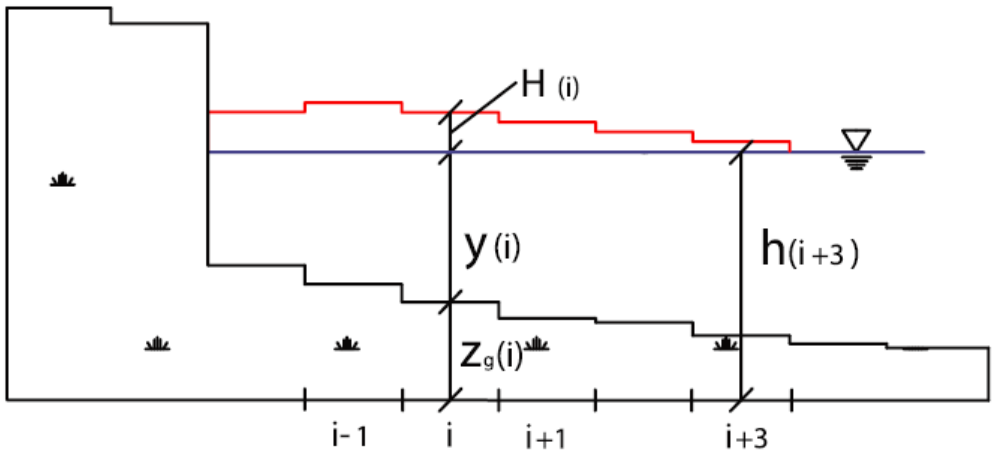

Figure 2.1: Model geometry. The tidal flat/salt marsh transect is divided into cells of width dx. The cells are numerated from left to right.

The physical processes included in the domain are: wind induced waves, tidal currents, sediment erosion, transport and deposition. The model takes also into account the dynamics of marsh vegetation and its feedbacks with erosion and deposition processes.

2.2.1 Wind induced waves, tides and related bottom shear stresses

Wave propagation is described by the one dimensional equation of wave energy conservation at steady-state:

$$c_g \frac{dE}{dx} = S \text{ , (Eq. 2.1)}$$

where E is the wave energy, $c_g = \frac{\sigma}{2k}\left(1+\frac{2ky}{\sinh(2ky)}\right)$ is the wave-group celerity, y the water depth, σ the wave frequency, and k the wave number. The source term S is described by the following equation:

$$S = S_w - S_{bf} - S_{wc} - S_{brk} \text{ , (Eq. 2.2)}$$

where S_w is the wave growth by wind action on the water surface, and the other terms are the dissipation of wave energy by bottom friction (S_{bf}), whitecapping (S_{wc}) and depth induced breaking (S_{brk}). The source term can be expressed as a function of wind speed (blowing from right to left), water depth and wave energy; it reads:

$$S = \alpha + \beta E - 2C_f \frac{k}{\sinh(2ky)} E - c\sigma\left(\frac{\gamma}{\gamma_{PM}}\right)^m E - \frac{2a}{T} Q_b \left(\frac{H_{max}}{H}\right)^2 E \text{ , (Eq. 2.3)}$$

The values of the parameters α and β depend on the wind speed U, C_f is a dissipation coefficient, γ is the integral wave steepness parameter, i.e. $\gamma = E\sigma^4 / g^2$, σ is the relative frequency, γ_{PM} is the theoretical value of γ for a Pearson-Moskowitz spectrum, Q_b is the probability that waves with height *H* will break, *T* is the wave period, *c*, *m* and α are empirical parameters. The numerical values of the parameters utilized to solve Eq. 2.3 are reported in Fagherazzi et al. (2006) and Carniello et al. (2005).

Eq. 2.1 is solved imposing an energy wave value equal to zero at the seaward boundary and propagating the wave energy along *x* using an upwind scheme in space:

$$E(i-1,t) = E(i,t) + S(i,t)\Delta x / c_g(i,t), \text{ (Eq. 2.4)}$$

where *i* is the element location (see Fig. 2.1). From the linear wave theory the wave height is derived from the wave energy, $H = \sqrt{8E/\rho g}$, where g is the gravitational acceleration and ρ the water density. The bottom shear stress induced by the wave is calculated using the computed wave height (Fredsoe and Deigaard 1992):

$$\tau_{wave} = \frac{1}{2} f_w \rho \left(\frac{\pi H}{T \sinh(ky)} \right)^2, \text{ (Eq. 2.5)}$$

where f_w is a friction factor and T is the wave period, assumed constant during propagation. For computational stability the shear stress induced by waves is set equal to zero when the water depth is shallower than 1 cm. Given the small dimension of the domain, the tide is assumed to propagate with infinite speed, therefore we set the water

level h equal at every point of the domain and varying only in time following tidal oscillations. The tide is assumed harmonic and semidiurnal, without spring-neap modulation:

$$h(t) = A\sin\left(t\frac{2\pi}{12}\right) \quad \text{,(Eq. 2.6)}$$

where A is half of the tide range and t is time in hours.

Tidal currents are calculated with a quasi-static model, based on the continuity equation:

$$Q(i+1,t) = Q(i,t) - \frac{\Delta y}{\Delta t}\Delta x \quad \text{, (Eq. 2.7)}$$

where y is the water depth, equal to $h - z_g$ (and zero if $h < z_g$), Q is a discharge per unit width, positive if directed rightward, and assumed equal to zero on the landward boundary, i.e. $Q(i=1,t) = 0$.

Bottom shear stress induced by the tidal current is calculated with an equation for uniform flow:

$$\tau_{curr} = C_f \rho (Q/y)^2 \quad \text{, (Eq. 2.8)}$$

where ρ is the water density and C_f is a friction coefficient set equal to 0.01 (Fagherazzi et al., 2007). The total bottom shear stress is calculated as a nonlinear combination of wave shear stress and tidal current shear stress (Soulsby, 1997):

$$\tau = \tau_{wave} + \tau_{curr}\left[1+1.2\left(\frac{\tau_{wave}}{\tau_{curr}+\tau_{wave}}\right)^{3.2}\right], \text{ (Eq. 2.9)}$$

2.2.2 Sediment erosion and deposition

The evolution of the tidal flat bottom is governed by erosion and sedimentation processes, according to the Exner equation:

$$\rho_b \frac{dz_g}{dt} = D - R \text{ , (Eq. 2.10)}$$

where ρ_b is the sediment density, D is the sedimentation rate and R is the erosion rate. The erosion term is the sum of two terms:

$$R = R_{shear} + R_{break} \text{, (Eq. 2.11)}$$

The first term is given by bottom shear stresses induced by waves and currents, whereas the second term captures the effect of turbulence generated by wave breaking. The simplest and widely used formulation for bottom erosion is:

$$R_{shear} = \begin{cases} 0 & \tau < \tau_{cr} \\ \alpha(\tau - \tau_{cr}) & \tau > \tau_{cr} \end{cases} \text{ , (Eq. 2.12)}$$

where α is the erosion rate and τ_{cr} is the critical shear stress. The second term, R_{break}, takes into account the localized erosion induced by the breaking of the waves.

We propose a formulation with the structure of the classical erosion equation, using wave power as main variable:

$$R_{break} = \begin{cases} 0 & P < P_{cr} \\ \beta(P - P_{cr})/d & P > P_{cr} \end{cases} \quad ,(\text{Eq. } 2.13)$$

where β is a constant parameter, P is the wave power per surface unit dissipated by breaking, P_{cr} is a threshold value for erosion, and d is the length over witch the erosion by wave breaking takes place, here equal to the cell length.

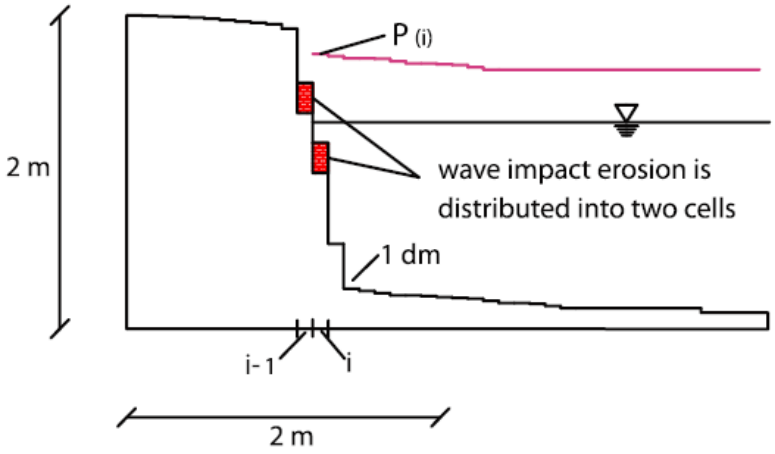

Figure 2.2: Schematic of the wave impact erosion on a vertical scarp.

Contrary to bottom erosion, which is a continuous process for a given wave forcing, scarp erosion is a discontinuous process, with removal of surface particles superimposed to scarp failure and mass wasting. For example, Allen (1989) showed that scarp erosion chiefly occurs through toppling and rotational slip. Moreover, vegetation has a strong role in scarp resistance and erosion mechanisms, and clearly its influence cannot be addressed with a standard wave breaking formulation on a gentle slope.

To our knowledge, there are no detailed models that describe the physics of the erosion of a cohesive marsh scarp by wave attack. The equation that relates sediment erosion to

excess shear stress (Eq. 2.12) cannot be used on a vertical scarp since the shear tensor is different than the one acting on a horizontal bottom. In fact, while at the bottom only the tangential shear stress is present (excluding the constant hydrostatic pressure), on the vertical scarp both tangential and normal stresses promote erosion.

Given the complexity of the process of scarp erosion, a heuristic approach based on only one parameter seems a better choice for a long-term model of marsh evolution. This parsimonious strategy is commonly adopted in geomorphic models of river meanders, in which the erosion of vegetated river banks is simply set proportional to the flow velocity at the river outerbank (Pizzuto, 1989; Seminara, 2006). Similarly, Schwimmer (2001) correlates the long term erosion rate of marsh scarps to the averaged wave power.

We thus propose to use the same equation for bottom erosion by wave breaking (Eq. 2.13), in which the term P is set equal to the rate of power dissipation by wave impact at the marsh scarp. When the wave encounters a vertical wall, the water depth becomes suddenly equal to zero, and the breaking is localized in a a small area in which the wave loses all its energy. In this case the breaking energy should be spread along a vertical surface, which cannot not be represented in a 1D model. To reproduce this process, we distribute the breaking energy into the two cells defining the scarp, namely the one above and the one below the point where the water encounters the bottom (see Fig. 2.2). Operatively, we set the value of P equal to Ec_g to both cells in Eq. 2.13, where the wave energy and the group celerity are calculated in the last cell with water depth greater than zero, and d is equal to two cell lenghts.

With this formulation the erosion by wave impact does not induce a horizontal migration of the scarp, but rather a vertical erosion of a cell column. However, by splitting the erosion into two cells and using a fine spatial resolution (0.1 m), we obtain a macroscopic result that well agrees with the characteristics of scarp erosion by lateral migration (Fig. 2.2). It should be stressed that scarp erosion is a complex phenomenon, which takes place both by gradual regression of the scarp, and by macroscopic failures. Our formulation could be seen as the average result of the two processes.

We use a value for P_{cr} that ranges from 3 W to 15 W, depending on vegetation. These values correspond to a range of wave height of 7-15 cm (assuming a wave group celerity of 0.5 m/s, which is a common value in front of marsh boundaries). This range of wave height matches the range of threshold values individuated by Trenhaile (2009) in his model for steeply sloping bluff retreat by broken wave impact. The value of β is calibrated empirically to have a regression rate of the order of m/yr. We recognize that further study have to be performed to determine the role of geotechnical parameters on scarp erosion.

The sedimentation rate is estimated with the formula of Einstein and Krone (1962):

$$D = \begin{cases} 0 & \tau > \tau_d \\ w_s r C \left(1 - \dfrac{\tau}{\tau_d}\right) & \tau < \tau_d \end{cases} \quad \text{, (Eq. 2.14)}$$

where w_s is the settling velocity, r is an empiric coefficient set equal to 2 (Parker et al., 1987), τ_d is the shear stress below which the sediment deposits.

The average sediment concentration in the water column is calculated by imposing the conservation of mass:

$$\frac{\partial(yC)}{\partial t}+\frac{\partial(QC)}{\partial x}+\varsigma\frac{\partial^2(yC)}{\partial x^2}=R-D\text{, (Eq. 2.15)}$$

where ς is the diffusion coefficient, and C is the sediment concentration.

The advection-diffusion equation is discretizated in space with a central difference scheme for the diffusion term and with an upwind method for the advection term. For stability purposes the system is solved implicitly in time. The resulting non-symmetric linear system is solved with a preconditioned biconjugate gradient method. In addition, for computational efficiency, the cells used for the advection-diffusion equation is larger (2 m) than the bottom cells (0.1 m).

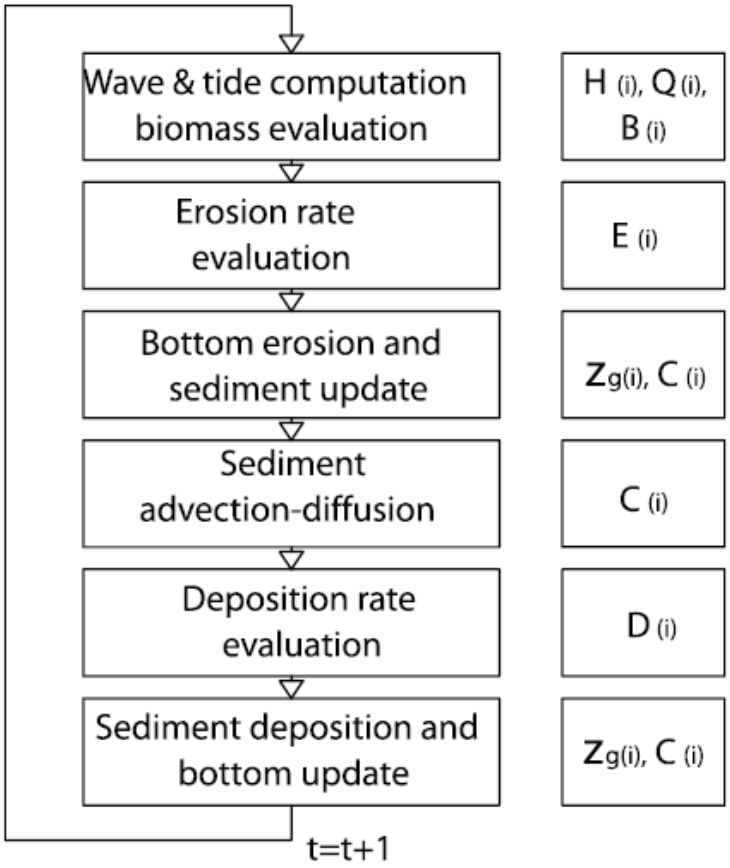

Figure 2.3: Model flowchart.

2.2.3 Vegetation processes

The presence of vegetation greatly modifies erosion and deposition processes on the marsh platform. The vegetation canopy decreases wave height and current velocity; roots increase the sediment resistance to erosion, vegetation biomass favors mineral sediment trapping and promotes belowground organic production.

Mudd et al. (2004) modeled all these processes as a function of aboveground biomass B. Using the data of Morris et al. (2002), Mudd et al. (2004) described the biomass as a

function of the elevation relative to the tide, D, defined as the difference between the HAT (highest astronomical tide) and the ground elevation. This value is biunivocal linked to the time fraction during which the vegetation is submerged (Mudd et al., 2004). The biomass is zero when is submerged for too long (D_{max}), and when it is not submerged long enough (D_{min}). Following Morris (2006) we assume that vegetation biomass varies parabolically within D_{min} and D_{max}:

$$B_{ps} = \begin{cases} 0 & D < D_{min} \\ B_{\max}(aD + bD^2 + c\ ) & D_{min} < D < D_{max} \\ 0 & D > D_{max} \end{cases} \quad \text{, (Eq. 2.16)}$$

The parameters *a,b,c* are chosen in order to have *B* equal to zero at $D = D_{max}$ and $D = D_{min}$, and equal to B_{max} at the parabola maximum.

Vegetation biomass varies through the seasons, peaking in the summer months, as shown by Morris and Haskin (1990). Mudd et al. (2004) proposed the following formulation:

$$B = \frac{B_{ps}(1-\omega)}{2}\left[\sin\left(\frac{2\pi m}{12} - \frac{\pi}{2}\right) + 1\right] + \omega B_{ps}\text{, (Eq. 2.17)}$$

where B is the biomass, m is the month, with $m = 1$ corresponding to January, and ω is a dimensionless factor.

Vegetation increases the sediment's resistance to erosion by stabilizing the substrate with a root mat. In our model we linearly correlate the increase of erosion threshold with the aboveground biomass:

$$\tau_{cr} = \tau_{cr}(1 + K_{veg} B/B_{max}), \text{ (Eq. 2.18)}$$

where K_{veg} is a nondimensional parameter.

Vegetation plays also a role in the erodability of the scarp. Only the top layer of marsh cliffs is resistant, because a dense root mat of marsh grasses binds the sediments together. We assume that the rootmat is directly related to the above ground biomass, and that once the biomass is removed, also the roots (or their stabilizing effect) disappear. Moreover, we assume that vegetation linearly increases the critical energy P_{cr} for wave erosion as a function of biomass (see Eq. 2.13)

$$P_{cr} = P_{cr}(1 + K_{veg} B/B_{max}), \text{ (Eq. 2.19)}$$

Vegetation influences sedimentation processes as well, by increasing the sediment trapping efficiency, and the belowground organogenic production.

The vegetation effect on the sedimentation rate is expressed by:

$$D = D_s + D_t, \text{ (Eq. 2.20)}$$

Where D_s is the sedimentation rate due only to settling. The rate of sediment trapped by vegetation D_t is expressed by the following equation:

$$D_t = Cu\eta d_s n_s h_s, \text{ (Eq. 2.21)}$$

where u is a typical value of the flow speed through vegetation, η is the rate at which transported sediment particles are captured by plant stems, d_s is the stem diameter, n_s is the stem density per unit area, and h_s is the average height of the stems. Accordingly to the formula proposed by Palmer et al. (2004) , the capture efficiency η reads:

$$\eta = 0.224\left(\frac{ud_s}{\nu}\right)^{0.718}\left(\frac{d_p}{d_s}\right)^{2.08} \text{, (Eq. 2.22)}$$

where d_p is particle diameter, and ν is the water kinematic viscosity.

The values of stem density per unit area, n_s, stem diameter, d_s, and average stem height, h_s, are expressed as a function of the above ground biomass B (Mudd et al., 2004):

$$\begin{aligned} n_s &= 250B^{0.3032} \\ h_s &= 0.0609B^{0.1876} \\ d_s &= 0.0006B^{0.3} \end{aligned} \quad \text{, (Eq. 2.23)}$$

Above ground biomass also promotes organogenic sediment production. The linear relationship between organogenic sedimentation and biomass presented by Randerson (1979) is chosen in this model:

$$z_g = z_g + k_b B/B_{max}\Delta t \text{ , (Eq. 2.24)}$$

where k_b is the maximum sedimentation rate.

The vegetation canopy on the marsh surface attenuates wind waves. Möeller (2006) studied wave attenuation induced by marsh vegetation in a UK saltmarsh, finding a

correlation between wave attenuation and the ratio wave height/water depth. Wave attenuation over a 10 m transect varied from 0.008% to 33%, depending on water depth and vegetation. For simplicity, we assume that the relative attenuation per unit of length along the direction of propagation is proportional to the vegetation biomass, with a maximum value of 3% per meter when the maximum biomass is reached. The relationship is:

$$H_{reduction}(\%) = 3\frac{B}{B_{max}} L_{Att} \text{ , (Eq. 2.25)}$$

where L_{Att} is the length along which the wave propagates, expressed in meter.

2.2.4 Computational scheme

At every time step both the bottom elevation z_g and the water depth y are held constant in every cell, while wave height, tidal current, and total shear stress are computed with Eqs. 3, 7 and 9 respectively. The erosion rate is calculated with Eq. 2.11 and the bottom elevation and suspended sediment are updated maintaining the mass balance:

$$z_g^{\,t+1/2} = z_g^{\,t} - R\Delta t/\rho_b \quad C^{t+1/2} = C^t + R\Delta t / y^t \text{ , (Eq. 2.26)}$$

The advection-diffusion equation (Eq. 2.17) is applied for a time step, then the sedimentation rate is calculated and the bottom elevation and the suspended sediment are updated:

$$z_g^{\,t+1} = z_g^{\,t+1/2} + D\Delta t/\rho_b \quad C^{t+1} = C^{t+1/2} - D\Delta t / y^t \text{ . (Eq. 2.27)}$$

Finally the biomass is recalculated as a function of elevation. The computational flowchart is presented in Fig. 2.3.

In order to have sufficient resolution during a full tidal cycle, a time step $dt = 30\,\text{min}$ is chosen. To reduce the simulation time we use a highermodel resolution during strong wind conditions and a lower model resolution during weak wind conditions. The simulation is divided into storms, during which the wind speed U is greater than a certain threshold, and fair-weather conditions, during which the wind speed is zero. The simulation is a sequence of storms and fair-weather periods, with duration *d* and *L* respectively (Fig. 2.4). During a storm the model runs with resolution Δt . During fair weather the system evolution is computed using only two tidal cycles, both calculated with resolution Δt and wind speed set to zero. In the first cycle the model is run normally, in the second cycle the model is run using a multiplying factor for sedimentation. This allows simulating sediment deposition with less computational time.

The wave height at the seaward boundary cell is not imposed, but it is calculated propagating an initial wave of 1 cm height over a horizontal flat with water depth equal to the water depth at the seaward boundary cell. This allows the utilization of an arbitrary wind fetch without increasing too much the computational effort. During the simulation the fetch length has been kept equal to 3 km.

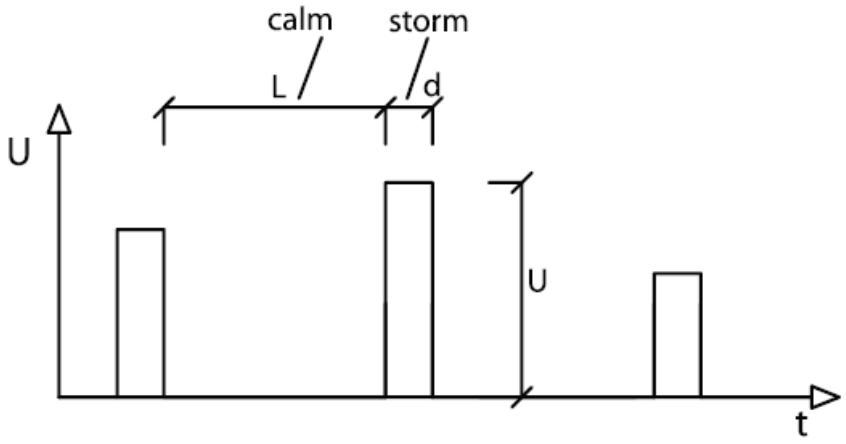

Figure 2.4: Numerical represenation of wind events. Periods with constant wind velocity U are spaced by periods of fair weather ($U = 0$).

Three sets of simulations are performed, with different scenarios of sediment availability. All simulations are run with and without vegetation, maintaining constant all the other parameters. The wind speed is assumed to be a random variable uniformly distributed between 0 and 20 m/s, the duration of the storm times, d, are 12 hours, the duration of the calm times, L, are 10 days, the wave period, T, is 2 s, the tidal amplitude, A, is 2 m.

In the first set of simulations the total mass of sediment is maintained constant and conservative boundary conditions for the advection-diffusion equation are used. Specifically, the maximum possible deposition in each cell is limited to the volume of suspended sediment in the water column above that cell. The model starts with an initial condition of a tidal flat with a gentle slope (3:1000) below MSL and no sediment in suspension. The simulation is run until a steady configuration is reached after 200 years.

Figure 2.5 shows the steady state profiles with and without vegetation. In both cases the tidal flat evolves into a concave-up profile, with a marsh (or an unvegetated terrace in the simulation without vegetation) that forms on the the upper part of the profile, at the landward side. The elevation of the salt marsh is close to HAT (highest astronomical tide with a gentle slope (2:1000). The transition between tidal flat and salt marsh takes place with a variation of the profile slope. In the simulation without vegetation the transition is gentle, with a gradual change from a convex up to a concave up profile. When the vegetation is present the slope increases from 2:1000 to 2:1 in few meters, creating a scarp.

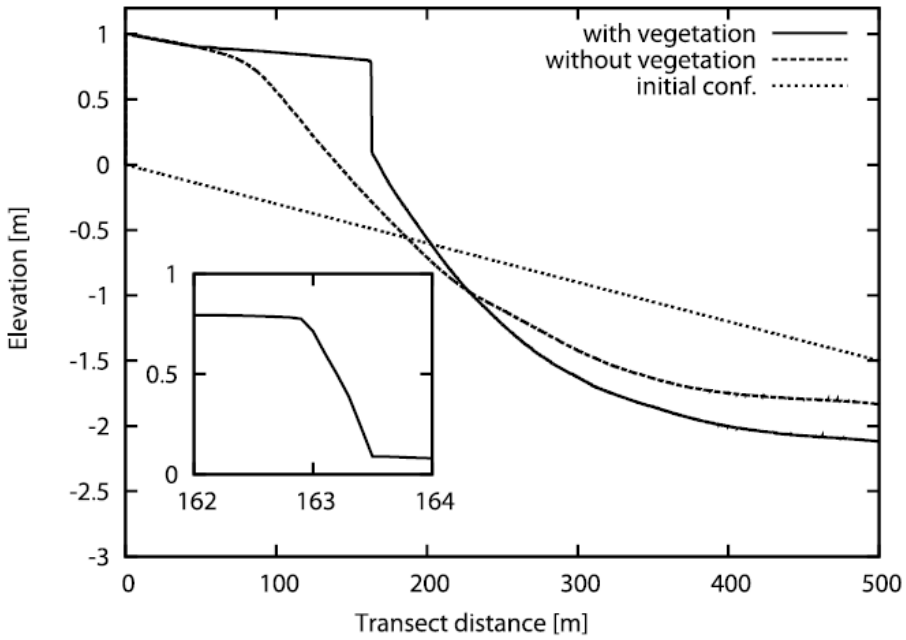

Figure 2.5: Steady intertidal profile after 200 years of simulation. The initial topography was a gently sloping tidal flat below mean sea level. The total amount of sediments is conserved during the simulation. The square inside the figure show a details of the marsh boundary.

In order to evaluate the model sensitivity to the spatial discretization, we perform the same simulation (scarp evolution starting from a constant slope with conservation of sediments), with dx=0.1 m and dx=0.05 m. The results of the two simulations are identical in time. Moreover, only for a very large cell sizes some differences are visible.

In the second set of simulations we reproduce the infilling of a tidal basin (Fig. 2.6). The initial condition is a tidal flat with a level 2 m lower than LAT (lowest astronomical tide), and the sediment concentration on the seaward boundary cell is set equal to 0.5 g/l . The net inflow of sediments leads to marsh accretion (Fig. 2.6a,b). In both cases (with and without vegetation) sediments start to accumulate at the landward side, maintaining a concave-up shape, with a gradual steepening of the deposit's slope. When the accreting area is close to HAT, the sediments form a terrace and a change in concavity takes place. After this point the whole profile progrades with a rigid translation, without variations in shape. When the vegetation is absent (Fig. 2.6a) the progadation ends when the system finds an equilibrium with the sediment input (after 300 years of simulation the profile does not change anymore). The equilibrium shape is similar to the one achieved imposing the conservation of sediment volume. When the vegetation is present (Fig. 2.6b) the profile does not reach equilibrium, and the system tends to fill the entire tidal basin. The slope between salt marsh and tidal flat is steeper (1:15) than in the case without vegetation (1:50), but the vertical scarp is still absent.

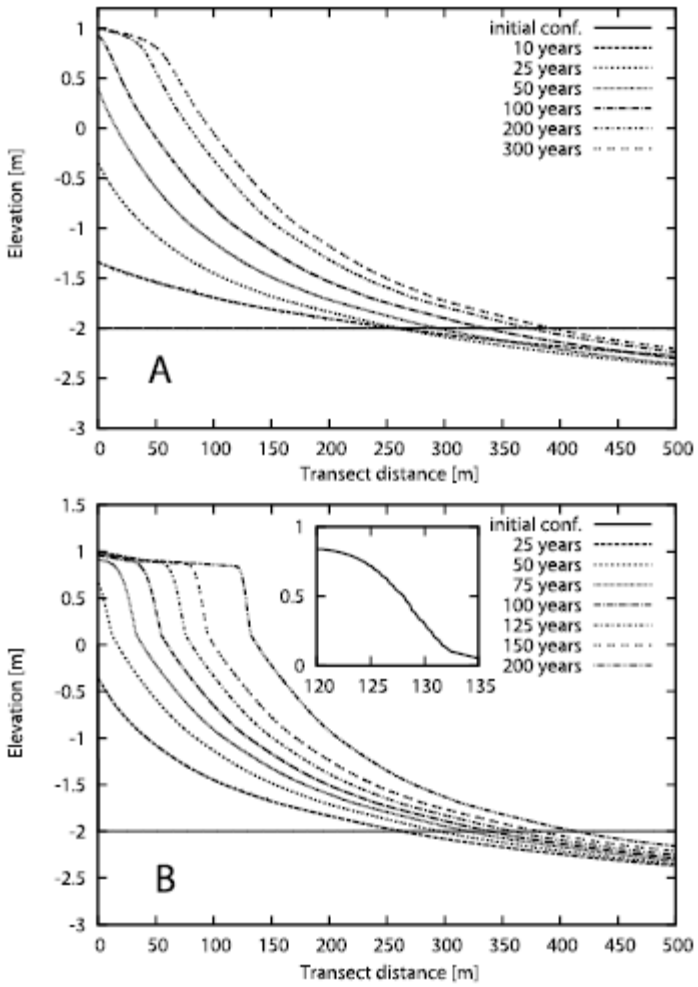

Figure 2.6: Basin infilling. The evolution of the profile starts from a horizontal tidal flat, with a constant sediment concentration (0.5 g/l) at the seaward boundary. a) without vegetation, b) with vegetation. The marsh is defined as the zone where the marsh vegetation can grow, tidal flat as the zone where the marsh vegetation cannot grow.

In the third set of experiments we simulate the erosion of salt marshes in a tidal basin (Fig. 2.7). In this case the initial configuration is set equal to the configuration reached after 150 years of basin infilling with vegetation (see Fig. 2.6b). In order to remove sediment from the basin, the sediment concentration at the seaward boundary cell is set equal to a low value (0.1 g/l), so that a net sediment flux exits the domain. In both

simulations, with and without vegetation, erosion lowers the tidal flat over time by about 0.5 m. When vegetation is absent erosion takes place on the top of the scarp, creating a gentle profile (Fig. 2.7a). During the last stages of the erosion process, the slope of the platform becomes steeper and eventually a vertical scarp forms. At this point the regression of the platform is given by a translation of the scarp. The erosion of the scarp continues until all sediments are removed from the basin. When vegetation is present, the upper part of the marsh is not eroded (Fig 2.7b). The erosion concentrates at the foot of the marsh, and a vertical scarp forms after a short time. Once the scarp is created, the erosion of the marsh is given by a rigid translation of the boundary. The height of the scarp remains constant in time, at 1 m.

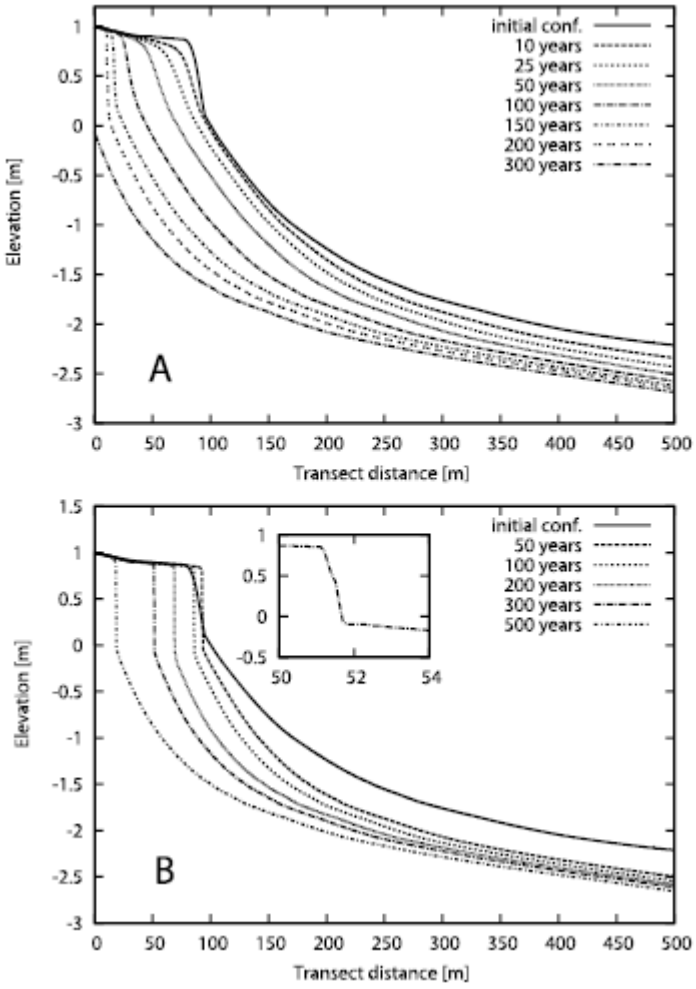

Figure 2.7: Salt marsh deterioration. The evolution of the profile starts from a fully developed salt marsh, imposing a sediment concentration equal to 0.1 g/l at the seaward boundary: a) without vegetation, b) with vegetation.

Figure 2.8 shows the elevation distribution in the basin with vegetation, during infilling (Fig. 2.8a) and during erosion (Fig. 2.8b). In both cases the distribution is bimodal, with one peak corresponding to the tidal flat elevation and one corresponding to the salt marsh elevation (see also Fagherazzi et al. 2006).

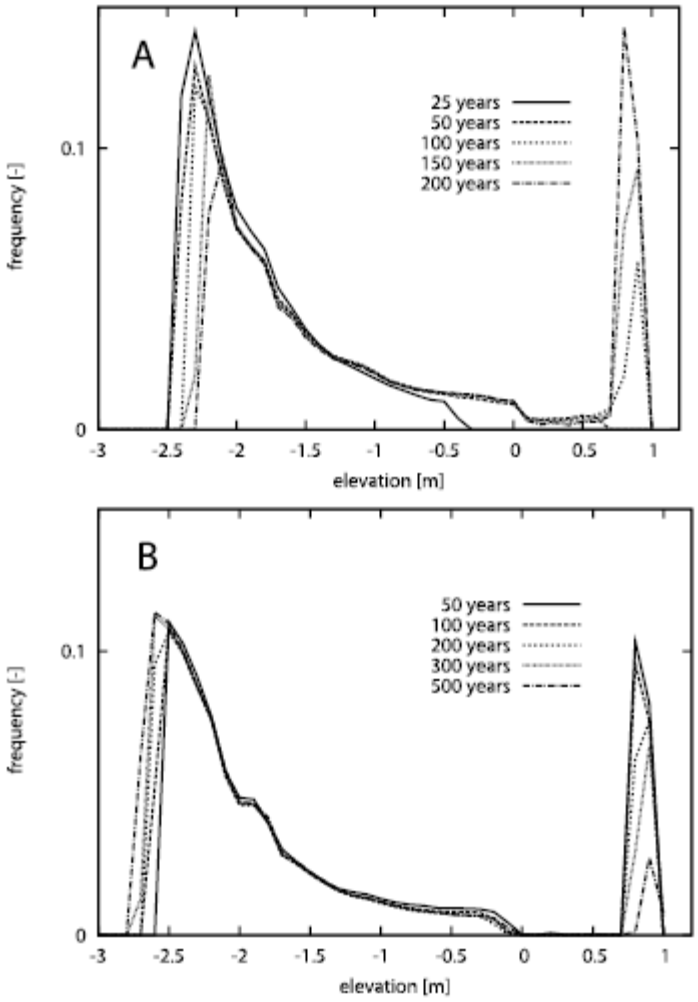

Figure 2.8: Frequency distribution of basin elevation during the simulation (vegetated case). a) Basin infilling, b) Basin erosion.

In the last set of simulations the effect of Relative Sea Level Rise (RSLR) is taken into account. In Figure 2.9 is shown the simulation of the erosion of the marshes with a constant RSLR of 2 mm/yr. As in the simulation with no RSLR, when the vegetation is present a vertical scarp forms, but in this case the regression is faster (about 1.5 times), and the height of the scarp increases in time, reaching a maximum of about 1.5 m (Fig.

2.9b). When the vegetation is absent, no vertical scarp forms, not even at the last stages of the erosion process (Fig. 2.9a).

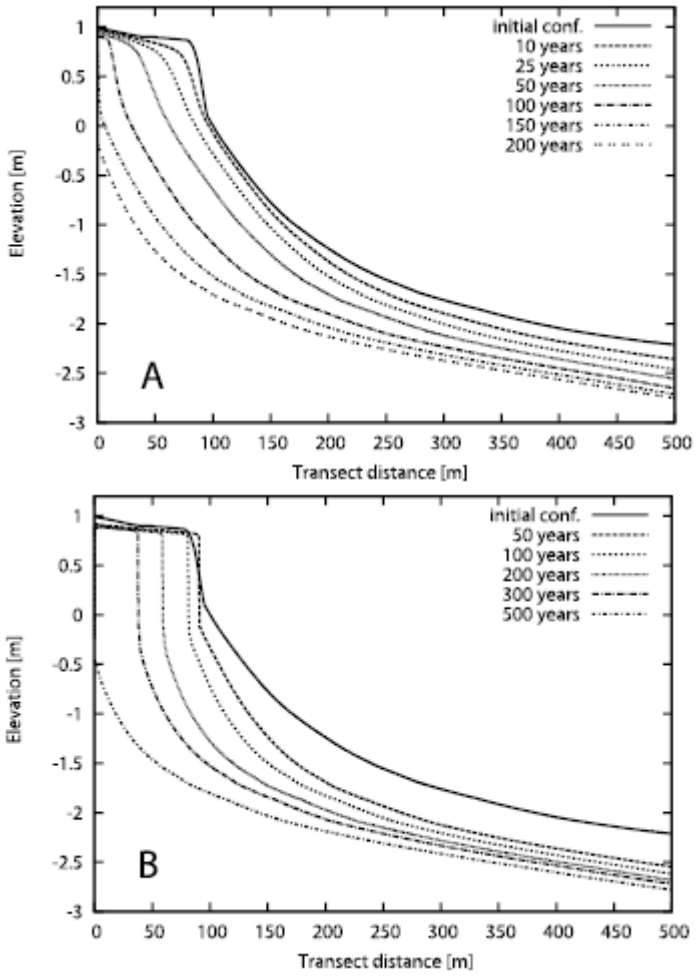

Figure 2.9: Basin erosion with a RSLR rate of 2 mm/yr. a) Without vegetation b) With vegetation.

In Figure 2.10 we simulate the coupled salt marsh - tidal flat evolution under different rates of sea-level rise. Only the simulation with vegetation is reported. When the RSLR is low, 2 mm/yr, the marsh is prograding (Fig. 2.10a). The slope between the marsh and the tidal flat is steeper (1:5) than in the case without RSLR, but without a distinct

vertical scarp. With a RSLR of 10 mm/yr the marsh is close to equilibrium (Fig. 2.10b). The marsh initially progrades and then regrades with a very slow rate (about 0.03 m/yr). With a RSLR of 20 mm/yr the scarp instead regrades (Fig. 2.10c), with a fast rate (about 0.5 m/yr). With a RSLR of 30 mm/yr the scarp initially regrades and then eventually drowns (Fig. 2.10d).

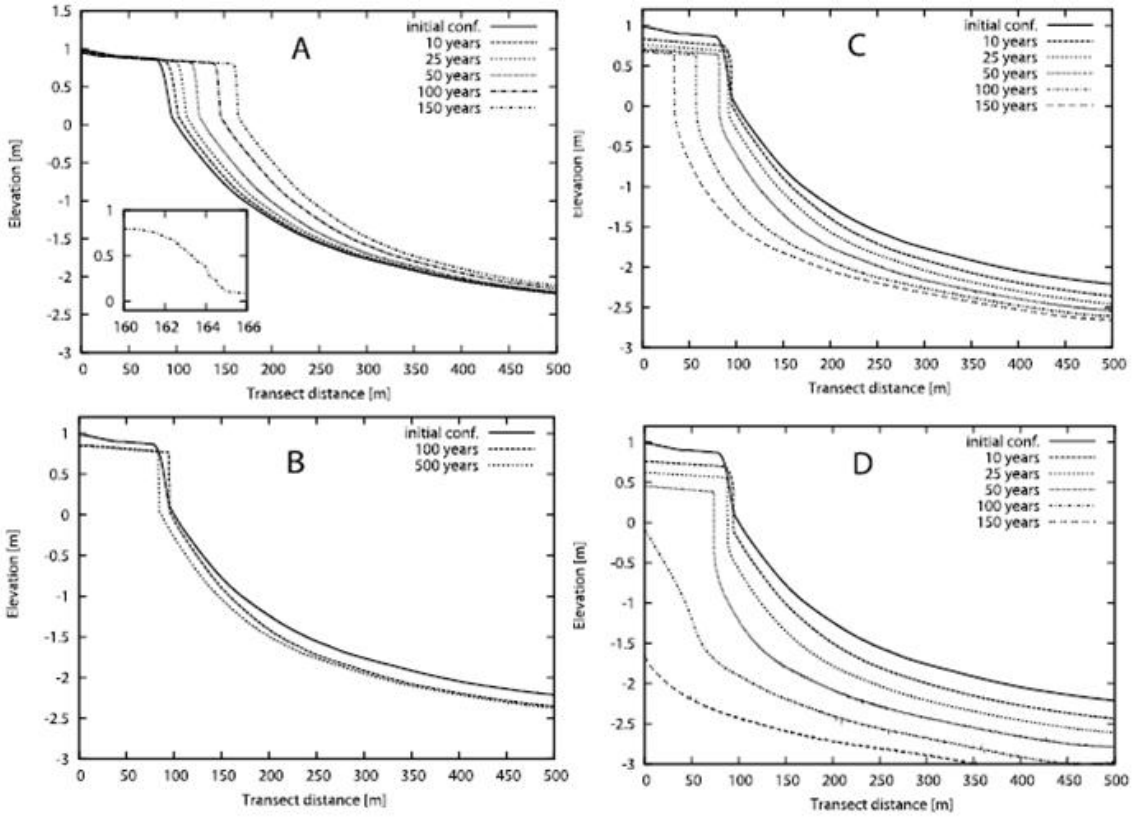

Figure 2.10: Basin evolution with different RSLR rates and vegetation. The sediment concentration at the seaward boundary is equal to 0.5 g/l. a) RSLR=0.2 mm/yr. b) 10 mm/yr. c) 20 mm/yr. d) 30 mm/yr.

Figure 2.11 shows the values of marsh boundary horizontal displacement rate (i.e. progradation or erosion) as a function of RSLR and sediment concentration at the seaward boundary. For simplicity we indicate erosion as negative progradation. For

every combination of RSLR and sediment concentration platform progradation is higher when vegetation is present. Moreover, in the vegetated case, the relation between progradation (p), RSLR and boundary sediment concentration (C) is approximately linear (Fig. 2.11a). The sensitivity of the horizontal displacement rate on RSLR and sediment concentration is different whereas the marsh is prograding (p>0) or eroding (p<0). The following set of equations best fits the data:

$$\begin{array}{ll} p = -7.8 \times RSLR + 275 \times C - 75.5 & p > 0 \\ p = -3.5 \times RSLR + 110 \times C - 26 & p < 0 \end{array}, \text{ (Eq. 2.28)}$$

where p is expressed in cm/yr, RSLR is expressed in mm/yr, C is expressed in g/l. Under progradation conditions the sensitivity of the horizontal displacement to RSLR and sediment concentration is more than double that under erosion condition (see the coefficients multiplying RSLR in Eq. 2.28).

When vegetation is absent, the sensitivity of the marsh horizontal displacement rate with RSLR is higher under progradation than under erosion (Fig. 2.11b). Moreover, the relationship between progradation rate and sediment concentration remains approximately linear.

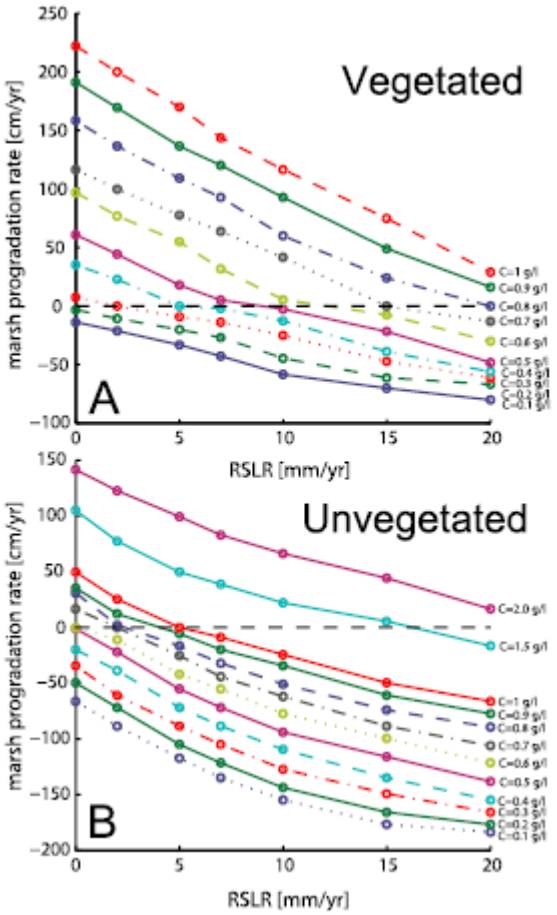

Figure 2.11: Progradation and erosion rates of the marsh boundary as function of RSLR and sediment concentration. Positive values indicate progradation, negative values indicate erosion. A) With vegetation. B) Without vegetation.

2.4 Discussion and Conclusions

The present model is a development of the model proposed by van de Koppel (2005). Our model does not produce the self-organized cycle of scarp erosion episodes which are present in the van de Koppel (2005) model. We suggest three possible reasons for this discrepancy.

First, in the model of van de Koppel (2005) the system is subject to a constant external forcing, i.e. wave erosion is a function of a parameter that is constant over the simulation. In our model the system is instead subject to alternate events of fair weather and wind. This more realistic situation allows the system to escape from conditions of positive erosive feedback, which cause the erosion cascade described in van de Koppel (2005). For example, during a long period without wind, the cliff can find a more stable configuration, depositing sediment at the scarp toe, thus reducing incoming waves and therefore stopping erosion.

Second, in the model of van de Koppel (2005) wave erosion is a function of bottom slope and biomass, which are defined locally and do not depend on the entire landscape morpholology. On the contrary, in our model wave erosion is also a function of tidal flat elevation, which affects wave propagation and therefore the amount of energy reaching the scarp. This global coupling makes the model less dependent on local unstable conditions.

Third, in the van de Koppel (2005) a vertical scarp is inherently unstable, since erosion is proportional to bottom slope. This model component triggers the erosion cascade, since the steeper is the scarp the more unstable it becomes. In our model a vertical scarp is instead stable, thus mimicking the natural conditions of many tidal marsh boundaries.

The model assumes a 1D geometry. This simplification cannot address lateral variations in salt marsh, tidal flat, and scarp morphology. Regarding the salt marsh, the 1D geometry does not address the presence of tidal creeks, which promote marsh drainage and therefore limit the erosion by sheet flow. However, the percentage of marsh area

covered by creeks is generally low, and large stretches of marsh scarp are not affected by them. Therefore we can assume that our transect is far enough from tidal creeks without loss of generality. At the boundary between the marsh and the tidal flat, the 1D geometry prevents the reproduction of complex erosional features, like transversal incisions, gullies, and toe undercutting. These features might induce different rates of boundary erosion, and will be addressed in future research.

The 1D assumption also prevents simulating the formation of drainage channels in tidal flats. Tidal channels concentrate tidal currents, reducing the flow in the remaining tidal flat. The channels promote the local transport of sediments, leading to a global increase in sediment mobility. This effect can be simulated increasing the suspended sediment diffusion in our model (the parameter ζ in Eq. 2.17). However, all these processes do not directly affect the local scarp evolution, which is the key point of this study. Future research will address the role of channels on the coupled evolution of tidal flats and salt marshes.

The spatial discretization introduces an additional source of error since the verticality of the scarp is limited by the finite cell dimension (0.1 m). Therefore the model cannot exactly represent a vertical scarp or a protruding one. However, our simplified discretization is computationally very efficient, and it is sufficient to simulate the scarp evolution in time. We assume that erosion by wave impact only acts in the two cells defining the scarp, and a sensitivity analysis has shown that different cell sizes lead to identical results.

Simulations show that in an intertidal area in which the total amount of sediment is conserved the cross-shore profile evolves until forming a platform above mean sea level and a tidal flat below mean sea level. The profile evolution is faster when the system is far from this equilibrium configuration, such as when the initial bathymetry is horizontal or with constant slope. In the initial stages of the evolution there are zones along the tidal flat profile where erosion, both by shear stress and wave breaking, is concentrated. On the contrary, close to the final equilibrium configuration, erosion rates are almost negligible along the tidal flat. In fact the equilibrium profile of the tidal flat varies gently in space thus preventing wave breaking, but favoring the dissipation of wave energy by bottom friction. Moreover, when the equilibrium configuration is reached, the tidal flat bottom is below the critical shear stress for erosion for most of the time. The concave-up equilibrium profile of the tidal flat resulting from our simulations is in agreement with the results of tidal flat models and field observations (Pritchard et al., 2002; Waeles et al., 2004).

When the intertidal area is encroached by vegetation, and therefore becomes more resistant to wave erosion, a steeper profile develops, with more sediments subtracted from the tidal flat and deposited on the marsh. Is it interesting to note that the tidal flat equilibrium profile is similar with and without vegetation, but just 20cm lower when vegetation is present. This indicates that the equilibrium profile stems from the sediment redistribution between the marsh platform and tidal flat, with depositional processes on the marsh platform affecting the neighboring tidal flats.

With a high sediment supply the tidal flats emerge from the water giving rise to a platform. Once the platform is formed, the boundary between the platform and tidal flat progrades, filling the intertidal area. The boundary is steep when vegetation is present and gentle when vegetation is absent. Moreover, vegetation increases the rate of progradation by capturing and stabilizing sediments on the marsh surface. Platform progradation does not develop a clear vertical scarp, even when vegetation is present. On the contrary, a vertical scarp forms when the marsh is under erosion. Scarp formation is a consequence of the lowering of the tidal flat, induced both by low sediment availability or RSLR, which entails that higher waves are reaching the marsh boundary. Vegetation is not critical for scarp development, since our simulations show that a scarp can form when an unvegetated platform is high in the tidal range (Fig. 2.7a). However, scarp formation is faster when vegetation is present.

The scarp is the location at which most of the wave energy dissipates by breaking. In order to concentrate wave breaking at one location and develop a vertical scarp, two conditions must take place: i) the tidal flat in front of the scarp has to be flat and enough deep to not significantly dissipate the wave energy before the breaking at the vertical scarp; ii) the scarp must be high enough to concentrate the breaking of the waves for a large range of tidal elevations, i.e. also during high tide the wave has to break at the scarp without propagating on the marsh platform.

The top of the marsh scarp is usually subject to high erosion, which in time would replace the scarp with a gentler slope. However, when the marsh is so high that wind waves cannot reach its surface with enough energy, the top of the slope becomes

sheltered from erosion, so that wave energy concentrates at the bottom promoting downcutting and the development of a vertical scarp. Vegetation decreases sediment erodability and thus protects the high part of the marsh from wave erosion. In addition, vegetation promotes sediment trapping, and therefore accretion. These two mechanisms concentrate erosion in the unvegetated area in front of the marsh, leading to the formation of a vertical scarp.

During the evolution of the intertidal profile, both under marsh progradation and erosion, the distribution of elevations is bimodal, with a distinct marsh and tidal flat separated by a boundary. This underlines that only these two states are stable, and that the highest instability are found in the transition between the two.

RSLR promotes marsh erosion, thus increases the regression rate of the scarp. RSLR submerges the marsh surface, thus promoting erosion not only by wave impact but also by bottom shear stresses, which constantly smooth the marsh edge. Our simulations show that even a small value of RSLR (2 mm/yr) prevents the formation of the scarp when vegetation is absent.

For any given sediement supply, different rates of RSLR entail different qualitative trajectories of basin evolution. A low rate of sea-level rise reduces the depth of the tidal flat increasing wave dissipation. Sediment deposition is thus favored and the marsh boundary progrades. A high rate of sea-level rise leads to a deeper tidal flat and therefore higher waves that erode the marsh boundary, leading to boundary retreat. As long as the maximum deposition rate on the marsh is higher than RSLR, the marsh remains emergent. The marsh converges to an equilibrium elevation near the optimum

value for vegetation growth (see Eq. 2.18), which is lower than the elevation it reaches without RSLR. This equilibrium is stable because a decrease in salt marsh elevation will increase vegetation biomass and therefore increase erosion resistance and sediment trapping (Morris, 2006). However, the lowering of the tidal flat increases the height of the waves reaching the marsh edge, which results in an increase of marsh regression by wave impact, thus accelerating erosion.

When the rate of RSLR is higher than the maximum deposition rate, there are no possible stable elevations for the marsh platform. In fact when the elevation drops below the optimum value for vegetation growth, the marsh becomes unstable because a reduction in vegetation cover increases erodability. At this point both wave impact and wave induced bottom shear stresses will erode the marsh, which eventually drowns, morphing into a tidal flat.

The model results are in accordance with the conceptual model proposed by Schwimmer and Pizzuto (2000) based on field observations. The accretion of the marsh, during a period of high sediment supply and low rate of RSLR, occurs by a successive deposition of sediment wedges in front of the marsh boundary. The accreting gentle profile dissipates wave energy, reducing breaking at the salt marsh boundary. Sedimentation on the marsh continues, until HAT is reached. The regression of the marsh is associated with a steepening of the profile, which eventually leads to scarp formation. The results of our model show that both an increase in the rate of RSLR or a decrease in sediment supply could change the marsh evolutive trajectory from

progradation to regression, as indicated by the stratigraphic data of Schwimmer and Pizzuto (2000).

Our results are also in agreement with the conceptual model proposed by Defina et al. (2007). During the infilling of the basin the marsh vertically accretes until it reaches a critical elevation; after which the marsh progrades horizontally. Similarly, during basin erosion, the marsh is initially eroded through the horizontal migration of the scarp, until eventually the entire marsh drowns.

Figure 2.11 summarizes the model results. When vegetation is present marsh progradation drammatically increases at high sediment concentrations and low RSLR. On the contrary, marsh erosion is less sensitive to RSLR and sediment concentration. We explain this phenomenon by considering the different morphologies that the marsh boundary assumes and the different physical processes that take place at the interface. Under progradation the boundary has a gentle slope, more surface is exposed to waves, and therefore an increase in RSLR will affect a greater surface, leading to a large change in erosive and depositional processes. Instead under regression the marsh boundary becomes a vertical scarp, where all erosion is concentrated. An increase in SLR will affect only a confined zone, reducing the global effect on the intertidal profile. Moreover, progradation is produced by deposition of large volumes of sediments, which can occur in a short time frame (a few tidal cycles are enough to deposit all sediments in suspension). Erosion is instead much slower, since wave attack can erode only a few centimeters of scarp in each storm. Whereas the deposition timescale is fast, the erosion timescale is dictated by the mechanical resistance of the marsh scarp and by the

presence of vegetation, thus limiting the response of the system to rapid variations in sea level.

2.5 References

Allen J.R.L., (2000), Morphodynamics of Holocene salt marshes: a review sketch from the Atlantic and Southern North Sea coasts of Europe, Quaternary Science Review, 19, 12, 1155-1231

Blum, L.K., and R.R. Christian, (2004), Belowground production and decomposition along a tidal gradient in a Virginia salt marsh. In The Ecogeomorphology of Tidal Marshes, eds. S. Fagherazzi, M. Marani, and L.K. Blum, 47–74. Washington, DC: American Geophysical Union.

Chapra, S.C., (1996), Surface Water-Quality Modeling. McGraw-Hill, 784 pp.

Cowell, P.J., M.J.F. Stive, A.W. Niedoroda, H.J. DE Vriend, D.J.P. Swift, G.M. Kaminsky, and M. Capobianco, (2003), The coastal-tract (part 1): a conceptual approach to aggregated modeling of low-order coastal change, Journal of Coastal Research, 19, 4, 812-827.

D'Alpaos A., S. Lanzoni, M. Marani, S. Fagherazzi, and A. Rinaldo, (2005), Tidal network ontogeny: Channel initiation and early development, Journal of Geophysical Research, 110, F02001.

D'Alpaos, A., S. Lanzoni, S.M. Mudd, and S. Fagherazzi, (2006), Modeling the influence of hydroperiod and vegetation on the cross-sectional formation of tidal channels Estuarine, Coastal and Shelf Science 69, 3-4, 311-324.

Defina, A., L. Carniello, S. Fagherazzi, and A. D'Alpaos, (2007), Self-organization of shallow basins in tidal flats and salt marshes, Journal of Geophysical Research, 112, F03001.

Fagherazzi, S., and T. Sun, (2003), Numerical simulations of transportational cyclic steps Computers & Geosciences, 29(9), 1071-1201.

Fagherazzi, S., M. Marani, and L.K. Blum, (Editors) (2004), The Ecogeomorphology of Tidal Marshes, American Geophysical Union Coastal and Esturine Studies, Washington DC, Volume 59, 266 pages.

Fagherazzi, S., L. Carniello, L. D'Alpaos, and A. Defina, (2006), Critical bifurcation of shallow microtidal landforms in tidal flats and salt marshes Proceeding of the National Academy of Sciences, 103, 22, 8337-8341.

Fagherazzi, S., C. Palermo, M. C. Rulli, L. Carniello, and A. Defina, (2007), Wind waves in shallow microtidal basins ans the dynamic equilibrium of tidal flats, of Geophysical Research, 112, F02024.

Fredsoe, J., and R. Deigaard, (1992), Mechanics of Coastal Sediement Transport (Advanced Series in Ocean Engineering, Vol. 3) (World Scientific, Singapore), p.369.

Goda, Y., (1970), New Wave pressure Formulae for Composite Breakwaters, Proceedings of the 14th International Coastal Engineering Conference, Vol. 3, pp 1702-1720.

James, W.F., J.W. Barko, and G.B. Malcolm, (2004), Shear stress and sediment resuspension in relation to submersed macrophyte biomass, Hydrobiologia, 515, 181–191.

Kirwan, M.L., and A.B. Murray, (2007), A coupled geomorphic and ecological model of tidal marsh evolution, Proceedings of the National Academy of Sciences of the United States of America, 104, 15, 6118-6122.

Le Hir, P., Y. Monbet, and F. Orvain, (2007), Sediment erodability in sediment transport modelling: Can we account for biota effects?, Continental Shelf Research, 27, 8, 1116-1142.

Mudd, S.M., S. Fagherazzi, J.T. Morris, and D.J. Furbish., (2004), Flow, Sedimentation, and Biomass Production on a Vegetated Salt Marsh in South Carolina: Toward a Predictive Model of Marsh Morphologic and Ecologic Evolution, Coastal and Estuarine Studies.

Möeller, I., (2006), Quantifying saltmarsh vegetation and its effect on wave height dissipation: Results from a UK East coast saltmarsh. Estuarine, Coastal and Shelf Science, 69, 337-351.

Morris, J.T., and B. Haskin, (1990), A 5-yr record of aerial primary production and stand characteristics of Spartina alterniflora, Ecology, 71, 6, 2209-2217.

Morris, J.T., P.V. Sundareshwar, C.T. Nietch, B. Kjerfve, and D.R. Cahoon, (2002) Responses of coastal wetlands to rising sea level, Ecology, 83, 2869-2877.

Morris, J.T., (2006), Competition among marsh macrophytes by means of geomorphological displacement in the intertidal zone. Estuarine, Coastal and Shelf Science, 69, 395-402.

Mudd, S.M., Fagherazzi, S., Morris J.T., and Furbish D.J., (2004), Flow, sedimentation, and biomass production on a vegetated salt marsh in South Carolina: toward a predictive model of marsh morphologic and ecologic evolution, in Fagherazzi, S., M. Marani, and L.K. Blum, (Eds.) The Ecogeomorphology of Salt Marshes, Estuarine and Coastal Studies Series, American Geophysical Union, Washington D.C., pp. 165-187.

Parchure, T.M., and A.J. Metha, (1985), Erosion of soft cohesive sediment deposits, Journal of Hydraulic Engineering- ASCE, 111, 10, 1308-1326.

Parker, G., M.H. Garcia,Y. Fukushima, and W. Yu, (1987), Experiments on turbidity currents aver an erodible bed, Journal of Hydraulic Research, 25, 1, 123-147.

Pizzuto, J.E., and T.S. Meckelnburgts, (1989), Evaluation of a linear bank erosion equation, Water resources research, 25, 5, 1005-1013.

Pritchard, D., A.J. Hogga, and W. Roberts, (2002), Morphological modelling of intertidal mudflats: the role of cross-shore tidal currents, Continenatl Shelf Research, 22, 1887–1895.

Randerson, P.F., (1979), A simulation of salt-marsh development and plant ecology. In: Knights, B., A.J. Phillips (Eds.), Estuarine and Coastal Land Reclamation and Water Storage, Sazon House, Farnborough, pp. 48-67.

Sainflou, M., (1928), Treatise on Vertical Breakwaters, Annals des Ponts et Chaussee, (Translated by W.J. Yardoff, U.S. Army Corps of Engineers.).

Schwimmer, R.A., and J.E. Pizzuto, (2000), A Model for the Evolution of Marsh Shorelines, Journal of Sedimentary Research, 70, 5, 1026-1035.

Schwimmer, R.A., (2001), Rates and Processes of Marsh Shoreline Erosion in Rehoboth Bay, Delaware, U.S.A. Journal of Coastal Rsearch, 17, 3, 672-683.

Seminara, G., Meanders, (2006), Journal of Fluid Mechanics, 554, 271-279.

Soulsby, R.L., (1997), Dynamics of Marine Sands: A Manual for Practical Applications, 248 pp., Thomas Telford, London.

Tanimoto, K., K. Moto, S. Ishizuka, and Y. Goda, (1976), An Investigation on Design Wave Force Formulae of Composite-Type Breakwaters, Proceedings of the 23rd Japanese Conference on Coastal Engineering, pp 11-16 (in Japanese).

Trenhaile, A.S., (2009), Modeling the erosion of cohesive clay coasts, Coastal Engineering, 56, 1, 59-72

van de Koppel, J., D. van der Wal, J.P. Bakker, and P.M.J. Herman, (2005), Self-organization and vegetation collapse in salt marsh ecosystems, American Naturalist, 165, 1, 1-12.

Waeles, B., P. Le Hir, and R. Silva Jacinto, (2004), Modélisation morphodynamique cross-shore d'un esrtan vaseux, Comptes Rendus Geoscience 336, 1025-1033 (in French, with abridged English version).

Chapter 3. Channels - tidal flat sediment exchange: the channel spillover

The contents of this were published in 2012 in the Journal of Geophysical Research – Oceans. This paper was co-authored with S. Fagherazzi (Department of Earth Science, Boston University).

Abstract

We analyze the hydrodynamics and sediment transport on a mudflat in Willapa Bay, Washington State, USA. Velocity profiles and suspended sediment concentrations were simultaneously measured for 46 days in a major flow-through channel, in a dead-end tributary channel, on the channel bank and on the adjacent tidal flat, encompassing periods with and without wind waves. A lateral circulation, perpendicular to the direction of the main channel, is observed to be associated with high sediment discharge directed from the channel to the tidal flat at the beginning of flood. This sediment discharge is able to explain the turbid tidal edge, which is a common feature of many tidal flats. An analytical model describing the lateral circulation and a conceptual model describing the sediment spillover from the channel are proposed. According to the model, the tidal flat sediment dynamics are strongly influenced by the sediment input from the main channel during fair weather, a process that is often overlooked in simplified models of tidal flat morphodynamics.

3.1 Introduction

Intertidal areas are characterized by extensive tidal flats incised by a network of channels. The sedimentary dynamics of these systems is governed by a variety of processes, which takes place at different temporal and spatial scales (de Swart and Zimmerman, 2009). The main processes triggering sediment transport are tides, stratification and density driven circulation, wind waves and wind induced currents, and drainage processes (Eisma, 1997; Le Hir et al., 2000; Friedrichs, 2012).

Tidal asymmetries, generated by the distortion of the tidal wave during its propagation in shallow water, result in a residual sediment transport. Analytical models suggest that high friction promotes flood dominance and hence landward transport, while extensive intertidal storage area, such as tidal flats and salt marshes, promotes ebb dominance and hence seaward transport (Speer and Aubrey, 1985; Friedrichs and Aubrey, 1988). In addition, the phase of the principal tidal constituents can generate tidal asymmetries in the absence of any internal distortion (Hoitink et al., 2003), which, for example, results in ebb-dominated tides along the Pacific coast of the United States (Nidzieko, 2010).

River discharge often induces density driven flow and stratification of the water column. Strain-induced periodic stratification (SIPS; Simpson et. al., 1990) influences the structure of the bottom boundary layer and can generate a landward net transport (Geyer, 1993; Stacey and Ralston, 2005).

Transport of fine sediments, which takes place predominantly in suspension, is largely affected by settling lag (Postma, 1967; Pritchard, 2005). In addition, because of asymmetry in vertical mixing induced by flocculation, larger flocs are transported at different water depths and velocities during ebb and flood (Winterwerp, 2011). Both settling lag and internal tidal asymmetry results in a net landward transport.

Wind surface waves also affect sediment resuspension and hence net sediment transport (Whitehouse and Mitchener, 1998; Roberts et al., 2000; Le Hir et al., 2000).Waves resuspend sediments via bottom stress triggered by wave orbital velocities, and inhibit sediment deposition during high slack water. Wind can also induce steady currents and seiches, which enhance sediment resuspension (Gloor et al, 1994; Talke and Stacey, 2008). As a consequence, sediment fluxes during storm conditions are mainly directed seaward (Dyer et al., 2000; Christiansen et al., 2006).

In addition, other processes have been recently shown to play a significant role: biota, such as macrophytes, microphytobenthos, and macrofauna, affect sediment erodability (Kornman and de Deckere, 1998; de Brouwer et al., 2000; Le Hir et al., 2007), while rainfall on the exposed tidal flat produces a mechanical abrasion that weakens the superficial layer and reduces the stabilizing effect of biofilms (Tolhurst et al., 2006; Tolhurst et al., 2008).

This work will focus on another important process which is often overlooked in simplified tidal flat models (e.g. Roberts et al, 2000; Pritchard, 2005): the sediment exchange between channels and tidal flats. Because of the higher current velocity, tidal

channels are often characterized by higher suspended sediment concentration than tidal flats during fair weather (Allen and Duffy, 1998; Ridderinkof, 2000; Janssen-Stelder, 2000). Therefore channels are a potential source of sediments for the flat, provided that a transport mechanism between them is present. Indeed, lateral circulation, i.e. the water fluxes between large channels and adjacent shoals, has been observed and explained with analytical models (Uncles et al, 1986; Li and O'Donnell, 1997; Li and Valle-Levinson, 1999; Li and O'Donnell, 2005). This circulation is characterized by the divergence of water from the channel during flood and a convergence during ebb. In addition, salinity gradients can establish a lateral baroclinic circulation between channels and shoals, with water moving out of the channel near the bed and converging at the surface (Lacy et al, 2003; Ralston and Stacey, 2005).

A number of authors observed sediment transport from high to low energy environments driven by tidal dispersion. Yang et al. (2003) found that during calm weather, sediment are preferentially resuspended in subtidal channels, and are advected landward by tidal currents. Ridderinkhof et al. (2000) argued that horizontal transport processes can explain some of the observed sediment patterns of the Ems-Dollard Estuary in The Netherlands (see also Dyer et al. 2000), by causing an exchange of sediments between the channels and the mudflat. Black (1998) concluded that sediment advection from deep and energetic regions of the Humber Estuary in the UK can explain the high sediment concentration measured on the mudflat at the beginning of the flood, which is often referred to as turbid tidal edge. These sediment pulses were

also detected in the Gradyb tidal area of the Wadden Sea (Pejrup, 1988) and in the mudflat of the Tavy Estuary in the UK (Uncles and Stephen, 2000).

The turbid tidal edge on a small mudflat in San Francisco Bay was explained by Talke and Stacey (2008) by considering the propagation of a salinity front: sharp horizontal density gradients are capable of trapping sediments and advecting them without significant dispersion (Ralston and Stacey, 2005). Warner et al (2004) measured a similar turbid tidal edge in San Francisco Bay associated with strong barotropic gradients from the channel to the tidal flat. Both the flood pulse and the barotropic gradients were reproduced with the numerical model ROMS (Song and Haidvogel, 1994) without introducing stratification, suggesting that in this case the turbid edge was not associated with frontal processes. The model's results showed that the flood pulses were associated with a net accretion on the tidal flat. However, the authors did not specify whether the turbid tidal edge was produced by local erosion or by advection. Similarly, Christie et al. (1999) measured a net increase of bed elevation just after the sediment flood pulses. These results indicate that the turbid tidal edge is a key process for the accumulation of sediment on tidal flats.

In this paper we investigate the mechanisms producing sediment exchange between channels and tidal flat in Willapa Bay, Washington State, USA. The dataset consists of velocity profiles and suspended sediment concentration simultaneously measured in a main flow-through channel, in a small tributary channel, on a channel bank and on the

adjacent tidal flat. The dataset spans 46 consecutive days of measurements during spring and neap tides, as well as during periods with wind waves were sampled.

Our measurements show a distinct transverse circulation characterized by a high velocity flow spilling from the channel at the beginning of the flood, similar to those measured (Collins et al. 1998; Le Hir et al. 2000; Friedrichs, 2012) and simulated (Warner et al. 2004) in various tidal flat-channels systems. The purpose of this paper is twofold: to introduce a simple analytical model for channel hydrodynamics that explains the observed transverse circulation, and to propose a conceptual model, named herein the channel spillover mechanism, which describes the sediment exchange between channels and tidal flat, thus offering an explanation for the turbid tidal edge.

3.2 Study site

Willapa Bay, Washington State, USA, is a mesotidal embayment with mixed-semidiurnal tides having a mean tidal range of 2.7 m (Hickey and Banas, 2003). The bay is located on the North Pacific coast of the United States and it is protected by a sand barrier peninsula on the seaward side aligned along the N-S direction (Fig. 3.1A). The bay has approximately a rectangular shape, 8x40 km, with a single inlet on the north side. The tide enters the bay through the inlet and propagates in the N-S direction. Four main rivers discharge in the bay: the North and the Willapa Rivers in the upper part, the Naselle River in the middle part, and the Bear River in the lower part of the bay. Of the four major rivers entering the bay, the Willapa and North Rivers account for

70-80 % of the freshwater delivered to the bay (Banas et al., 2004). These two rivers are located very close to the inlet and therefore have only a minor effect on the southern part of the bay. The Naselle River accounts for about 20% of the total freshwater input. The Bear River discharge is estimated to be 17 % of the Naselle River (Nowaki and Ogston, 2011), which translates to about 3 % of the total frashwater input. The Bear River discharges in the Bear River channel, which is one of the major tidal channels within the bay (Fig. 3.1A,B). We will herein refer to the Bear River channel as the BR channel.

The southern part of the bay is characterized by extensive mudflats, incised by channels of a wide range of dimensions (Fig. 3.1B). The mudflat substrate has a high concentration of silt and clay sediments (Peterson et al. 1984). Sediments in the channels and on the flat are compositionally similar and are characterized by flocs ranging from 0.16 to 20 μm (Law et al., 2011). Our study focuses on the upper part of the BR channel and its adjacent mudflat (Fig. 3.1B). The BR channel is oriented along the bay major axis (N-S) and is about 100-200 m wide and 2-3 m deep with respect to MLLW (NOAA nautical chart 18504, 1998). At this location the mudflat is drained by a series of small tributary channels, oriented W-E, spaced approximately 200 m, and connected to the BR channel (Fig. 3.1C). The mouth of these channels is about 1 m deep and 10 m wide; the channels are about 500m long and shoals until reaching the tidal flat elevation. According to the classification of Ashley and Zeff (1988), the BR channel constitutes a flow-through channel, while the tributary channels on the mudflat are dead-end (drainage) channels.

Five Acoustic Doppler Current Profiler (ADCP) were deployed for 46 days (from 2/21 to 4/9 2010) for a total of 90 tidal cycles. Two ADCPs were placed on the tidal flat (TF1, TF2), one at the mouth of a dead-end channel, one inside the BR channel, and one on the tidal flat next to the BR channel (channel bank) (Fig. 3.1C). The ADCPs were deployed directly on the bed surface in the upward looking configuration. Near the bank site the BR channel bifurcates in two branches, which reconnect after 1 km. The east branch is about 60 m wide and 2 m deep with respect to the tidal flat, the west branch is about 80 m wide and 3 m deep. The ADCP in the BR channel was deployed in the east branch (see Fig. 3.1C). Finally, an Optical Backscatter Sensor (OBS) was deployed with the ADCP in the dead-end channel at 20 cm from the channel bottom.

A topographic survey reveals that the mudflat is approximately flat along the N-S direction, at the spatial scale of the tidal flat width (500 m). A bottom slope is present in the W-E direction, but only within the last 250 m close to the landward boundary, varying gradually from 0.1% to 1% (Fig. 3.1E). The mudflat is placed 0.7 m below mean sea level (MSL), and its elevation in the main seaward section is set herein equal to zero in a local coordinate system. The two instrument sites on the tidal flat are placed at the same elevation; the bottom of the dead-end channel is 1m below the tidal flat, the bank site (low tidal flat) is 0.3m below the tidal flat, and the site in the BR channel is 1.4 m below the tidal flat elevation.

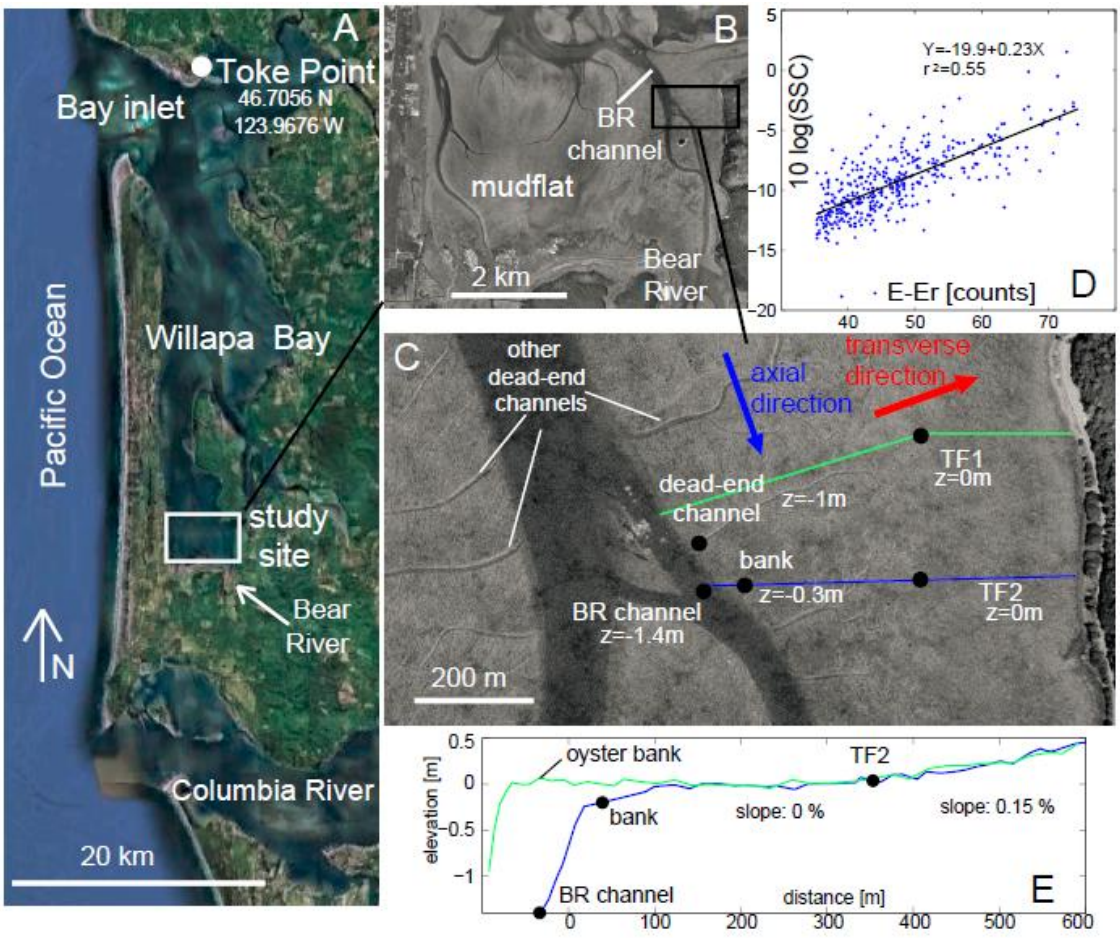

Figure 3.1: A) Location of Willapa Bay, Washington State, USA. Image from Google Map, 2010, with data from USGS, SIO, NOAA, US Navy, NGA, GEBCO. B) Detail of the inner mudflat of Willapa Bay. C) Instrument deployment with position of the five ADCPs. Image from Google Map, 2004, data from DigitalGlobe and USGS. D) Calibration of the ADCP backscatter with the suspended sediment concentration. E) Topographic transect from a local survey. The location of the transects is shown in Figure 3.1C.

3.3 Data collection and analysis

3.3.1 Tidal Currents

Velocity profiles ***u****(z)* were measured with the ADCPs at 2 Hz every 30 minutes, averaging over 60 s, with a vertical cell size of 10 cm and a blanking distance of 10 cm. Water depth (*d*) was calculated using the pressure measured by the ADCPs' piezometers and by assuming a constant water density ρ equal to 1025 kg/m^3. The pressure was corrected with the atmospheric pressure measured at the NOAA station at Toke Point (station 9440910). Water level was obtained by adding the bed elevation (measured during the survey) to the water depth.

Water discharge per unit of width (simply referred as discharge) was calculated by integrating the velocity profiles over the vertical: $\boldsymbol{q} = \int \boldsymbol{u}(z)dz$. Depth averaged speed **U** was calculated by dividing discharge per unit of width by the water depth: **U**=**q**/d.

Current induced bed shear stress was calculated from the depth averaged speed as:

$$\tau_{curr} = \rho C_D \left|\boldsymbol{U}\right|^2, \text{ (Eq. 3.1)}$$

where C_D is the drag coefficient. In order to use the depth averaged velocity rather than a velocity at a fixed water depth, the drag coefficient is chosen variable with water depth and it is computed with the Manning's formula:

$$C_D = \frac{gn^2}{d^{1/3}}. \text{ (Eq. 3.2)}$$

where g is the gravitational acceleration. The choice of the Manning's coefficient n will be discussed in the results section.

3.3.2 Waves

At every location, a wave burst of 512 points was hourly sampled at 2 Hz. The surface elevation energy spectrum S_η was reconstructed from each wave burst using the standard linear wave theory (Tucker and Pitt, 2011). The multiplying factor to account for the reduction of pressure with depth was limited to 10, to avoid injecting noise into the reconstruction of the surface spectrum (Gibbons et al., 1983). For frequency corresponding to a multiplying factor greater than 10 we assumed that the energy spectrum is proportional to f^{-4}, characteristic function of the tail spectrum in shallow water (Bouws et al., 1985).

The significant wave orbital velocity at the bed U_{bs} was calculated from the surface elevation energy spectrum using the linear wave theory as follows (Wiberg and Sherwood, 2008):

$$U_{bs} = 2\left(\int \frac{\omega^2}{\sinh^2(kd)} S_\eta df \right)^{1/2}, \text{(Eq. 3.3)}$$

where ω is the angular frequency and k is the wave number. The wave induced bed shear stress, τ_{wave}, was computed as:

$$\tau_{wave} = \frac{1}{2} \rho f_w U_{bs}^2, \text{(Eq. 3.4)}$$

where f_w is a friction factor set equal to 0.015 (Green and Coco, 2007).

3.3.3 Suspended sediment concentration

Suspended sediment concentration (SSC) was estimated using the backscatter signal of the ADCP and the turbidity value measured by the OBS when present. The OBS turbidity signal was calibrated against SSC measured in a laboratory tank, using sediments collected on the tidal flat. The linear regression between the OBS signal and the measured SSC had a correlation coefficient $r^2 = 0.97$. The OBS was present only at the dead-end channel site.

At every location, suspended sediment concentration at the bottom of the water column (SSC_b) was estimated using the first bin of the ADCP's backscatter signal (Gartner, 2004; Hoitink and Hoekstr, 2005). The sonar equation can be written as (Deines, 1999):

$$10\log_{10}(SSC) = a + \log_{10}(\Psi R^2) + 2A \cdot R + K_c(E - E_r), \text{ (Eq. 3.5)}$$

where R is the distance along the beam (in m), A is the sum of the water absorption coefficient and the sound attenuation due to sediments (in db/m), E is the echo strength (in counts), E_r is the received signal strength (the echo baseline when no signal is present), K_c is the received signal strength indicator scale factor, and a is a constant parameter. Ψ is a factor that describes the departure from spherical spreading of the backscatter signal, calculated from the formula in Downing et al. (1995) as:

$$\Psi = \left[1 + 1.35R / R_{cr} + (2.5R / R_{cr})^{3.2}\right] / \left[1.35R / R_{cr} + (2.5R / R_{cr})^{3.2}\right], \text{ (Eq. 3.6)}$$

with R_{cr} defining the transition between far and near field, calculated as $R_{cr} = \pi a_t^2 / \lambda$, where a_t is the transducer radius (1 cm) and λ the acoustic wavelength.

For each ADCP, E_r was set equal to the recorded minimum value of the echo strength. The value of a and K_c (Eq. 3.5) were calibrated using the SSC computed with the OBS signal at the dead-end channel site (Fig. 3.1D). For the sites where the OBS were not present (tidal flat, BR channel and bank), the same values of K_c and a were used.

The SSC vertical distribution SSC(z) was computed assuming a Rouse profile:

$$SSC(z) = SSC(z_r)\left[\frac{d-z}{z}\frac{z_r}{d-z_r}\right]^{Ro}, \text{(Eq. 3.7)}$$

where z_r is the reference elevation, equal to the height of the first ADCP bin (0.2 m); *Ro* is the Rouse number, defined as w_s/Ku_*; where w_s is the settling velocity; u_* is the friction velocity and K is the von Karman's constant (0.4). The friction velocity was calculated from the total mean bed shears stress, computed with the nonlinear combination of τ_{wave} and τ_{curr} (Soulsby, 1997): $u_* = \sqrt{\tau_{tot,mean} / \rho}$. The settling velocity was estimated from the exponential decrease in SSC after the flood peak currents at all sites. Given the restricted range of SSC (0-0.8 kg/m^3), we found that a constant settling velocity is appropriate (mean equal to 0.34 mm/s, with a standard deviation of 0.18 mm/s). The term SSC will herein refer to the depth integrated SSC. Finally, suspended sediment discharge per unit of width was calculated by integrating over the vertical the product of the velocity profiles and the SSC profile.

3.3.4 Error analysis

The nominal accuracy for the ADCP is ±0.5 cm/s plus 1% of the measured value. The accuracy of the pressure transducer (and hence water depth) is 2.5 cm. The error of the water discharge calculation depends on both velocity and water depth, and is on the order of a few percent. The nominal accuracy of the OBS is 0.5 g/m^3. The high correlation of the OBS calibration curve obtained in the lab ($r^2 = 0.97$) suggests a high accuracy of the SSC measured in the field. SSC computed with the acoustic backscatter of the ADCPs presents instead a very large error. The low correlation ($r^2= 0.55$) between the SSC measured with the OBS and the acoustic backscatter at the dead-end channel can be explained by three factors. First, even if the average over the three acoustic beams of the instrument is performed, the backscatter signal is measured as an integer number of counts, which spans a limited range (around 50 units). Second, the variability in sediment composition, especially the amount of sand, could significantly change the calibration curve of the acoustic backscatter. However, field surveys showed that the sediment composition is uniform in the studied mudflat and contains a very small amount of sand (Law et al., 2011; Hsu and Ogston, 2011). Finally, the sonar equations introduce further approximations. Adding all these uncertainties, we roughly estimate that the accuracy of the SSC measurements obtained with the backscatter is on the order of 50%. On the other hand, the very recursive SSC patterns observed among different tidal cycles indicates that the precision of the measurements with the backscatter signal is on the order of 10%, in agreement with the precision estimated by Gartner (2004). Several successful applications (Gartner, 2004; Hoitink and Hokstra,

2005; Fagherazzi and Priestas 2010; Sommerfield and Wong, 2011; Hsu and Ogston, 2011) suggest that the acoustic backscatter can be used to quantify SSC with enough accuracy to detect sediment transport processes.

3.3.5 A simple model for barotropic lateral circulation

We consider a rectangular geometry, with the x axis along the longitudinal direction of the main channel and the y axis lying along the channel cross section. The cross section bed elevation, described by the function $z_g = z_g(y)$, varies laterally but it is constant along the x axis.

The depth-averaged, shallow water momentum and continuity equations (Li and O'Donnell, 1997) read:

$$\frac{\partial U_x}{\partial t} + U_x \frac{\partial U_x}{\partial x} + U_y \frac{\partial U_x}{\partial y} = -g \frac{\partial \xi}{\partial x} + \frac{n^2 g U_x |\boldsymbol{U}|}{d^{4/3}}, \text{ (Eq. 3.8)}$$

$$\frac{\partial U_y}{\partial t} + U_x \frac{\partial U_y}{\partial x} + U_y \frac{\partial U_y}{\partial y} = -g \frac{\partial \xi}{\partial y} + \frac{n^2 g U_y |\boldsymbol{U}|}{d^{4/3}}, \text{ (Eq. 3.9)}$$

$$\frac{\partial \xi}{\partial t} + \frac{\partial (U_x d)}{\partial x} + \frac{\partial (U_y d)}{\partial y} = 0, \text{ (Eq. 3.10)}$$

where the subscripts denote the components along *x* and *y* directions, ξ is the water level, and *d* is the water depth, equal to $\xi - z_g$. The Coriolis term is neglected and the friction term is expressed with the Manning formula, as in Eq. 3.2.

Similarly to Li and Valle-Levinsion (1999) we assume that the water level is uniform along the cross section (y axis). The validity of the assumption is supported by a scale analysis of the terms in Eq. 3.9. We introduce a scale D for water depth, a scale ω_T for the tidal angular frequency, and a scale for the across tidal flat length, L_y, and for the along tidal flat length, L_x. Following the non-dimensional analysis presented in Fagherazzi et al. (2003), we can write:

$$d = Dd^*, \xi = D\xi^*, t = \frac{t^*}{\omega_T}, x = x^* L_x, y = y^* L_y, U_x = U_x{}^* L_x \omega_T, U_y = U_y{}^* L_y \omega_T \text{, (Eq. 3.11)}$$

where the variables with a star are non-dimensional. The equations 10-12 thus become:

$$\gamma\left(\frac{\partial U_x{}^*}{\partial t^*} + U_x{}^* \frac{\partial U_x{}^*}{\partial x^*} + U_y{}^* \frac{\partial U_x{}^*}{\partial y^*}\right) = -\frac{\partial \xi^*}{\partial x^*} + \Lambda \frac{U_x{}^* \left|\boldsymbol{U}^*\right|}{(d^*)^{4/3}} \text{, (Eq. 3.12)}$$

$$\varepsilon^2\gamma\left(\frac{\partial U_y{}^*}{\partial t^*} + U_x{}^* \frac{\partial U_y{}^*}{\partial x^*} + U_y{}^* \frac{\partial U_y{}^*}{\partial y^*}\right) = -\frac{\partial \xi^*}{\partial y^*} + \varepsilon^2\Lambda \frac{U_y{}^* \left|\boldsymbol{U}^*\right|}{(d^*)^{4/3}} \text{, (Eq. 3.13)}$$

$$\frac{\partial \xi^*}{\partial t^*} + \frac{\partial (U_x{}^* d^*)}{\partial x^*} + \frac{\partial (U_y{}^* d^*)}{\partial y^*} = 0 \text{, (Eq. 3.14)}$$

with the introduction of three non-dimensional parameters:

$$\varepsilon = \frac{L_y}{L_x}, \gamma = \frac{\omega_T^2 L_x^2}{gD}, \Lambda = \frac{n^2 L_x^3 \omega_T^2}{D^{7/3}} \text{, (Eq. 3.15)}$$

The representative parameters are L_y ~ 500 m (width of the tidal flat at the measurement site), L_x ~ 5000 m (length of the tidal flat and main tidal channels in the

Southern part of Willapa Bay, $\omega_T = 1.4\ 10^{-4}$ (semidiurnal tide) and n = 0.016 s $m^{-1/3}$ (see section 4.3). Water depth discriminates when the parameters γ and Λ are small. For a water depth of 0.2 m, corresponding to the minimum depth for the ADCP velocity measurements, γ is 0.25 and Λ is 26.

The parameter ε^2 is small (~ 0.01) and therefore we can neglect the terms in Eq. 3.13 multiplied by ε^2, as long as the parameters γ and Λ are less than $O(10^2)$. We can also neglect the term in γ in Eq. 12, so that Eqs. 3.12-3.13 become:

$$\frac{\partial \xi^*}{\partial x^*} = \Lambda \frac{U_x^* \left| \boldsymbol{U}^* \right|}{(d^*)^{4/3}}, \text{ (Eq. 3.16)}$$

$$\frac{\partial \xi^*}{\partial y^*} = 0, \text{ (Eq. 3.17)}$$

Eq. 3.16 states that the advection and the local acceleration terms can be neglected in the momentum equation in the *x* direction (see also Friedrichs and Madsen, 1992). Eq. 3.17 states that, at a first approximation, the water surface is flat in the *y* direction, and therefore $\xi = \xi(x,t)$. For water depths smaller than 0.2 m the friction term becomes gradually important and the assumption of constant water level along *y* is no longer valid.

Introducing the discharge per unit width $q_x = U_x d$ and $q_y = U_y d$ and recasting Eqs. 14, 16 and 17 in terms of dimensional variables (Eq. 3.11), we obtain:

$$q_x = \frac{1}{n} d^{5/3} \left| \frac{\partial \xi}{\partial x} \right|^{1/2} sign\left(\frac{\partial \xi}{\partial x} \right), \text{ (Eq. 3.18)}$$

$$\frac{\partial \xi}{\partial t} + \frac{\partial q_x}{\partial x} + \frac{\partial q_y}{\partial y} = 0. \text{ (Eq. 3.19)}$$

We assume that the Manning coefficient *n* is a function of *y* but not of *x*, i.e. that the bottom friction can vary only between channel and tidal flat. For simplicity we drop the absolute value and the sign operator in Eq. 3.18. Taking the derivative of Eq. 3.18 over the *x*-direction we obtain:

$$\frac{\partial q_x}{\partial x} = \frac{1}{n}\left(\frac{1}{2} d^{5/3} \left(\frac{\partial \xi}{\partial x} \right)^{-1/2} \frac{\partial^2 \xi}{\partial x^2} + \frac{5}{3} \left(\frac{\partial \xi}{\partial x} \right)^{3/2} d^{2/3} \right), \text{ (Eq. 3.20)}$$

so that the system 19-20 can be rewritten at every location *x* as:

$$\frac{\partial q_x(y,t)}{\partial x} = \frac{1}{n(y)} \left(\alpha(x) \left[d(y,t) \right]^{5/3} \beta(x) \left[d(y,t) \right]^{2/3} \right), \text{ (Eq. 3.21)}$$

$$\frac{\partial q_y(y,t)}{\partial y} = -\frac{\partial \xi(x,t)}{\partial t} - \frac{1}{n(y)} \left(\alpha(x) \left[d(y,t) \right]^{5/3} \beta(x) \left[d(y,t) \right]^{2/3} \right), \text{ (Eq. 3.22)}$$

where α and β are coefficients that depend on the longitudinal barotropic gradient, which is function of *x* but not of *y*.

Eq. 3.21-3.22 are our simplified model of lateral circulation on a small tidal flat flanking a long channel. Note that if α and β are known, the flow velocity can be computed along the width *y* of the tidal flat, since all the other terms in Eq. 3.21-3.22

are independent of *x*. The model is therefore a useful tool for studying the lateral circulation in a channel-flat system without solving the tidal propagation along the channel. According to Eq. 3.21 the highest divergence in the discharge along the *x* direction takes place in the portion of the cross section with the greatest water depth and the lowest value of *n*, i.e. in the channel. The lateral circulation stems from the difference in discharge divergence between channel and tidal flat in the along channel direction, combined with the constraint of a constant water level. Basically, the tidal channel fills much faster than the tidal flat so that some water must move from the channel to the flat to maintain the water level constant along the transverse direction.

The two coefficients α and β can be evaluated exactly by computing the propagation of the tidal wave along the longitudinal direction and obtaining the corresponding barotropic gradients (e.g. Friedrichs and Madsen, 1992). However, these coefficients can be estimated by introducing an additional equation. Integrating the continuity equation along the y-direction, and imposing a zero lateral velocity at the boundaries of the cross section, we derive:

$$\frac{\partial \xi}{\partial t} L + \int_0^L \frac{\partial q_x}{\partial x} dy = 0 \text{, (Eq. 3.23)}$$

where *L* is the width of the cross section. Eq. 3.23 gives an integral constraint that can be used to estimate the unknown parameters α and β in Eq. 3.21-3.22. For simplicity, we will consider the two extreme cases: $\alpha \gg \beta$ and $\alpha \ll \beta$. Any other relationship between α and β would give a solution that is bounded by the solutions of these two

end members. The choice between the two extreme cases does not change the qualitative result of Eq. 3.21 (greater longitudinal discharge divergence for greater water depths), but affects only the exponent of the power law relationship in Eq. 3.21 and 3.22 (5/3 for $\alpha \gg \beta$ and 2/3 for $\alpha \ll \beta$). Once Eq. 3.21-3.22 are solved, the lateral discharge is computed by integrating the divergence of transverse lateral discharge, and the transverse velocity is calculated dividing the transverse discharge by the water depth.

According to this simple formulation, the lateral circulation depends on the water level displacement, the cross section geometry and the friction coefficient. Because of the integral constraint in Eq. 3.23, the role of Eq. 3.21 is only to redistribute the total longitudinal discharge divergence within the cross section. As a consequence, the lateral circulation depends on the ratio between the friction coefficient in the channel and on the tidal flat, but not on its absolute value.

3.4 Hydrodynamic results

3.4.1 General water circulation

At high tide the entire tidal flat is submerged below 2-3 m of water, while it emerges at low water (Fig 2A). The site in the BR channel is always submerged, even during the lowest tide (-1 m below tidal flat level), while the site at the mouth of the dead-end channel is exposed at very low water levels. The depth averaged velocity **U** is projected along the BR channel (160° N) and perpendicular to the channel (70° N), direction that

coincides with the dead-end channel axis (Fig. 3.1C). We will refer to the former as axial velocity and to the latter as transverse velocity. The velocity is considered positive during flood, i.e. when the two components are directed toward 160° N and toward 70° N.

At all sites the flow pattern is variable within a tidal cycle, but similar between different tidal cycles. The velocity magnitude is greater during spring tides than during neap tides, but the qualitative pattern remains the same. We will therefore describe only a characteristic tidal cycle, considering separately the axial velocity and the transverse velocity.

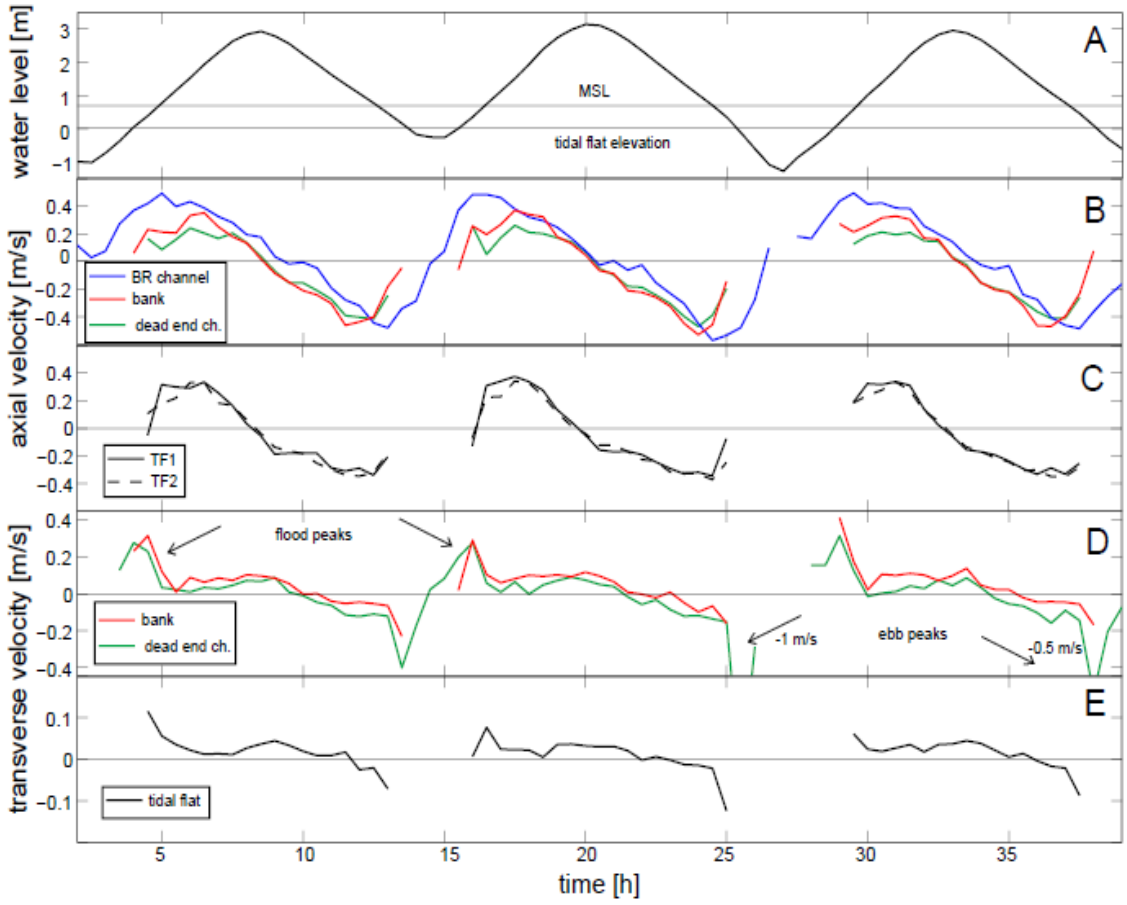

Figure 3.2: Example of the measured physical quantities from 3/3 to 3/6 2010. A) Water level. B) Axial velocity in the BR channel, bank and dead-end channel (only the portion above the tidal flat elevation. C) Axial velocity on the tidal flat sites TF1 and TF2. D) Transverse velocity on the bank and dead-end channel. E) Transverse velocity on the tidal flat (average of T1 and T2).

3.4.1.1. Axial velocity

In the BR channel, on the bank, and on the tidal flat the flow is primarily along the axial direction for most of the tidal cycle. Axial velocities at the two tidal flat sites (TF1, TF2) are very similar, both varying between -0.3 and 0.3 m/s (Fig. 3.2C). For simplicity, we will refer to the velocity on the tidal flat as the average velocity between the two locations. On the tidal flat the phase lag between water level and axial velocity

fluctuation, calculated as the time lag that maximizes the correlation between the two curves, is -90°.The tide is oscillating as a standing wave, with the velocity peaking when the water level is around mean sea level.

In the BR channel the axial velocity is higher than on the tidal flat (maximum velocity around 0.5 m/s); the phase lag between water level and velocities is -78°, representative of a partially progressive wave (Fig. 3.2B). The peak flood velocity in the BR channel is reached 1.5 hours earlier than on the tidal flat, while the peak ebb velocity is reached 1 hour later than on the tidal flat. Therefore the peak velocity in the BR channel always occurs at a lower water level than on the tidal flat.

On the bank site the axial velocity is similar to that on the tidal flat, with the peak velocity reached at the same tidal stage (Fig. 3.2B). However, while the flood peak velocities are almost identical between the two sites, the peak ebb velocity on the bank is 30% higher than on the tidal flat. The axial velocity at the dead-end channel, computed by averaging only the portion of the velocity profile above the tidal flat elevation, is similar to that at the bank (Fig. 3.2B).

3.4.1.2 Transverse velocity

In general, a positive transverse flow (directed toward the tidal flat) is detected during flood, while a negative flow (from the tidal flat to the BR channel) is detected during ebb.

The transverse velocity on the bank shows a clear peak at the beginning of the flood (up to 0.4 m/s), when the water inundates the tidal flat (Fig. 3.2D, Fig. 3.3A). After the

peak, the velocity slows down to around 0.1 m/s. The inward velocity lasts until 2 hours after high slack water; then the transverse flow reverses and a steady velocity around 0.1 m/s directed toward the channel takes place. Finally, when the ebbing flow has almost drained the tidal flat, the transverse velocity peaks again to 0.2-0.3 m/s.

The transverse velocity in the dead-end channel mimics the one on the bank, with a peak at the beginning of the tidal flat inundation (Fig. 3.2D, 3B). Flood velocities are slightly weaker than on the bank, while the opposite holds for ebb velocities. In addition, the dead-end channel shows a very strong transverse ebb velocity when the water levels drops below the tidal flat elevation (up to 1 m/s, depending on tidal amplitude, Fig. 3.3B). This ebb peak was measured by Mariotti and Fagherazzi (2010) and explained as the drainage of the mudflat through lateral runnels.

On the tidal flat a similar pattern is also detected: the velocity is directed toward the tidal flat during flood and toward the BR channel during ebb (Fig. 3.2E). In this case the magnitude of the transverse flow is about half that on the bank, and the peaks are less evident.

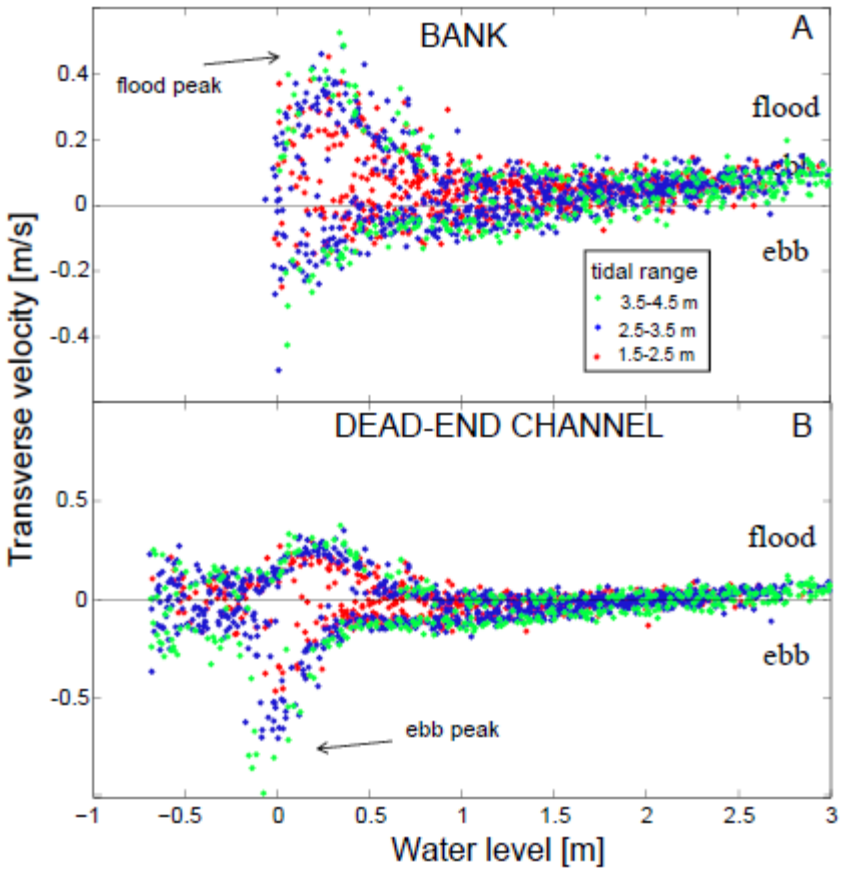

Figure 3.3: Stage versus transverse velocity relationship at A) bank site, B) dead-end channel.

3.4.2 Model results

The lateral circulation model is applied to the study case, considering the cross section geometry in Figure 3.4A by imposing the water level measured in the BR channel. We consider a case with constant value of Manning coefficient in both channel and tidal flat, and a case in which the coefficient on the tidal flat is 1.41the value in the channel. The two cases yield almost identical results (Fig. 3.4C,D), indicating that the variation in water depth between the channel and the tidal flat is more important than a possible variation in bottom frictions.

The model reproduces the peak velocity at the beginning of the flood. The peak velocities are greater at the bank (around 0.3 m/s, Fig. 3.4C) than on the tidal flat (around 0.1 m/s, Fig. 3.4D), in accordance with the measured values. The model anticipates the timing of these peak velocities at both locations. This deviation from the measured data is probably caused by neglecting the lateral barotropic gradient, which tends to delay the propagation of the water from the BR channel.

For both the bank and the tidal flat sites, the same qualitative pattern is obtained assuming $\alpha \gg \beta$ and $\alpha \ll \beta$. In the former case the magnitude of the velocity is greater than in the latter case, because the asymmetry in axial discharge divergence between tidal flat and channel is higher. After the flood peak, the velocity decreases, remains low (<0.1 m/s) and finally grows and peaks again toward the end of the ebb (reaching a value around 0.2 m/s at the bank and 0.1 m/s on the tidal flat). The model also shows that the lateral discharge is always greater at the bank than on the tidal flat (Fig. 3.4E,F).

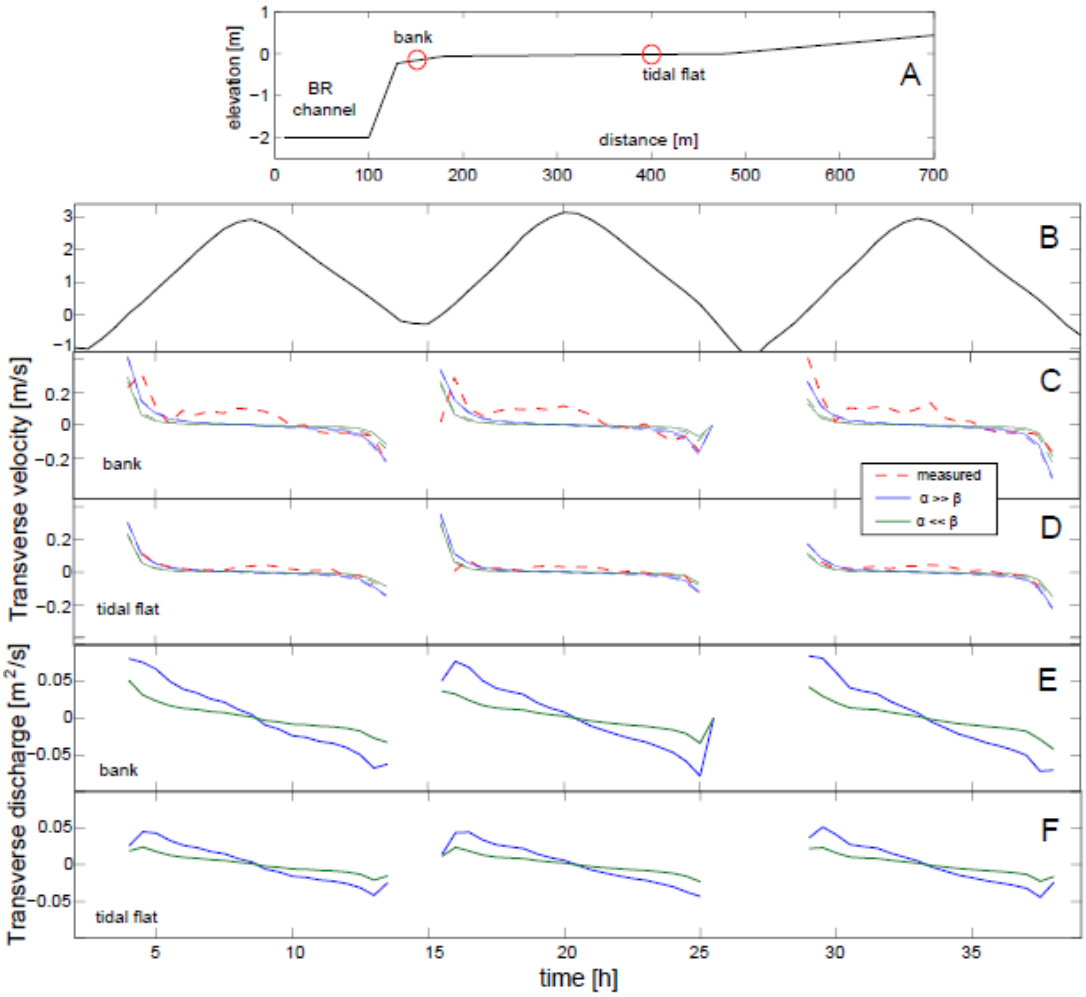

Figure 3.4: Results from the hydrodynamic model for the lateral circulation simulating the period from 3/3 to 3/6 2010. A) Cross section. B) Water level. C,D) Transverse velocity on the bank and on the tidal flat: measured values (red dashed line) and predicted values imposing $\alpha \gg \beta$ and $\alpha \ll \beta$. The continuous line is the case with uniform n (manning coefficient), the dashed line is the case with $n_{tidal\ flat} = 1.41\ n_{channel}$ (the two lines are almost overlapping). E,F) Transverse discharge on the bank and on the tidal flat predicted with the model, imposing $\alpha \gg \beta$ and $\alpha \ll \beta$.

The model does not capture the transverse velocity during the last stage of the flood. A possible explanation is that, at higher water levels, the flow is no more affected by the BR channel, but instead is controlled by the large scale circulation driven by the

complex basin geometry. The model suggests that the observed lateral fluxes at the beginning of the tidal flat inundation and at the end of the tidal flat drainage are generated by the difference in discharge divergence between the main channel and the tidal flat and by the constraint of continuity (Eq. 3.21-3.22).

In the rest of the paper we will investigate how sediment dynamics are affected by this lateral circulation. However, we will first analyze the structure of the vertical velocity profile in order to assess the role of stratification.

3.4.3 Stratification and drag coefficient

In this section we evaluate the possible effects of stratification and estimate the friction coefficient in Eq. 3.2. Stratification, and in particular strain-induced periodic stratification (SIPS; Simpson et. al., 1990), is able to influence the structure of the bottom boundary layer and hence turbulence mixing and bed shear stress (Stacey and Ralston, 2005). Therefore the analysis of stratification is important in order to understand the patterns of current induced bed shear stress during ebb and flood.

No direct measurements of salinity were performed during the survey. However, the freshwater input of Bear River can be used to qualitatively estimate the importance of stratification. The measuring period was characterized by low river discharge: the mean discharge from Bear River (estimated as 20% of the Naselle River discharge, USGS station 12010000) was 2.6 m^3/s, with a peak of 5.2 m^3/s (Fig. 3.5C). As a reference, the tidal prism in the southern Willapa Bay tidal flat is about 45 10^6 m^3, which gives a mean tidal discharge of 2 10^3 m^3/s. The low river discharge suggests that stratification was

low during the sampling period. In fact, during the same period, Nowaki and Ogston (2011) measured vertical variation of salinity on the order of few PSU in a nearby tributary channel.

Velocity profiles were analyzed to infer the structure of the bottom boundary layer and to detect the presence of stratified flows. In order to reduce the scatter on the velocity measurements, the profiles were ensemble averaged based on water level, tidal phase (ebb or flood) and tidal range (Fig. 3.6). First, a tidal range was assigned to each velocity profile, calculated as the difference between the closest high and low slack water levels. Distinction was made between flood profiles (mean velocity <0) and ebb profiles (mean velocity >0). Finally, within each class of tidal range (1.5-2.5m; 2.5-3.5m; 3.5-4.5 m), all the velocity profiles corresponding to a water level between -0.25 and 0.25 m were averaged together to produce one profile; this was repeated in intervals of 0.5 m from -0.25 m to 2.75m.

A qualitative observation of the velocity profiles (Fig. 3.6) indicates that the bottom boundary layer extends over most of the water column, at least for water depths smaller than 2.5 m, which are associated to the highest velocities. The profiles do not show apparent differences between ebb and flood, for each class of tidal range and water level. In particular, no mid-depth maxima in the velocity profiles, characteristic of stratification and baroclinic circulation are evident (Ralston and Stacey 2005, Lacy et al. 2003).

Bed roughness was estimated fitting a log-linear profile distribution to all the profiles with a mean velocity greater than 0.2 m/s (Soulsby and Dyer, 1981). The estimated bed roughness shows a large variability, ranging from 0.3 to 46.8 mm, with a mean of 5 mm. No clear differences between ebb and flood, between accelerating and decelerating flow, and between BR channel and tidal flat were detected.

An independent estimation of the bed roughness was done using the mean sediment diameter D: z_o=D/30 (Nikuradse, 1933). The mean floc size of the sediments is 16 μm in the channels and 20 μm on the mudflat (Law et al, 2011), which gives a very low bed roughness (0.006 mm). However, the high value of z_o estimated from the velocity profiles can be explained by the presence of bed forms (Ke et al., 1994). In situ observations confirm that the tidal flat is incised by ubiquitous runnels and small creeks. Because these bedforms are related to the drainage of the tidal flat at very low water level (Williams et al., 2008; Carling et al., 2009), they lack any prevalent orientation with respect to the main flow and they cannot be directly compared to dunes and ripples found in fluvial environments (e.g. Best, 2005).

Assuming that the bedform-related drag is not contributing to the shear stress responsible for sediment transport (van Rijn, 2007), we choose a single coefficient in the Manning formula (Eq. 3.2), constant for all sites and tidal phases. We take this coefficient equal to 0.016 s $m^{-1/3}$, which, for a water depth equal to 1 m, gives C_D=0.0025, a value commonly used in muddy tidal environments (Whitehouse, 2000). This value corresponds approximately to a bed roughness of 0.2 mm.

3.5 Sediment dynamics

Suspended sediment concentration (SSC) is highly variable within the tidal cycle, among different tidal cycles, and among different locations (Fig. 3.5). During periods without waves, SSC in the BR channel is greater than on the tidal flat for the entire tidal cycle (Fig. 3.5F, 3.5G, 3.7). On the contrary, during periods with wave activity, SSC is greater on the tidal flat than in the BR channel (Fig 5F,3.5G,3.7), in agreement with the higher shear stress induced by waves on the shallow tidal flat (Fig 3.5D,3.5E). Here we will focus on the sediment dynamics without waves (H_s on the tidal flat<0.1m). The role of waves induced resuspension will be considered in the discussion.

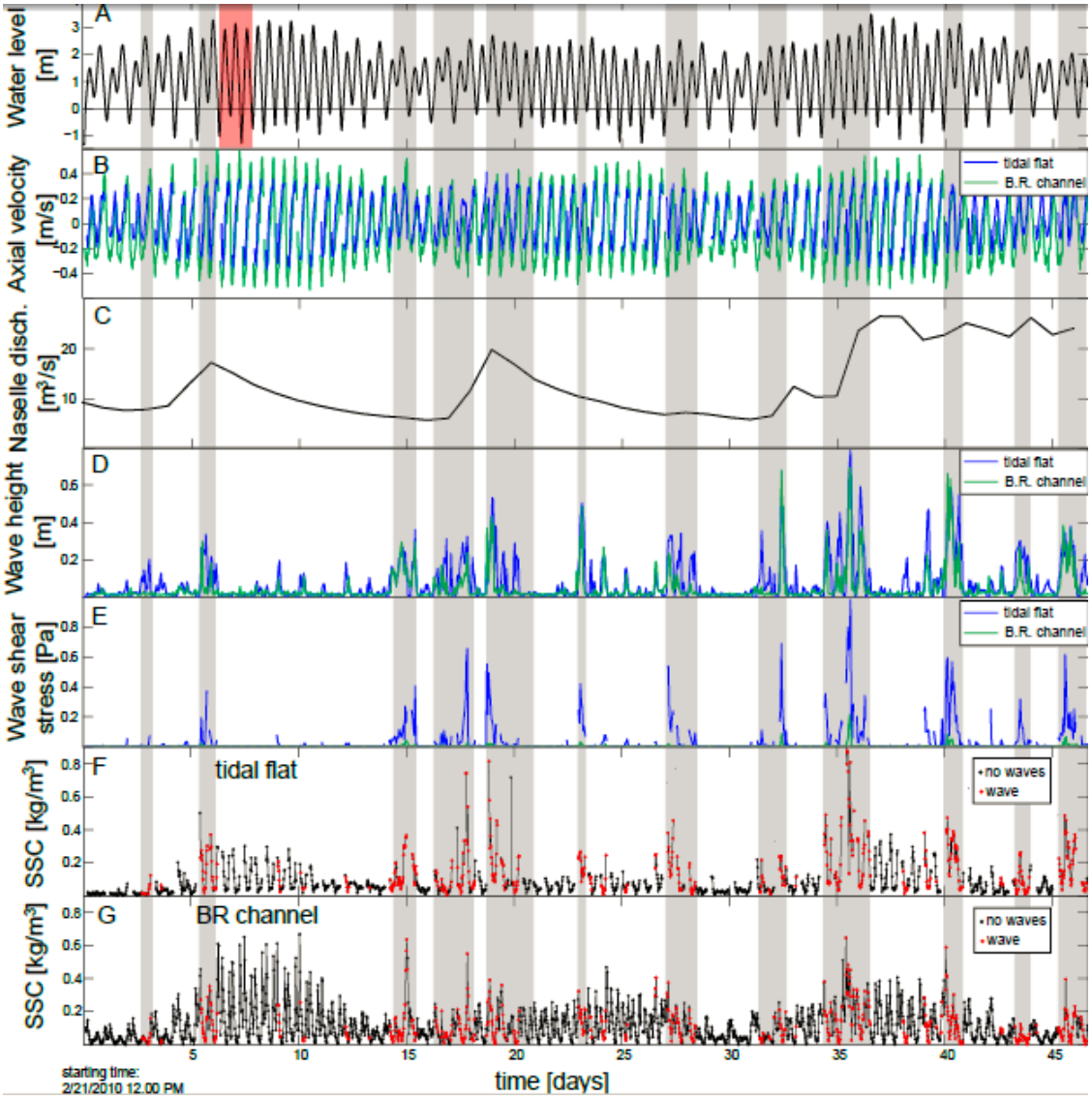

Figure 3.5: Complete time series of the measured physical quantities from 2/21 to 4/9 2010. A) Water level. The red band shows the period between 3/3 and 3/6 2010. B) Axial velocity in the BR channel and on the tidal flat C) Water discharge in the Naselle River (USGS station 12010000). D) Wave height in the BR channel and on the tidal flat. E) Bottom wave shear stress in the BR channel and on the tidal flat. F) SSC on the tidal flat and G) in the BR channel. Black points correspond to no wave activity (Hs<0.1m), red points and grey bands correspond to wave activity (Hs>0.1m).

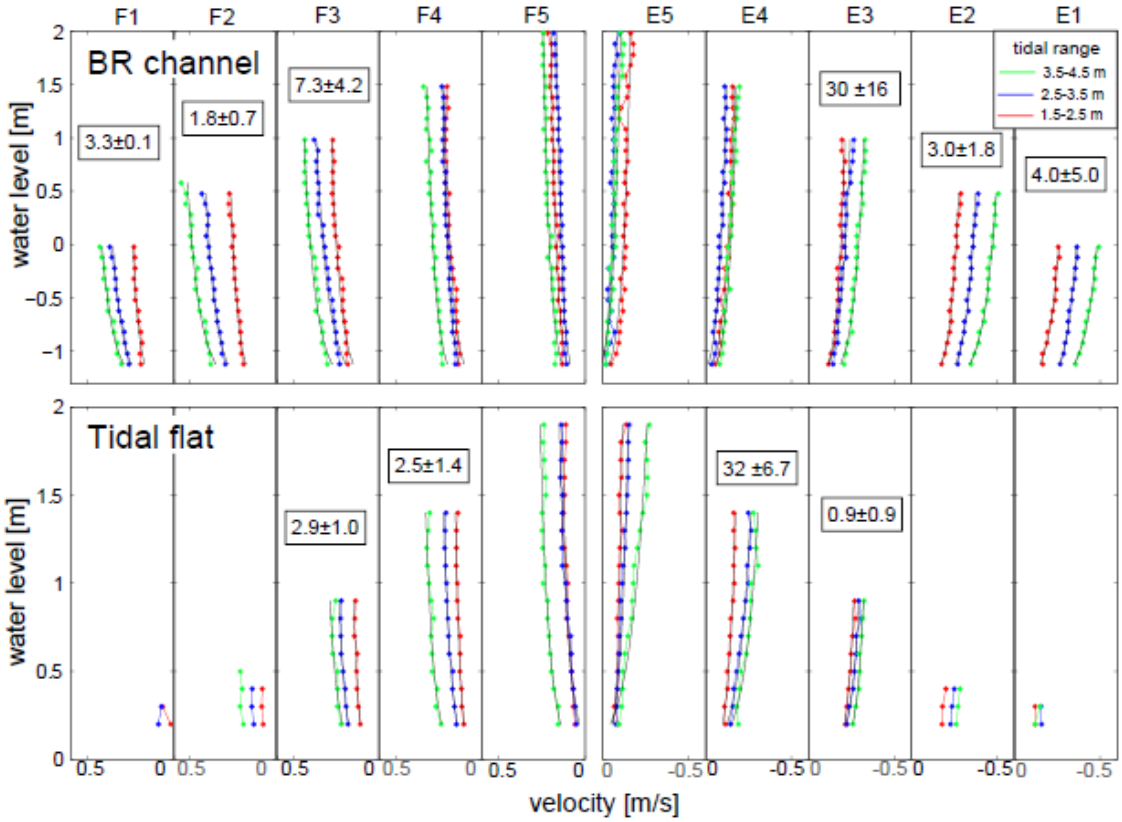

Figure 3.6: Ensemble average profiles, with ensembles defined by 0.25 m bins of water depths and 1 m bins of tidal range. A) BR channel, B) tidal flat. The black continuous line is the log-linear fitting for each ensemble profile. The values in the boxes are the averaged bed roughness (z_o) and its standard deviation for each tidal phase (units in mm).

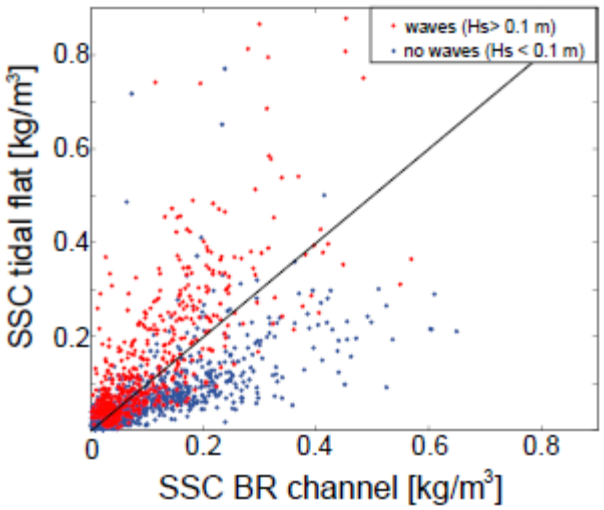

Figure 3.7: SSC in the BR channel and on the tidal flat for periods with waves (Hs on the tidal flat >0.1 m) and without waves (Hs<0.1 m).

3.5.1 Suspended Sediment Concentration (SSC) during fair weather

SSC shows a recursive pattern between different tidal cycles. For simplicity we describe a single tidal cycle, representative of all tides during periods without waves and rainfall.

In the BR channel higher values of SSC (Fig. 3.8A) are found in correspondence with higher axial velocities, which trigger higher shear stresses (Fig. 3.8B). Considering only tidal stages with water level above the tidal flat, SSC in the BR channel correlates well to the current shear stress during both ebb and flood (Fig. 3.9A).

SSC at the bank site peaks at the beginning of the flood (Fig. 3.8A, stage F1), in correspondence with high transverse velocity (Fig. 3.2D, 3.8C). At this stage SSC on the bank and in the BR channel are similar. After this peak, SSC decreases following a reduction of transverse flow (Fig. 3.2D, 3.8C, stage F2). This decrease in SSC is not present in the BR channel. After 1 hour, SSC peaks a second time, reaching a value

close to the SSC in the BR channel (stage F3). This second peak is associated with the maximum longitudinal velocity on the bank. SSC on the bank maintains the same value as the SSC in the BR channel for the rest of the flood and the initial part of the ebb. Toward the end of the ebb, SSC on the bank increases again in correspondence with higher shear stresses (Fig. 3.8A, stage E1), and decreases in correspondence with the ebb peak in transverse velocity (Fig. 3.2D, 3.8C, stage E2).

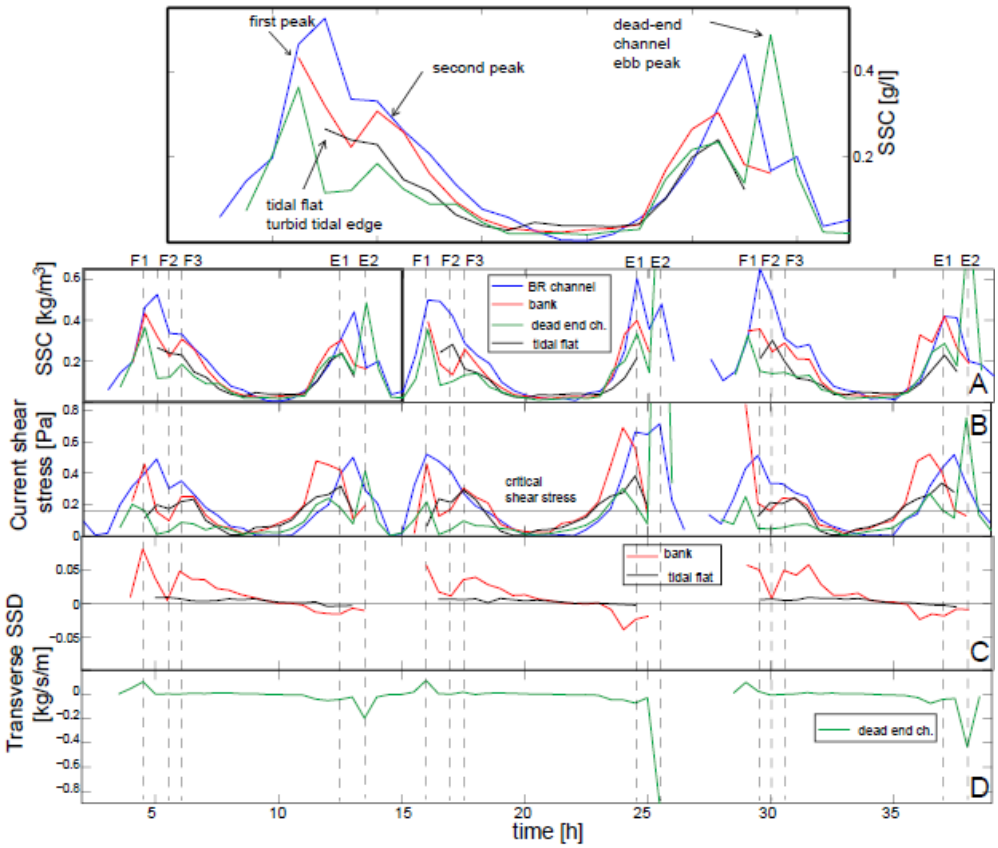

Figure 3.8: Example of the measured physical quantities from 3/3 to 3/6 2010. A) SSC in the BR channel, bank, dead-end channel and tidal flat. B) Current induced shear stress in the BR channel, bank, dead-end channel and tidal flat. The horizontal black line defines the critical shear stress, set equal to 0.15 Pa. C) Transverse suspended sediment discharge at the bank and on the tidal flat. D) Transverse suspended sediment

discharge in the dead-end channel. The vertical dashed lines indicates various stages during flood, F1, F2, and F3, and during ebb, E1 and E2 (see also Fig. 3.10).

SSC in the dead-end channel shows a very similar pattern: a first peak at the beginning of the flood, followed by a decrease in SSC and then by a secondary peak. In this case the secondary peak is lower than on the bank. During the last stage of the ebb SSC increases again to values similar to the bank. Finally, a very high peak of SSC (up to 1 kg/m^3) is found in correspondence with the ebb peak velocity when the tidal flat is exposed (see Mariotti and Fagherazzi 2010). Because the ADCPs on the tidal flat were placed at a higher elevation than on the bank, measurements during the transverse flood peak are not present. The first two measurements of SSC on the tidal flat are always very high (Fig. 3.8A, stage F1-F2), and represent the propagation of the peak of SSC during flood (turbid tidal edge). The turbid tidal edge takes place about 0.5 to 1 hour after the sediment discharge peak measured at the bank location. At this stage the SSC on the tidal flat is nearly equal or higher than on the bank but lower than in the BR channel. After the initial peak, SSC on the tidal flat decreases slowly and steadily, without displaying a secondary peak found at the bank and dead-end channel (stage F3). SSC increases again towards the end of the ebb, in correspondence with higher shear stresses on the tidal flat (stage E1).

The relationship between SSC and currents shear stress on the tidal flat shows an asymmetry between ebb and flood (Fig. 3.9B). During ebb the SSC remains low for shear stress below 0.15 Pa, and then increases fast. Assuming that the low values of SSC (<0.05 kg/m^3) are the background value always present (e.g. wash load), the values

of 0.15 Pa indicates approximately the critical shear stress for erosion on the tidal flat. In situ measurements of critical shear stress produced similar values (Wiberg et al, 2011). On the contrary, during the initial stage of the flood (water depth on the tidal flat < 1 m), elevated SSC are found in correspondence with very low shear stresses (< 0.1 Pa). A similar decoupling between shear stress and SSC was observed in a nearby region of the southern Willapa Bay tidal flat, and was explained by advection of sediment from the adjacent channel (Hill et al, 2001).

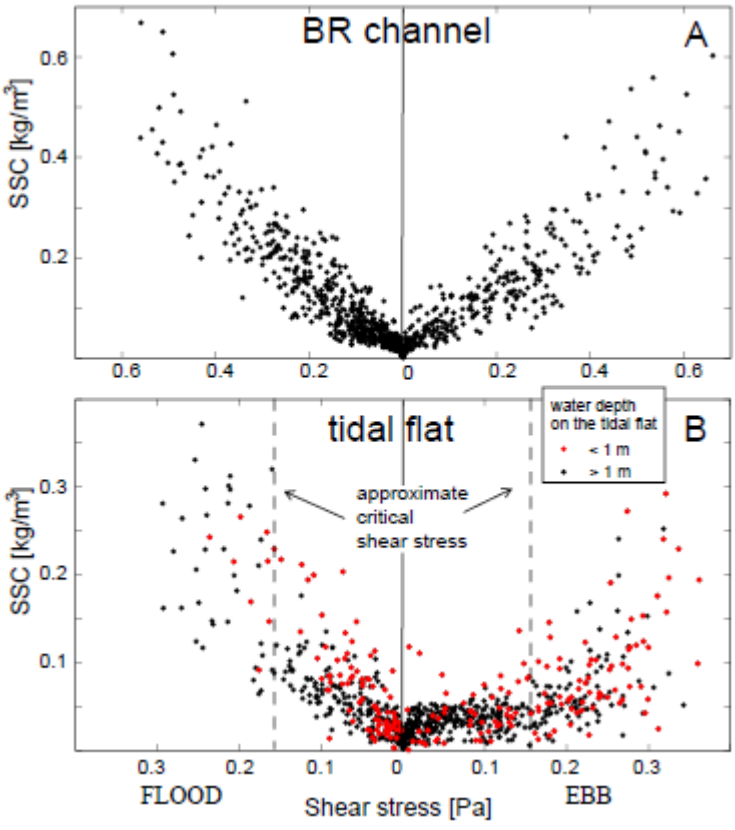

Figure 3.9: SSC against current induced bed shear stress in the BR channel (A), and on the tidal flat (B), for periods without waves. Only tidal stages with water level above the tidal flat are considered. The dashed vertical line is the estimated critical shear stress, equal to 0.15 Pa.

3.5.2 Transverse suspended sediment discharge

The sediment flux from the BR channel is similar to the propagation of a sediment laden salinity front in San Francisco Bay described by Ralston and Stacey (2007) and by Talke and Stacey (2008). At our site however we found advection of sediment which was not associated with a salinity front. A major difference between the two results is that the site in San Francisco Bay was a very small and enclosed tidal flat, with a direct freshwater input from two major tidal creeks. Instead the lower Willapa Bay is an open tidal flat with low freshwater input, at least during our measurements, which is more similar to the site of Warner et al. (2004). Therefore our observations suggest that the advection of sediment from the channel is not associated with the propagation of a salinity front, as also indicated by Warner et al. (2004).

From continuity, the water flowing on the bank in the transverse direction originates from the BR channel, which is characterized by elevated SSC. Therefore the high sediment flux on the bank during the early flood stage (Fig. 3.8C, stage F1) is explained by advection of sediment from the BR channel. The fact that SSC on the bank is almost identical to SSC in the BR channel (Fig. 3.8A, stage F1) suggests that erosion and deposition on the bank are close to a dynamical balance during the water spilling.

There is strong evidence that sediment resuspension from the tidal flat is small compared to the advective flux of sediment from the BR channel. First, laboratory erosion measurements using a Gust-chamber showed that sediment erodability is higher in the channels than on the tidal flat (Wiberg et al., 2011). Second, because of the

increase of sediment resistance caused by dewatering during aerial exposure (Amos et al., 1988; Tolhurst et al. 2006b), sediment erodability on the tidal flat is expected to be low at the beginning of the flood inundations.

Finally, a consideration about the role of dead-end channels in the sediment budget is made. Transverse sediment discharge in the dead-end channel is greater than that on the bank (Fig. 3.8C,D). However, dead-end channels constitute less than 10% of the boundary between the BR channel and the tidal flat. Assuming that the measurements in the dead-end channel and on the bank are representative of these two elements, the width-integrated sediment discharge in the dead-end channel is small compared to that on the bank. Therefore the flux of sediment on the tidal flat during flood is influenced more by the fluxes on the bank than the fluxes in the dead-end channels. The flux of sediment in the dead-end channel becomes instead significant during the last stage of the ebb, when the tidal flat emerges.

3.6 Discussion

3.6.1 Channel - tidal flat sediment exchange

The first measurement on the tidal flat at the beginning of the flood (Fig. 3.8A, stage F1) shows a distinct turbid tidal edge. SSC decreases after the initial peak, even if the local bottom shear stress increases (Fig. 3.8A,B). Similarly, there is a low correlation between SSC and shear stress during flood (Fig. 3.9B). Local resuspension is not a

likely cause of the turbid tidal edge during flood, in agreement with the finding of Black (1998) and Talke and Stacey (2008).

We suggest that the transverse sediment discharge coming from the BR channel is contributing to the formation of the turbid edge on the tidal flat. The sediment discharge peak measured at the bank location takes place around 0.5 to 1 hour before the SSC peak on the tidal flat, which is approximately the time needed for a current of 0.3 m/s to reach the distance between the BR channel and the tidal flat sites (500 m). A simple mass balance reveals the contribution of the lateral discharge to the sediment budget on the tidal flat. We isolate a strip of tidal flat with 1 m length along the BR channel direction. Considering a turbid tidal edge equal to 0.3 kg/m^3, a water depth of 0.3 m, and a tidal flat width equal to 500 m, the amount of sediment in suspension over this strip of tidal flat is 45 kg. At the beginning of the flood (Fig. 3.8C, stage F1), the peak transverse flux from the bank is 0.05 kg/s, which multiplied by a time step (0.5 hours) gives 90 kg. Therefore the amount of sediment transported by the transverse flow is more than sufficient to explain the turbid tidal edge and additional sedimentation on the bank and tidal flat.

The secondary peak of SSC on the bank during flood (Fig. 3.8A, stage F3) is explained by the peak in longitudinal velocity, provided that erodible material is present. The high velocity is probably caused by turbulent transport of momentum, as the water level increases and the bank becomes part of the BR channel. The transverse sediment discharge during the secondary peak (Fig. 3.8C, stage F3) is comparable to that

observed during the first peak (stage F1). However, because of the greater water depth and smaller transverse velocity, SSC does not significatively increase on the tidal flat (Fig. 3.8A).

The transverse velocity during the secondary SSC peak is probably associated with the large scale tidal circulation in the Bay. At high water levels, such as during the stage F3, the flow is less channelized and hence the velocity direction is more affected by the shape of the tidal basin than by the channels orientation. As a result, our analytical model is not able to capture this flow that strongly depends on the overall morphology of the basin.

Finally, during ebb SSC on the tidal flat remains low for most of the time, increasing only toward the end following an increase in shear stress. As suggested by the SSC-shear stress relationship (Fig. 3.9B), local resuspension seems the most probable source of sediment. During ebb SSC in the BR channel is equal or greater than on the tidal flat, and the transverse sediment discharge is oriented toward the BR channel Therefore, even if BR channel is a potential source of sediment, the advective mechanism acts in the opposite way: relative low SSC water is transported from the tidal flat to the BR channel.

3.6.2 The channel spillover mechanism

The simplified analytical model used herein shows how barotropic lateral circulation determines the pattern of transverse velocity observed on the bank and on the tidal flat. According to the model, the maximum lateral discharge takes place when the water

level is just above the tidal flat elevation. This phase corresponds to the higher SSC in the BR channel, and therefore to the phase when the BR channel is a potential source of sediment for the tidal flat.

We delineate a specific process for asymmetric sediment flux on the tidal flat, which we will refer as channel spillover mechanism. The conceptual model is based on the following assumptions:

1) Currents, and hence shear stresses, are higher in the flow-through channel than on the tidal flat.

2) Because of the higher shear stresses, SSC in the flow-through channel are higher than on the tidal flat, during both ebb and flood. This assumption requires that bottom erodability in the channel is equal or greater than that on the tidal flat, as in our study site (Wiberg et al. 2011)

3) The transverse barotropic flow is directed from the flow-through channel to the tidal flat during flood and in the opposite direction during ebb.

Given these constraints, relatively high SSC water is brought from the channel to the tidal flat during flood (Fig. 3.10, stage F1), while relatively low SSC water is brought from the tidal flat to the flow-through channel during ebb (Fig. 3.10, stage E2). The role of the channel bank during flood is neutral, i.e. water coming from the channel to the tidal flat does not change its SSC. This asymmetric pattern results in a net sediment transport from the channel to the tidal flats.

The role of concentration gradients driving sediment across mudflats via tidal dispersion has been already emphasized (Roberts et al, Prtichard et al, 2002; Friedrichs, 2012). The novelty of our conceptual model is to show that this sediment transport mechanism is associated to a specific lateral circulation between a channel and its adjacent tidal flats.

The proposed mechanism presents some similarities with the scour and settling lag mechanism (Postma, 1961): both processes are due to spatial (or Lagrangian) asymmetries (see Friedrichs, 2012 for a review). Settling lag results from the combination of the delay in sedimentation after the velocity has diminished to the point at which particles can no longer be held in suspension, plus one of the following: 1) tidal velocities decreasing landward, 2) water depth decreasing landward, 3) high slack water period greater than the low slack water period (for a review, see Pritchard and Hogg, 2002). The channel spillover mechanism stems from a difference in the boundary condition of SSC and from lateral circulation. This mechanism is present even without 1) variations in velocity along the direction of sediment transport, 2) variations in water depth along the direction of sediment transport, 3) slack water duration asymmetries.

An additional difference is that the settling lag effect is dominant around high slack water, after sediment erosion generated by peak currents. Instead, the channel spillover mechanism is dominant at the beginning of the flood, when the water inundates the tidal flat (Fig. 3.9B, water depths <1m). The proposed mechanism is analogous to the transport of sediment on fluvial floodplains. In both cases sediment is transported in the

main channel, were velocities are higher, and then advected on the adjacent areas, characterized by lower velocities which favors sediment settling.

The channel spillover mechanism proposes an alternative explanation of the turbid tidal edge. Cross sectionally integrated models for axial sediment transport showed that the turbid tidal edge stems from local flow convergence, which tends to accumulate suspended sediment (Friedrichs et al., 1998; Pritchard and Hogg, 2002; Pritchard, 2005). Our model instead suggests that the turbid tidal edge on the tidal flat is formed by transport from a source of elevated SSC, i.e. it is driven by tidal dispersion. The two processes do not exclude each other, and it is plausible that both contribute to the formation of the turbid edge.

The channel spillover mechanism does not require tidal asymmetries, but does not preclude their presence. The mechanism works for both symmetric and asymmetric tides provided that two main processes are present: SSC is higher in the channel and water discharge is directed from the channel to the tidal flat during flood and in the opposite direction during ebb.

During wave events, bottom shear stresses are larger on the tidal flat than in the BR channel leading to higher SSC on the flat surface (Fig. 3.5F,G, 3.7). Therefore wave activity reverses the direction of the channel spillover mechanism. Indeed, several authors (Yang et al, 2003; Ridderinkof, 2000; Janssen-Stelder, 2000) observed higher SSC on tidal flats and sediment flux directed toward subtidal channels during stormy weather.

Finally, the contribution of the dead-end channel flow to the width-integrated transverse sediment discharge is small with respect to the contribution of the overbank flow. The contribution of the dead-end channel is significant only during the very last stage of the ebb, when the water level drops below the tidal flat elevation and the bank is exposed. The ebb pulse in the dead-end channel is associated with extremely shallow drainage (Mariotti and Fagherazzi, 2010), and produces a net export of sediment from the tidal flat.

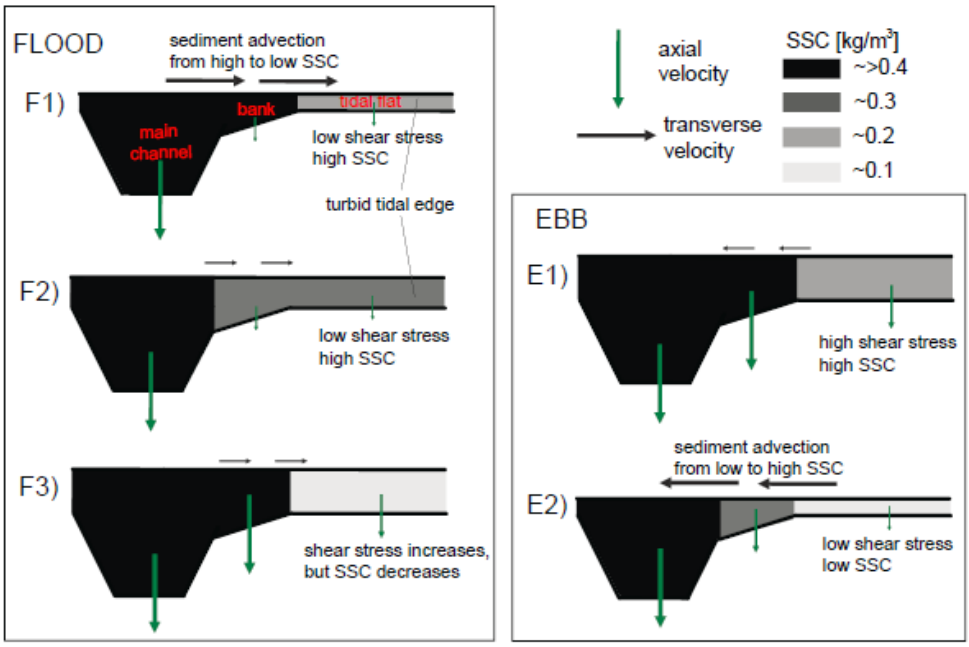

Figure 3.10: Cartoon describing the channel spillover mechanism. Axial velocities and SSC are greater in the channel than on the tidal flat during both ebb and flood. Transverse flow is directed from the channel to the tidal flat during the early flood (F1) and from the tidal flat to the channel during the late ebb (E2). During F1 the sediment advection is a positive term for the SSC balance on the tidal flat, and contributes to the formation of the turbid tidal edge, while during E2 the sediment advection is a negative term for the SSC balance in the BR channel. During mid-flood (F3), high longitudinal velocities on the bank can generate a secondary SSC peak. However, because of the small transverse velocity, the resulting sediment discharge does not substantially increase SSC on the tidal flat.

3.7 Conclusions

We measured a lateral circulation between a large flow-through channel and the adjacent tidal flat in Willapa Bay, Washington State, USA. The lateral velocity is higher at the beginning of the tidal flat inundation and at the end of the tidal flat drainage. A simplified barotropic model suggests that this lateral circulation is generated by the difference in discharge-divergence between the main channel and the tidal flat along the channel direction. This model allows estimating the lateral circulation by continuity arguments only, without solving the propagation of the tidal wave in the longitudinal and lateral direction.

The lateral circulation is characterized by a flux of sediment directed from the BR channel to the tidal flat during flood. This flux likely originates from the elevated SSC in the BR channel and is transported across the bank without significant change. The advection of sediment from the BR channel contributes to the formation of the turbid tidal edge measured on the tidal flat. Even though observations suggested the importance of sediment advection from channels (e.g. Ridderinkhof et al., 2000), this process has never been emphasized and described in detail, nor associated with a specific lateral circulation, nor related to the formation of the turbid tidal edge.

We propose a simple mechanism, called herein channel spillover, which stems from two conditions: 1) higher SSC in the main channel than on the tidal flat, 2) water diverging from the channel during the early phase of the flood and converging during the late

stage of the ebb. According to the channel spillover mechanism, sediments are brought from the main channel to the tidal flat during flood, but not during ebb, generating a net accumulation on the tidal flat.

This mechanism can either occur independently or interact with other sedimentary processes acting on tidal flats. Tidal asymmetries in duration, velocity or stratification are not altering the spillover mechanism, provided that conditions 1) and 2) are present. However, the presence of wind waves increases SSC on the tidal flat more than in the BR channel, reversing the channel spillover mechanism. It is therefore clear that a complete understanding of the tidal flat sediment dynamics requires the coupling between all these processes.

3.8 References

Amos, C.L., N.A. Van Wagoner, and G.R. Daborn, (1988), The influence of subaerial exposure on the bulk properties of fine-grained intertidal sediments from Minas Basin, Bay of Fundy, Estuarine, Coastal and Shelf Science, 27, 1-13.

Allen, J.R.L., and Duffy M.J., (1998), Medium-term sedimentation on high intertidal mudflats and salt marshes in the Severn Estuary, SW Britain: the role of wind and tide, Marine Geology, 150, 1–27.

Ashley, G.M., and M.L. Zeff, (1988), Tidal channel classification for a low-mesotidal salt-marsh, Marine Geology, 82, 1-2, 17-32.

Banas, N.S., B.M. Hickey, P. MacCready, and J.A. Newton, (2004), Dynamics of Willapa Bay, Washington: A highly unsteady, partially mixed estuary, Journal of Physical Oceanography, 34, 11, 2413-2427.

Black, K.S., (1998), Suspended sediment dynamics and bed erosion in the high shore mudflat region of the Humber estuary, UK, Marine Pollution Bulletin, 37, 3-7, 122-133.

Bouws, E., H. Gunther, W. Rosenthal, and C. L. Vincent, (1985), Similarity of the wind wave spectrum in finite depth water. 1 Spectral form, Journal of Geophysical Research, 90 (NC1), 975-986.

de Brouwer, J. F. C., S. Bjelic, M.G.T. de Deckere, and L.J. Stal, (2000), Interplay between biology and sedimentology in a mudflat (Biezelingse Ham, Westerschelde, The Netherlands) , Continental Shelf Research, 20, 10-11, 1159-1177.

Carling, P.A., J.J. Williams, I.W. Croudace, and C.L. Amos, (2009), Formation of mud ridge and runnels in the intertidal zone of the Severn Estuary, UK. Continental Shelf Research, 29, 16, 1913-1926.

Christiansen, C., G. Volund, L. C. Lund-Hansen, and J. Bartholdy, (2006), Wind influence on tidal flat sediment dynamics: Field investigations in the Ho Bugt, Danish Wadden Sea, Marine Geology, 235, 1-4, 75-86.

Christie, M.C., K.R. Dyer, and P. Turner, (1999), Sediment flux and bed level measurements from a macro tidal mudflat, Estuarine Coastal and Shelf Science, 49, 5, 667-688.

Collins, M.B., X. Ke, and S. Gao, (1998), Tidally-induced Flow Structure Over Intertidal Flats, Estuarine, Coastal and Shelf Science, 46, 233–250.

de Swart, H E., and J.T.F. Zimmerman, (2009), Morphodynamics of Tidal Inlet Systems, Annual Review of Fluid Mechanics, 41, 203-229.

Deines, K.L., (1999), Backscatter estimation using broadband acoustic Doppler Current Profilers, 249-253 pp., Ieee, New York.

Downing, A., P.D. Thorne, and C E. Vincent, (1995), Backscattering from a suspension in the near-field of a piston transducer, Journal of the Acoustical Society of America, 97, 3, 1614-1620.

Dyer, K.R., M.C. Christie, N. Feates, M.J. Fennessy, M. Pejrup, and W. van der Lee, (2000), An investigation into processes influencing the morphodynamics of an intertidal mudflat, the Dollard estuary, the Netherlands: I. Hydrodynamics and suspended sediment, Estuarine Coastal and Shelf Science, 50, 5, 607-625.

Eisma, D., (1997), Intertidal Deposits: River Mouths, Tidal Flats and Coastal Lagoons, Marine Science Series, CRC Press, Boca Raton, 507pp.

Fagherazzi, S., P.L. Wiberg, and A.D. Howard, (2003), Tidal flow field in a small basin, Journal of Geophysical Research, 108, C3, 3071.

Fagherazzi, S., and A.M. Priestas, (2010), Sediments and water fluxes in a muddy coastline: interplay between waves and tidal channel hydrodynamics, Earth Surface Processes and Landforms, 35, 3, 284-293.

Friedrichs, C.T., B.A. Armbrust, and H.E. de Swart, (1998), Hydrodynamics and equilibrium sediment dynamics of shallow, funnel-shaped tidal estuaries. In: J. Dronkers and M. Scheffers (Eds.), Physics of Estuaries and Coastal Seas, Balkema Press, Rotterdam, The Netherlands, p. 315-328.

Friedrichs, C.T., and D.G. Aubrey, (1988), Non-linear Tidal Distortion in Shallow Well-mixed Estuaries: a Synthesis, Estuarine, Coastal and Shelf Science, (1988) 27,521-545.

Friedrichs, C. T., and O. S. Madsen, (1992), Nonlinear Diffusion of the Tidal Signal in Frictionally Dominated Embayments, Journal of Geophysical Research, 97, C4, 5637-5650.

Friedrichs, C.T., (2012), Tidal flat morphodynamics: a synthesis. In: J.D. Hansom and B.W. Flemming (Eds.), Treatise on Estuarine and Coastal Science, Volume 3: Estuarine and Coastal Geology and Geomorphology, Elsevier, in press.

Gartner, J.W., (2004), Estimating suspended solids concentrations from backscatter intensity measured by acoustic Doppler current profiler in San Francisco Bay, California, Marine Geology, 211, 3-4, 169-187.

Geyer, W.R., (1993), The importance of suppression of turbulence by stratification on the estuarine turbidity maximum, Estuaries, 16, 1, 113-125.

Gibbons, D.T., G. Jones, A. Hay, and F. Johnson, (1983), Performance of a new submersible tide-wave recorder, UNESCO, Technical paper in marine science.

Gloor, M., A. Wuest, and M. Munnich, (1994), Benthic boundary mixing and resuspension induced by internal seiches, Hydrobiologia, 284, 1, 59-68.

Green, M.O., and G. Coco, (2007), Sediment transport on an estuarine intertidal flat: Measurements and conceptual model of waves, rainfall and exchanges with a tidal creek, Estuarine Coastal and Shelf Science, 72, 4, 553-569.

Green, M.O., K.P. Black, and C.L. Amos, (1997), Control of estuarine sediment dynamics by interactions between currents and waves at several scales, Marine Geology, 144, 1-3, 97-116.

Hickey, B.M., and N.S. Banas, (2003), Oceanography of the US Pacific Northwest Coastal Ocean and estuaries with application to coastal ecology, Estuaries, 26(4B), 1010-1031.

Hill, P.S., J.P. Newgard, B.A., Law, and T.G. Milligan, (2011), Linking suspended floc dynamics to the spatial distribution of sediment texture on the Shoalwater Bay tidal complex in Willapa Bay, Continental Shelf Research, submitted to special issue: Tidal Flats.

Hoitink, A.J.F., and P. Hoekstra, (2005), Observations of suspended sediment from ADCP and OBS measurements in a mud-dominated environment, Coastal Engineering, 52, 2, 103-118.

Hoitink, A.J.F., P. Hoekstra, and D.S. van Maren, (2003), Flow asymmetry associated with astronomical tides: Implications for the residual transport of sediment, Journal of Geophysical Research, 108(C10).

Hsu, T.J., S.N. Chen, and A.S. Ogston, (2011), A numerical investigation of fine sediment transport across intertidal flats, Continental Shelf Research, submitted to special issue: Tidal Flats.

Janssen-Stelder, B., (2000), The effect of different hydrodynamic conditions on the morphodynamics of a tidal mudflat in the Dutch Wadden Sea, Continental Shelf Research, 20, 1461-1478.

Ke, X.K., M.B. Collins, and S.E. Poulos, (1994), Velocity structure and sea-bed roughness associated with intertidal (sand and mud) flats and salt-marshes of the wash, UK, Journal of Coastal Research, 10, 3, 702-715.

Kornman, B.A., and E.M.G.T. de Deckere, (1998), Temporal variation in sediment erodibility and suspended sediment dynamics in the Dollard estuary. In: Black, K. S., Paterson, D. M., Cramp, A. (Eds.), Sedimentary Processes in the Intertidal Zone, Geological Society, London, Special Publications 139, pp. 231–241.

Lacy, J.R., M.T. Stacey, J.R. Burau, and S.G. Monismith, (2003), Interaction of lateral baroclinic forcing and turbulence in an estuary, Journal of Geophysical Research, 108(C3), 3089.

Law, B.A., T.G. Milligan, P.S. Hill, J. Newgard, R.A. Wheatcroft, and P.L. Wiberg, (2011), Bed sediment texture on the Shoalwater Bay tidal complex, Willapa Bay: role of flocculation, Continental Shelf Research, submitted to special issue: Tidal Flats.

Le Hir, P., W. Roberts, O. Cazaillet, M. Christie, P. Bassoullet, and C. Bacher, (2000), Characterization of intertidal flat hydrodynamics, Continental Shelf Research, 20, 12-13, 1433-1459.

Le Hir, P., Y. Monbet, and F. Orvain, (2007), Sediment erodability in sediment transport modelling: Can we account for biota effects?, Continental Shelf Research, 27, 8, 1116-1142.

Li, C.Y., and J. O' Donnell, (1997), Tidally driven residual circulation in shallow estuaries with lateral depth variation, Journal of Geophysical Research, 102(C13), 27915-27929.

Li, C.Y., and A. Valle-Levinson, (1999), A two-dimensional analytic tidal model for a narrow estuary of arbitrary lateral depth variation: The intratidal motion, Journal of Geophysical Research, 104(C10), 23525-23543.

Li, C.Y., and J. O' Donnell, (2005), The effect of channel length on the residual circulation in tidally dominated channels, Journal of Physical Oceanography, 35, 10, 1826-1840.

Mariotti, G., and S. Fagherazzi, (2011), Asymmetric fluxes of water and sediments in a mesotidal mudflat channel, Continental Shelf Research, 31, 1, 23-36.

Nidzieko, N. J., (2010), Tidal asymmetry in estuaries with mixed semidiurnal/diurnal tides, Journal of Geophysical Research, 115, C08006.

Nikuradse, J., (1933), Stromungsgesetz in rauhren rohren, vDI Forschungshefte 361 (English translation: Laws of flow in rough pipes). Tech. Rep. NACA Technical

Memorandum 1292, National Advisory Commission for Aeronautics, Washington, D. C., USA (1950).

Nowacki, D.J., and A.S. Ogston, (2011), Water and sediment transport of channel-flat systems in a mesotidal mudflat: Willapa Bay, Washington, Continental Shelf Research, submitted to special issue: Tidal Flats.

Pejrup, M., (1988), Suspended sediment transport across a tidal flat, Marine Geology, 82, 3-4, 187-198.

Peterson, C., K. Scheidegger, P. Komar, and W. Niem, (1984), Sediment composition and hydrography in 6 high-gradient estuaries of the northwestern united-states, Journal of Sedimentary Petrology, 54, 1, 86-97.

Postma, H., (1961), Transport and accumulation of suspended matter in the dutch Wadden Sea, Netherland journal of sea research, 1, 148-190.

Pritchard, D., (2005), Suspended sediment transport along an idealised tidal embayment: settling lag, residual transport and the interpretation of tidal signals, Ocean Dynamics, 55, 2, 124-136.

Pritchard, D., A.J. Hogg, and W. Roberts, (2002), Morphological modelling of intertidal mudflats: the role of cross-shore tidal currents, Continental Shelf Research, 22, 11-13, 1887-1895.

Ralston, D.K., and M.T. Stacey, (2005), Longitudinal dispersion and lateral circulation in the intertidal zone, Journal of Geophysical Research, 110, C07015.

Ralston, D.K., and M.T. Stacey, (2007), Tidal and meteorological forcing of sediment transport in tributary mudflat channels, Continental Shelf Research, 27, 10-11, 1510-1527.

Ridderinkhof, H., R. van der Ham, and W. van der Lee, (2000), Temporal variations in concentration and transport of suspended sediments in a channel-flat system in the Ems-Dollard estuary, Continental Shelf Research, 20, 12-13, 1479-1493.

Roberts, W., P. Le Hir, and R.J.S. Whitehouse, (2000), Investigation using simple mathematical models of the effect of tidal currents and waves on the profile shape of intertidal mudflats, Continental Shelf Research, 20, 10-11, 1079-1097.

Simpson, J.H., J. Brown, J. Matthews, and G. Allen, (1990), Tidal straining, density currents, and stirring in the control of estuarine stratification, Estuaries, 13, 2, 125-132.

Sommerfield, C.K., and K.C. Wong, (2011), Mechanisms of sediment flux and turbidity maintenance in the Delaware Estuary, Journal of Geophysical Research, 116, C01005.

Song, Y., and D.B. Haidvogel, (1994), A semi-implicit ocean circulation model using a generalized topography-following coordinate, Journal of Computational Physics, 115, 1, 228–244.

Soulsby, R.L., and K.R. Dyer, (1981), The form of the near-bed velocity profile in a tidally accelerating flow, Journal of Geophysical Research-Oceans, 86(NC9), 8067-8074.

Soulsby, R.L. (1997), Dynamics of Marine Sands, pp. 250, Thomas Telford Publications, London, Thomas Telford Publications.

Speer, P.E., and D.G. Aubrey, (1985), A Study of Non-linear Tidal Propagation in Shallow Inlet/Estuarine Systems. Part II: Theory, Estuarine, Coastal and Shelf Science, 21, 207-224.

Stacey, M.T., and D.K. Ralston, (2005), The scaling and structure of the estuarine bottom boundary layer, Journal of Physical Oceanography, 35, 1, 55-71.

Talke, S.A., and M.T. Stacey, (2008), Suspended sediment fluxes at an intertidal flat: The shifting influence of wave, wind, tidal, and freshwater forcing, Continental Shelf Research, 28, 6, 710-725.

Tolhurst, J., E.C. Defew, R. G. Perkins, A. Sharples, and D.M. Paterson, (2006), The effects of tidally-driven temporal variation on measuring intertidal cohesive sediment erosion threshold, Aquatic Ecology, 40, 4, 521-531.

Tolhurst, J., E.C. Defew, J.F.C. de Brouwer, K. Wolfstein, L.J. Stal, and D.M. Paterson, (2006b), Small-scale temporal and spatial variability in the erosion threshold and properties of cohesive intertidal sediments, Continental Shelf Research, 26, 351-362.

Tolhurst, T.J., C.W. Watts, S. Vardy, J. E. Saunders, M.C. Consalvey, and D.M. Paterson, (2008), The effects of simulated rain on the erosion threshold and biogeochemical properties of intertidal sediments, Continental Shelf Research, 28, 10-11, 1217-1230.

Tucker, M.J., and E.G. Pitt, (2001), Waves in ocean engineering, 521 pp., Elsevier, The Netherlands.

Uncles, R.J., and J.A. Stephens, (2000), Observations of currents, salinity, turbidity and intertidal mudflat characteristics and properties in the Tavy Estuary, UK, Continental Shelf Research, 20, 12-13, 1531-1549.

Uncles, R.J., R.C.A. Elliott, and S.A. Weston, (1986), Observed and computed lateral circulation patterns in a partly mixed estuary, Estuarine Coastal and Shelf Science, 22, 4, 439-457.

van Rijn, L.C., (2007), Unified view of sediment transport by currents and waves. I: Initiation of motion, bed roughness, and bed-load transport, Journal of Hydraulic Engineering, 133, 6, 649-667.

Warner, J.C., D.H. Schoellhamer, C.A. Ruhl, and J.R. Burau, (2004), Floodtide pulses after low tides in shallow subembayments adjacent to deep channels, Estuarine Coastal and Shelf Science, 60, 2, 213-228.

Whitehouse, R.J.S., and H.J. Mitchener, (1998), Observations of the morphodynamics behavior of an intertidal mudflat at different timescales, In: Black, K.S., Paterson, D.M., Cramp, A. (Eds.) Sedimentary Processes in the Intertidal Zone. Geological Society, London, Special Publication, 139, 255-271.

Wiberg, P.L., and C.R. Sherwood, (2008), Calculating wave-generated bottom orbital velocities from surface-wave parameters, Computers & Geosciences, 34, 10, 1243-1262.

Wiber, P.L., R. Wheatcroft, P. Hill, T. Milligan, B. Law and J. Newgard, (2011), Sediment erodibility on a tidal flat: channel complexes in southern Willapa Bay, Continental Shelf Research, submitted to special issue: Tidal Flats.

Williams, J.J., P.A. Carling, C.L. Amos, and C. Thompson, (2008), Field investigation of ridge-runnel dynamics on an intertidal mudflat, Estuarine Coastal and Shelf Science, 79, 2, 213-229.

Winterwerp, J.C., (2011), Fine sediment transport by tidal asymmetry in the high-concentrated Ems River: indications for a regime shift in response to channel deepening, Ocean Dynamics, 61, 2-3, 203-215.

Yang, S., C.T. Friedrichs, Z. Shi, P. Ding, J. Zhu, and Q. Zhao, (2003), Morphological response of tidal marshes, flats and channels of the outer Yangtze river mouth to a major storm, Estuaries, 26, 6, 1416–1425.

Chapter 4. A dynamical model for the coupled evolution of channels and tidal flats

The contents of this chapter are based on a paper submitted to Journal of Geophysical Research – Earth Surface. This paper was co-authored with S. Fagherazzi (Department of Earth Science, Boston University).

Abstract

A dynamical model for the morphological evolution of channels and tidal flats is proposed. Both channels and tidal flats are schematized as sediment reservoirs, whose depths are the only two dynamical variables of the system. The two reservoirs exchange sediments through the tidal dispersion mechanism. The reference concentrations are determined by currents and waves, which are function of the geometry of the system. The hydrodynamic component of our simplified model is compared to the numerical model Delft3D, showing good agreement. The morphological model shows that, without wind waves, a flat bottom is unstable and the only stable configuration is a channel without tidal flats. For intermediate wave conditions, a non-trivial stable equilibrium arises, characterized by a channel flanked by tidal flats. Intense waves suppress the channelization process, and a flat bed becomes then only stable equilibrium. Finally, relative sea level rise allows the coexistence of channels and tidal flats, even in absence of waves.

4.1. Introduction

Intertidal areas feature two distinct morphological units: channels and tidal flats. Despite these two elements are strongly coupled, their morphological evolution is often studied independently, hampering a comprehensive understanding of the system.

Tidal channels are generally studied with a one-dimensional schematization (Friedrichs, 1995; Lanzoni and Seminara, 2002; Seminara et al., 2009; Toffolon and Lanzoni, 2010). In these frameworks tidal flats are considered as water storage areas, without participating in the momentum dynamics. This storage effect promotes ebb dominance and hence a net seaward transport of sediments (Speer and Aubrey, 1985; Friedrichs and Aubrey, 1988). The channel morphological evolution is based on channel hydrodynamics, computed assuming that the tidal flat is a fixed element that does not evolve in time.

On the other hand, tidal flats are generally schematized as a transect parallel to the main flow direction (Le Hir et al., 2000; Roberts et al, 2000; Pritchard et al, 2002; Pritchard and Hogg, 2003; Mariotti and Fagherazzi, 2010). As a result the draining effect of channels and the consequent reduction of flow on the tidal flat are neglected. In these models the tidal flat transect is coupled with the rest of the system through a sediment boundary condition at the seaward end. This boundary condition represents the dynamics of the rest of the system, such as sediment inputs from channels adjacent to

the tidal flat. Because this boundary condition is set a priori, the coupling between tidal flat and channel hydrodynamics is neglected.

A number of observations have been carried out in both channels and tidal flats, shedding light on the main sedimentary mechanisms at play in these environments. Because of the higher current velocity, tidal channels are often characterized by a suspended sediment concentration higher than nearby tidal flats during fair weather (Ridderinkof, 2000; Janssen-Stelder, 2000). During storms the reduced water depths on tidal flats allow a strong penetration of the wave motion, resulting in higher bottom shear stresses and substrate remobilization (Dyer et al., 2000; Christiansen et al., 2006). Because of these dynamics, sediments are preferentially transported from channels to tidal flats during fair weather and from tidal flats to channels during storms (Yang et al., 2003; Allen and Duffy, 1998).

In order to quantify the sediment exchange between channels and tidal flats, three processes should be taken into account: i) sediment resuspension in the channels (e.g. Lanzoni and Seminara, 2002), wave resuspension on the tidal flats (e.g. Fagherazzi and Wiberg, 2009), and lateral circulation between the two (e.g. Li and O'Donnell, 1997; Mariotti and Fagherazzi, 2012b). In addition, in order to close the sedimentary budget, sediment exchange with the continental shelf should be included. In fact the flux of fine material exiting a tidal basin during stormy weather is considered a major component of the sediment budget (e.g. Tambroni and Seminara, 2006).

In this paper we develop a dynamical model for the coupled morphological evolution of channels and tidal flats. A suite of simplified models compute the flow repartition between a channel and a tidal flat, the effect of wind waves, and the exchange of sediments with the continental shelf. The model predicts the system trajectories, the equilibrium points, and their bifurcations as a function of tidal range, wind speed, and relative sea level rise.

4.2 The channel tidal-flat model

In order to determine the equilibrium points and the evolution trajectories of the system we express its dynamics in terms of ODEs of the two independent variables, the depth of the channel, d_c, and the depth of the tidal flat, d_f. Below we report the details of the model and its governing equations.

4.2.1. Schematization and morphological model

The model considers channels and tidal flats as two sediment reservoirs whose volume changes in time. We consider a schematic basin, with a single rectangular channel bounded by a rectangular tidal flat at each side and connected to the open sea through a single inlet (Fig. 4.1). The total width of the channel, $2b_c$, the width of a single tidal flat, b_f, and their lengths are kept fixed. The depths of the channel and tidal flat, d_c and d_f, are the only dynamic variables of the system. For simplicity, the vertical datum is fixed at Mean Higher High Water (MHHW) and the depths are considered positive below this datum. A single-frequency tide with amplitude a is considered, and hence MHHW will be simply referred as High Water (HW). In this reference frame, Low Water (LW)

coincides with 2*a*. Because the horizontal extension of both channel and tidal flat is fixed, d_c and d_f are univocal indicators of the amount of sediment present in the channel and tidal flat reservoirs.

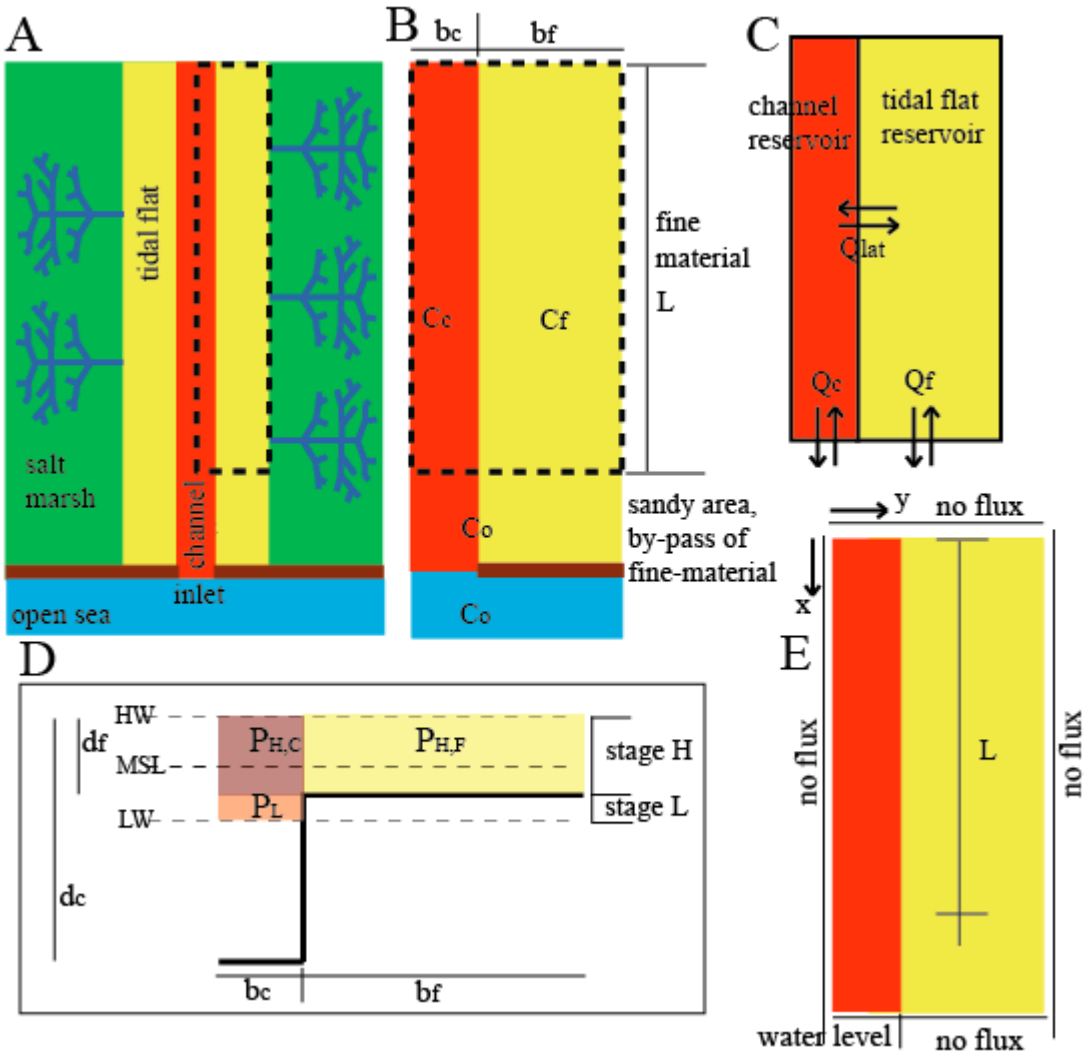

Figure 4.1. A) Scheme of the modeled tidal basin composed of open sea, tidal channel, tidal flats, and salt marshes. B) Detail of the control volume considered. Two sediment reservoirs are selected: channel and adjacent tidal flat. The basin length, *L*, and the channel and tidal flat widths, b_c and b_f, are constant parameters. The dynamical variables are the channel and tidal flat depths, d_c and d_f. C) Scheme of the fluxes between the two sediment reservoirs and the open sea. D) Schematization of the channel and tidal flat cross section. Identification of the tidal volumes for different tidal stages

(see Eqs. 4,5). E) Model domain and boundary conditions used for the hydrodynamic numerical simulations with Delft3D.

We assume that the sediment in the basin is composed by very fine material (D_{50}=100 microns), which is prevalently transported in suspension. Because of the elevated mobility of the sediments, we assume that the reference sediment concentrations in the channel, C_c, and on the tidal flat, C_f, are uniform in space.

In addition, we assume that the substrate near the inlet is sandy, since all the fine material is resuspended by strong tidal currents and by swell waves at the seaward side (FitzGerald, 1996, Tambroni and Seminara, 2006). We also assume that the reference concentration in this region is identical to that of the open sea close to the tidal inlet, C_o.

Because of the system symmetry, we isolate a control volume composed of half channel and one lateral tidal flat (Fig. 4.1B). The control volume ends at the region close to the inlet characterized by coarse material. The effective length of the control volume is L.

The channel and tidal flat reservoirs exchange sediments between them and with the open-sea. We assume that the tidally-averaged transport is dominated by tidal dispersion (Okubo, 1973; Dronkers, 1978; Di Silvio et al., 2010). Tidal dispersion is driven by an exchange flow, symmetrical with respect to ebb and flood, combined to gradients in sediment concentration. In our simplified model the sediment gradients result from the different sediment concentrations in the channel, on the tidal flat, and in the open sea. Residual transport, i.e. ebb-flood flow asymmetries, is neglected.

We schematize the flow exchange in three parts: flow between tidal flat and open sea, between channel and open sea, and between tidal flat and channel (Fig. 4.1C). The tidally-averaged sediment mass balance for the channel and tidal flat reservoirs reads:

$$\begin{aligned}\frac{d\left(d_c\right)}{dt} &= \left[Q_{lat}\left(C_c - C_f\right) + Q_c\left(C_c - C_o\right)\right] / \left[b_c L \rho_s\right] + RSLR - S \\ \frac{d\left(d_f\right)}{dt} &= \left[Q_{lat}\left(C_f - C_c\right) + Q_f\left(C_f - C_o\right)\right] / \left[b_f L \rho_s\right] + RSLR - S\end{aligned} \quad \text{, (Eq. 4.1)}$$

where Q_c is the tidally-averaged longitudinal volume-exchange rate from the channel unit, Q_f is the tidally-averaged longitudinal volume-exchange rate from the tidal flat unit, Q_{lat} is the tidally-averaged volume-exchange rate between the channel and tidal flat units, and ρ_s is the apparent sediment density. *RSLR* is the relative sea level rise, which is simulated keeping the tidal datum fixed and increasing uniformly the channel and tidal flat depths. *S* is the sedimentation rate (per unit of area) due to sediment inputs from rivers discharging in the basin or due to erosion of salt marshes. The sedimentation rate is assumed to occur uniformly in both channel and tidal flat. For simplicity, we combine sea level rise and sediment inputs in the net exogenous erosion: $E_o = RSLR\text{-}S$. Salt marsh extension is considered fixed, which allows to keep both the basin length (L) and width B ($=b_c+b_f$) constant in time. In future research, we will relax this hypothesis to study the spatial evolution of the domain, driven for example by salt marsh boundary erosion.

We assume that the reference concentrations in the channel, subscript *c*, and in the tidal flat, subscript *f*, are such that erosion and deposition are identical. Assuming that the

deposition rate is equal to $w_s C_{c/f}$ and that the erosion rate is $m_e \max\left[\left(\tau_{c/f} - \tau_{cr}\right)/\tau_{cr}, 0\right]$ we obtain (Whitehouse, 2000):

$$C_{c/f} = \max\left(\frac{\tau_{c/f} - \tau_{cr}}{\tau_{cr}}, 0\right)\frac{m_e}{w_s}, \text{ (Eq. 4.2)}$$

where w_s is the reference settling velocity, m_e is the erosion coefficient, $\tau_{c/f}$ is the reference shear stress in the channel or in the tidal flat, and τ_{cr} is the critical shear stress for erosion. We assume that waves and currents act independently determining the reference sediment concentrations in both the channel and tidal flat:

$$C_{c/f} = \lambda_w \max\left(\frac{\tau_{w,c/f} - \tau_{cr}}{\tau_{cr}}, 0\right)\frac{m_e}{w_s} + \lambda_{cur} \max\left(\frac{\tau_{cur,c/f} - \tau_{cr}}{\tau_{cr}}, 0\right)\frac{m_e}{w_s}, \text{ (Eq. 4.3)}$$

where $\tau_{w,c/f}$ are the reference wave-induced shear stresses in the channel or tidal flat, $\tau_{cur,c/f}$ are the reference current-induced shear stresses in the channel or tidal flat, and λ_w and λ_{cur} are the frequencies of the wave and current resuspension processes normalized to a tidal cycle. Because the current-induced shear stresses are constantly present when water is transported, λ_{cur} is equal to one. λ_w depends on the magnitude of the wind event (U_{wind}) considered to calculate τ_w. For simplicity, we select the wind event that takes place on average every tidal cycle, and hence we fix λ_w equal to one. The intensity of such wind event is then the control parameter for the wind process. An alternative approach would be to fix a wind speed, e.g. 10 m/s, and consider λ_w as the control parameter.

The model structure is briefly illustrated in Fig. 4.2. The complex hydrodynamics and sediment transport in a tidal basin is simplified in the following way: i) the fluxes of water are calculated from the tidal prism; ii) the tidal prism is partitioned between tidal flat and channel as a function of water depth, following a simplification of the momentum equation; iii) from the water fluxes, a characteristic tidal current velocity is obtained; this velocity is used to calculate current bottom shear stresses; iv) wave bottom shear stresses are calculated as a function of wind speed, fetch, and depth; v) fluxes of sediments result by the combination of water fluxes and reference suspended sediment concentrations, computed as function of wave and current shear stresses; vi) the sediment fluxes determine erosion and deposition at the bottom of the channel and tidal flat and therefore the evolution of the system.

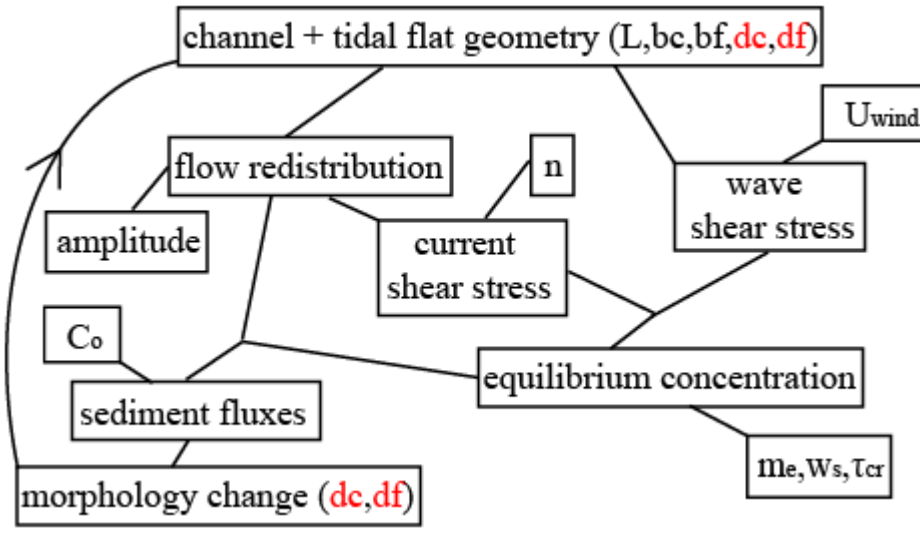

Figure 4.2: Model structure: processes and driving parameters. Given the channel and tidal flat geometry, a hydrodynamic model computes the flow repartition between channel and tidal flat and related current shear stresses, while a wave model computes wave shear stresses. The reference sediment concentrations are computed from the

shear stresses, and they are combined with the water fluxes and the open-sea concentration to obtain the sediment fluxes, which modify the system morphology. The red variables are the unknowns in our model while the black variables are the fixed parameters.

4.2.2. Hydrodynamic model for flow redistribution

Here we propose a simplified model for the flow in the channel and tidal flat. We assume that the hydrodynamics is tidally dominated, neglecting the presence of wind driven currents, seiches, riverine circulation, and stratification. Considering short basins only (e.g. L << tidal wave length), we assume the tide to be quasi-static, so that the water level is uniform in space (Fagherazzi et al., 2003). We also assume that the tidal prism above the salt marsh is negligible with respect to the tidal prism in the basin, which is the case when the salt marsh level is close to the HW and the tidal creek network is limited.

We consider two stages: stage H, when the tidal flat is submerged, and stage L, when the tidal flat is emergent (Fig. 4.1D). Stage H considers water levels between HW and the tidal flat elevation, while stage L considers water levels between the tidal flat elevation and LW. The tidal prisms for the channel, $P_{H,c}$, and tidal flat $P_{H,f}$, for stage H are:

$$\begin{aligned} P_{H,f} &= \min(d_f, LW) Lb_f \\ P_{H,c} &= \min(d_f, LW) Lb_c \end{aligned} \quad \text{(Eq. 4.4)}$$

According to this equation, the tidal prism changes when the tidal flat elevation is above or below LW. The total tidal prism for stage H, P_H, is the sum of $P_{H,f}$ and $P_{H,c}$. In addition, the channel tidal prism for stage L is:

$$P_L = \min\left(LW - \min\left(LW, d_f\right), d_c - d_f\right) Lb_c \text{. (Eq. 4,5)}$$

We then introduce a simplified model to redistribute the flow between the channel and the tidal flat during stage H. We assume that the flow in the longitudinal direction is in equilibrium with bottom friction, according to the Manning equation:

$$U = \frac{1}{n} h^{2/3} i^{1/2} \text{, (Eq. 4.6)}$$

where n is the Manning's coefficient, i is the longitudinal barotropic gradient, and h is the effective water depth. This depth takes into account that the water level varies during the tidal cycle, and it is set equal to the average between the minimum and maximum water depth in both channel and tidal flat:

$$h_{c/f} = \left[d_{c/f} + \max(0, d_{c/f} - LW) \right] / 2 \text{. (Eq. 4.7)}$$

If the unit is exposed at low tide, the effective depth is equal to half the maximum depth; if the unit is not exposed, the effective depth is equal to the maximum depth minus the tidal amplitude. Assuming that i is uniform along each cross section, the redistribution of the longitudinal discharge between channel and tidal flat is proportional to $h^{5/3}$ (Mariotti and Fagherazzi, 2012b). The total volume of water exiting the channel, V_c, and the tidal flat, V_f, in the longitudinal direction becomes:

$$V_c = P_L + P_H \frac{b_c h_c^{5/3}}{\left(b_c h_c^{5/3} + b_f h_f^{5/3}\right)} \quad \text{. (Eq. 4.8)}$$
$$V_f = P_H \frac{b_f h_f^{5/3}}{\left(b_c h_c^{5/3} + b_f h_f^{5/3}\right)}$$

According to this simple model, the repartition of the water fluxes between channel and tidal flat increases when the difference in water depth increases. This repartition depends on the ratio between the channel and tidal flat width, but not on their absolute value (Mariotti and Fagherazzi, 2012b). The volume exchanged between channel and tidal flat normal to the channel direction is computed from the conservation of mass, as the residual between the tidal prism above the tidal flat and the volume exiting the tidal flat along the longitudinal direction (Mariotti and Fagherazzi, 2012b):

$$V_{lat} = P_{H,f} - V_f \quad \text{. (Eq. 4.9)}$$

The volumes V_c, V_f, V_{lat} are divided by the tidal period T_ω to obtain the tidally averaged volume exchange rates Q_c, Q_f, Q_{lat} used in Eq. 4.1. Noticeably, the proposed equations do not depend on the channel longitudinal profile, but only on its depth at the terminal section. This condition is met if the channel depth is lower than LW at every location, so that the tidal prism can be computed using Eq. 4.4.

4.2.3. Current shear stresses

In order to compute the current shear stress, a reference velocity is needed. Here we choose the maximum velocity through a tidal cycle. In fact, because of the non-linearity

in sediment erosion (Eq. 4.2), the reference velocity cannot be assumed to be equal to the average velocity.

The maximum velocity in the channel and in the tidal flat is computed assuming the quasi static tide propagation (Boon, 1975; Fagherazzi et al., 2008), dividing the volume of water per unit of width flowing in the longitudinal direction by the reference depth and by an effective tidal time T_e:

$$U_{c/f} = \frac{V_{c/f}}{b_{c/f} h_{c/f} T_{e,c/f}} \frac{\pi}{2}. \text{ (Eq. 4.10)}$$

T_e equals the amount of time during which water is flowing (i.e. the bed is not dry) during ebb or flood in a tidal cycle, i.e.:

$$T_{e,c/f} = \frac{T_\omega}{2} \frac{\min\left(2a, d_{c/f}\right)}{2a}. \text{ (Eq. 4.11)}$$

The factor π/2 in Eq. 10 originates from the ratio between the maximum and average water level temporal derivatives, and it is needed in order to evaluate the maximum rather than the tidally averaged velocity.

The current-induced shear stress is then computed from the velocity using the Manning equation:

$$\tau_{cur,c/f} = \frac{\gamma n^2}{h_{c/f}^{1/3}} U_{c/f}{}^2, \text{ (Eq. 4.12)}$$

where γ is the water specific weight.

4.2.4. Comparison with the results of the model Delft3D

The model for the longitudinal and lateral circulation and for the maximum velocities is compared with the hydrodynamic model Delft3D (Lesser et al., 2004), which solves numerically the depth-averaged shallow water equations.

The Delft3D model is applied to a simple geometry (Fig. 4.1E), which reproduces the geometry used in the morphological model: a rectangular channel with depth d_c, bounded by a tidal flat with elevation d_f. A buffer area of 2 km length is introduced in the seaward region, to reduce the effect of boundary conditions on partially wet areas (i.e., the tidal flats). A sinusoidal water level is imposed on the channel seaward end, while a no flux condition is imposed on the tidal flat seaward end, simulating the presence of a barrier island. Friction is computed using the Manning equation, with a coefficient n= 0.016 $m^{1/3}/s$, which is equivalent to a drag coefficient of ~0.0025, often used in muddy environments (Whitehouse et al., 2000). Horizontal eddy viscosity is computed with the large eddy simulation technique. Simulations are performed considering a single domain length, L = 8km, a single total width, B = 1.2 km, changing the ratio between channel and tidal flat width, b_c/B, and channel and tidal flat depths.

The ebb-flood symmetrical volumes exchanged along the longitudinal and transversal directions are computed from the results of the Delft3D model as:

$$V_c^{Delft3D} = \frac{1}{2}\int_0^{T_\omega}\left|\int_{y=0}^{y=bc} U_x(x=L,y,t)dy\right|dt$$

$$V_f^{Delft3D} = \frac{1}{2}\int_0^{T_\omega}\left|\int_{y=bc}^{y=bc+bf} U_x(x=L,y,t)dy\right|dt\,, \qquad \text{(Eq. 4.13)}$$

$$V_{lat}^{Delft3D} = \frac{1}{2}\int_0^{T_\omega}\left|\int_{x=0}^{x=L} U_y(x,y=b_c,t)dx\right|dt$$

where U_x and U_y are the velocities computed with the Delft3D model. The maximum tidal velocities are calculated as the average of the maximum ebb and flood velocity, U_x, at the terminal cross section, x=L.

The results of Delft3D and the simplified model are in good agreement (Fig. 4.3). Both models predict that the maximum lateral exchange generally occurs when the tidal flat elevation is at the LW level ($d_f/2a$=1 in Fig. 4.3A). When the tidal flats are above LW, the tidal prism is smaller than the maximum one (Eq. 4.4). When tidal flats are deeper than LW, the tidal prism remains constant, but the difference in water depth between channel and tidal flat and hence the flow repartition is reduced (Eq. 4.8).

The simplified model generally captures the maximum velocity simulated by Delft3D (Fig. 4.3B). In particular, the model reproduces the velocity increase in the channel and corresponding velocity decrease in the tidal flat when the water depth in the tidal flat decreases. This velocity increase in the channel is caused by the tidal flat mass storage effect, which has been extensively investigated (Dronkers, 1986). The decrease of velocity on the tidal flat is instead caused by the channel drainage effect. This process is not captured by one-dimensional models of tidal flat evolution (Le Hir et al., 2000;

Roberts et al, 2000; Pritchard et al, 2002; Pritchard and Hogg, 2003; Mariotti and Fagherazzi, 2010).

In addition to the simplified geometry with a constant channel depth, the same Delft3D simulations are performed using a more realistic domain, characterized by a linear sloping channel, with depth equal to d_c at the seaward edge and equal to the minimum between LW and d_f at the landward edge. This modification affects the velocity distribution along the channel, but does not significantly change the flow repartition between channel and tidal flat. Also in the linear sloping scenario the maximum lateral exchange occurs for tidal flat elevation at LW and the velocity in the channel is always greater than on the tidal flat (Fig A1). Because here we focus on the gross flow repartition between channel and tidal flat and their reference velocities rather than on the detailed velocity distribution along the channel (needed instead for the morphological evolution of the channel profile, see Lanzoni and Seminara, 2002; Seminara et al., 2009), this result supports the use of our simple schematization.

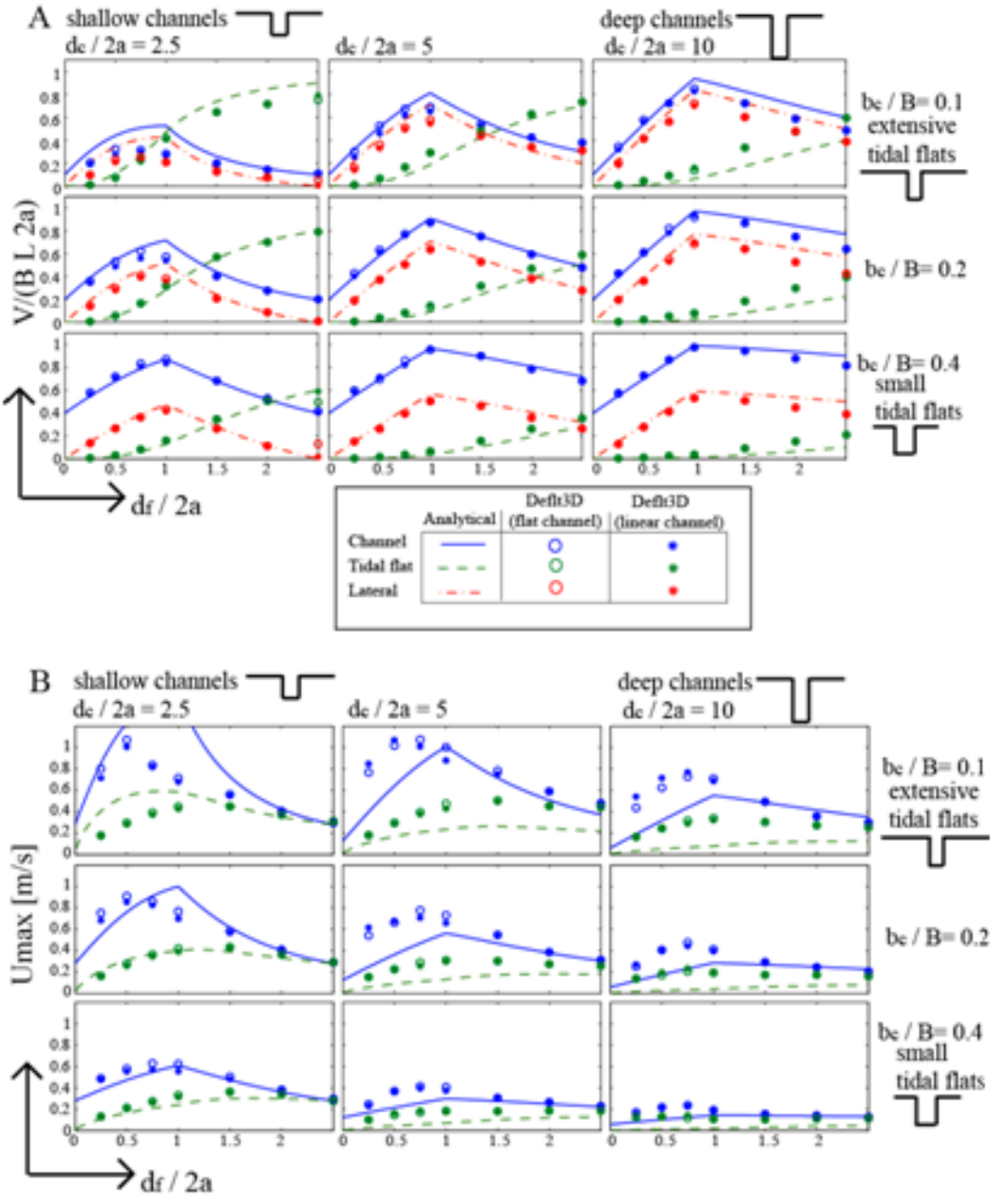

Figure 4.3: A) Normalized exchanged volumes (channel, tidal flat, and lateral, Eqs. 8,9), and B) maximum tidal velocity (channel and tidal flat), as a function of the nondimensional geometric parameters: b_c/B, $d_c/2a$ and $d_f/2a$. Lines are the results of our analytical model, dots are the Delft3D results with L=8km, n=0.016 $m^{1/3}/s$, a=0.5 m (empty circles for a flat channel, stars for a linearly sloping channel).

4.2.5. Wave shear stress

Locally-generated surface wind waves are reproduced with a simplified method. Significant wave height, H_s, and peak period, T_p, are computed using the semi-empirical relationships of Young and Veraghen (1996):

$$g^2 \frac{H_s^2}{16} U_{wind} = 3.64 \cdot 10^{-3} \left\{ \tanh A_1 \tanh \left[\frac{B_1}{\tanh A_1} \right] \right\}^{1.74}$$
$$\frac{1}{gT_p} U_{wind} = 0.133 \left\{ \tanh A_2 \tanh \left[\frac{B_2}{\tanh A_2} \right] \right\}^{-0.37} \quad \text{, (Eq. 4.14)}$$

with A_1=0.493$(gd/U_{wind})^{0.75}$, B_1=3.13 $10^{-3}(gd/U_{wind})^{0.57}$, A_2=0.331 $(g\,\chi\,/U_{wind})^{1.01}$, B_2=5.215 $10^{-4}(g\,\chi\,/U_{wind})^{0.73}$, where χ is the fetch and U_{wind} is the reference wind speed.

Mariotti and Fagherazzi (2012a) showed that the presence of channels marginally affects the wave regime on tidal flats. Therefore, the tidal flat effective depth, h_f, is taken as a reference to compute the wave regime (H_s, T_p) over the whole domain, neglecting the presence of channels. Fetch is assumed to be equal to the basin length, and wind speed is considered a control parameter. The wave-induced shear stress τ_w is then computed as:

$$\tau_{w,c/f} = \frac{1}{2} \rho f_w \left(\frac{\pi H_s}{T_p \sinh\left(k h_{c/f}\right)} \right)^2 \quad \text{, (Eq. 4.15)}$$

where f_w is a friction factor, and k is the wave number, derived from the dispersion relationship. Because of the greater water depth, wave shear stresses are lower in the

channel than on the tidal flat. These semi-empirical equations (Eq. 4.14,4.15) produce a non-monotonic relationship between bed shear stress and water depth (Fagherazzi et al., 2006), which is function of both wind speed and fetch (Mariotti and Fagherazzi, 2012a). For a fixed fetch and wind speed, we refer to the maximum wave shear stress over all the possible depths as $\tau_{w,max}$.

Name	**Meaning**	**Value**	**Reference**
$2a$	Tidal range	2 m	Fixed by the authors
λ_{cur} , λ_w	Frequency factor for currents and waves	1	
N	Manning coefficient	0.016 $m^{1/3}/s$	
T_ω	Period of the diurnal tide	12.5 hr	
w_s	Settling velocity	0.5 mm/s	
τ_{cr}	Critical shear stress	0.1Pa	
L	Longitudinal length	5 km	
ρ_s	Apparent sediment density	1800 kg/m^3	
b_c/B	Channel width/ total width	0.1-0.4	Varied
U_{wind}	Wind speed	0-15 m/s	Parametrically
E_o	Net exogenous erosion	-15 to 15 mm/yr	
m_e	Erosion coefficient	10^{-4} $kg/(m^2s)$	Whitehouse et al. (2000)

Name	Meaning	Value	Reference
f_w	Wave friction coefficient	0.015	Collins (1972)

Table 4.1: Model parameters.

4.3 Model results

The simplified model is studied fixing the wave friction coefficient, f_w, the Manning's coefficient, n, the erosion parameter, m_e, the settling velocity, w_s, the critical shear stress, τ_{cr}, the tidal amplitude, a, and the basin length, L (Table 4.1). We therefore explore the model sensitivity to the following parameters: b_c/B, C_o, E_o, and U_{wind}. b_c/B describes the geometry of the channel compared to the tidal basin. C_o is a proxy for external sediment availability, which is affected by long-shore sediment transport and inlet evolution (Tambroni and Seminara, 2006). E_o represents the combined effect of RSLR and sediment inputs from rivers or erosion of salt marshes. U_{wind} quantifies the role of wind waves on tidal flat evolution.

4.3.1. Case without relative sea level rise or sediment inputs in the basin (Eo=0)

We first consider the case with E_o = 0, i.e. with no RSLR or internal sediment inputs. The system admits only one equilibrium solution, C_c=C_f=C_o, in which the reference concentration is the same in the channel and tidal flats, and it is equal to the seaward boundary concentration. In order to maintain this equilibrium, the shear stress in both channel and tidal flat is such that $C(\tau_{eq(w)}, \tau_{eq(cur)})$=$C_o$:

$$\lambda_w \max\left(\tau_{eq(w)} - \tau_{cr}, 0\right) + \lambda_{cur} \max\left(\tau_{eq(cur)} - \tau_{cr}, 0\right) + \tau_{cr} = \tau_{eq} = C_o \frac{\tau_{cr} w_s}{m_e} + \tau_{cr} \text{ . (Eq. 4.16)}$$

The solution further depends on whether we consider only tidal currents or both currents and waves, as discussed below.

4.3.1.1. Tidal currents

When only currents are present, an analytical treatment of the solution is possible. If the channel is deeper than the tidal flat, the current induced bed shear stress and the reference concentration are higher in the channel. As a result, the system admits only trivial equilibria, which correspond to Q_{lat} equal to zero. This condition is met in two simple configurations: tidal flat depth equal to zero or tidal flat depth equal to channel depth. The first scenario is interpreted as a tidal creek in which the surrounding salt marshes have an elevation equal to HW and do not contribute to the tidal prism (tidal creek case, P_c). The second scenario is interpreted as a tidal flat without channels (tidal sound case, P_s). In absence of waves, the equilibrium shear stress is associated to the following equilibrium depth:

$$d_{cur} = a + \left[\rho g n^2 \left(\frac{L 2a}{T_\omega / 2} \frac{\pi}{2} \right)^2 \tau_{eq}^{-1} \right]^{3/7} \text{ , (Eq. 4.17)}$$

which is valid if $d_{cur} > 2a$, i.e. the depth of the channel is lower than LW.

The equilibrium point P_c (tidal creek) is stable: an increase in channel depth decreases the bed shear stress and the sediment concentration in the channel promoting infilling,

while a decrease in channel depth increases its sediment concentration promoting scouring (Fig. 4.4). The equilibrium point P_s (unchannalized sound) is instead unstable. A channel slightly deeper than the surrounding tidal flat starts draining water, thus increasing the current shear stress in the channel and decreasing it on the tidal flat. This condition creates a gradient of sediment concentration from the channel to the tidal flat, which, combined to the water exchange between the two elements (Q_{lat}), determines a flux of sediment toward the tidal flat. This flux tends to fill the tidal flat, increasing the relative channel depth, thus creating a morphological positive feedback that constitutes the basic mechanism for channel formation (Fagherazzi and Furbish, 2001). Indeed, this process is the channel spillover mechanism described by Mariotti and Fagherazzi (2012b).

The union of the points with channel depth equal to the tidal flat depth constitutes the stable manifold of the unstable point P_s (Fig. 4.4, 1:1 line), which hence results to be a saddle. An unstable manifold connects the unstable equilibrium P_s to the stable equilibrium P_c. The time needed to move from a neighborhood of P_s to a neighborhood of P_c is on the order of 100 years (Fig. 4.4). Interestingly, the points on this manifold experience channel depths greater than the equilibrium value, as found also by D'Alpaos et al. (2006).

Changing the relative channel width b_c/B does not affect the equilibrium depth d_{cur} (Fig. 4.4, Eq. 4.17). However, the lower the relative channel width, the higher is the maximum channel depth experienced by the manifold connecting P_s to P_c. Changing the

model parameters (L, a, τ_{cr}) affects both the equilibrium points (Eq. 4.17) and the manifold, but does not affect the qualitative bifurcation portrait.

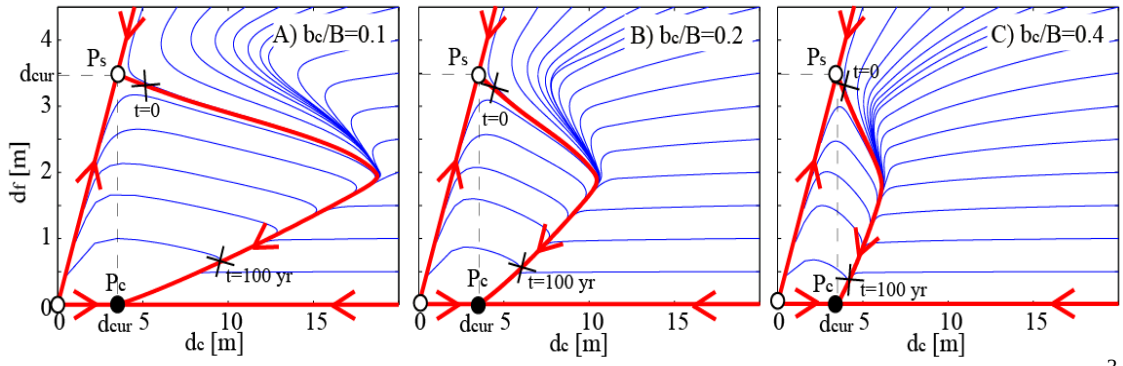

Figure 4.4**:** Phase space plot of channel and tidal flat depths, with a=1m, C_o=0.1 kg/m^3, E_o=0, L=5km, τ_{cr}=0.1 Pa, U_{wind}=0. The normalized channel width b_c/B is varied. The stable (solid circles) and unstable points (empty circles), manifolds (red lines), and some indicative trajectories (blue lines) are reported. An unstable manifold connect the unstable point P_s to the stable point P_c. The two X symbols on the manifold are spaced by 100 years. The dashed line indicates the equilibrium depth d_{cur} (Eq. 4.17).

4.3.1.2. Tidal currents and waves

Wind waves induce high shear stresses on tidal flats, triggering a complex dynamics. We find that the system experiences four distinct regimes when we increase the wind speed: current dominated, mixed, weakly wave dominated, and strongly wave dominated (Fig. 4.5).

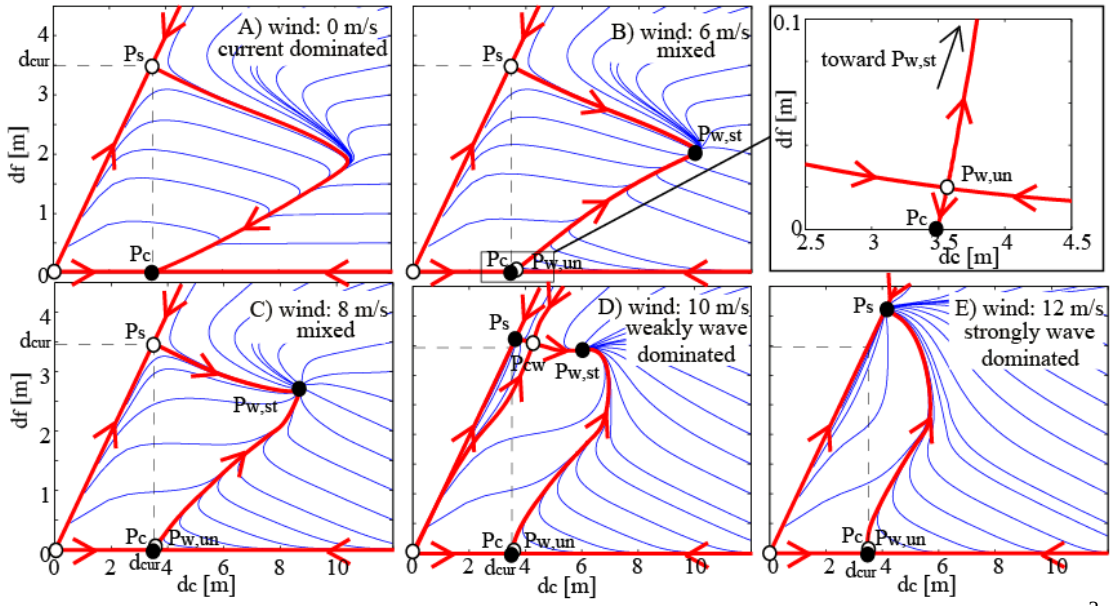

Figure 4.5: Phase space plot of channel and tidal flat depth, with a=1m, C_o=0.1 kg/m^3, E_o=0, L=5km, τ_{cr}=0.1 Pa, b_c/B=*0.2*. Wind speed is varied from 0 to 12 m/s. The stable (solid circles) and unstable points (empty circles), manifolds (red lines), and some indicative trajectories (blue lines) are reported. The dashed lines indicate the equilibrium depth d_{cur} (Eq. 4.17). A) Current dominated regime: only two trivial equilibria are present. B,C) Mixed regime: the stable equilibrium $P_{w,st}$ dominates the phase space. The inset shows a detail of the unstable equilibrium $P_{w,un}$, which almost overlaps P_c. D,E) Wave dominated regimes: the equilibrium point P_s is no more equal to d_{cur} and it is now stable.E) In the strongly wave dominated regime the equilibrium point $P_{w,st}$ disappears.

The current dominated regime occurs for low wind velocities, such that $\tau_{w,max}<\tau_{eq}$ (Fig. 4.5A). In this regime the equilibrium points are those due to tidal currents only (P_s and P_c, Eq. 4.17). In these conditions, the higher sediment concentration in the channel tends to fill the tidal flats, despite τ_w on the tidal flats is greater than τ_{cr}. Some trajectories are slightly different from the case without waves, but the overall phase space portrait remains unchanged.

The mixed regime occurs for wind velocity such that $\tau_{w,max}>\tau_{eq}$ (Fig. 4.5B,C). In this regime a bifurcation occurs and two non-trivial equilibria appear, $P_{w,st}$ and $P_{w,un}$, leaving unvaried the current dominated equilibria P_c and P_s. The new equilibria are such that $\tau_{cur,c}= \tau_{w,f}=\tau_{eq}$, i.e. the equilibrium concentrations are determined by currents in the channel and by waves on the tidal flat (Fig. 4.6A,B,E,F). The presence of two equilibria $P_{w,st}$ and $P_{w,un}$ stems from the fact that there are two depths on the tidal flat capable of generating the same wave shear stress, as showed by Fagherazzi et al. (2006) (Eq. 4.14,4.15). The unstable equilibrium $P_{w,un}$ lays on the rising limb of the τ_w-d_f curve, while the stable equilibrium $P_{w,st}$ lays on the decreasing limb on the curve (Fig. 4.6A,E).

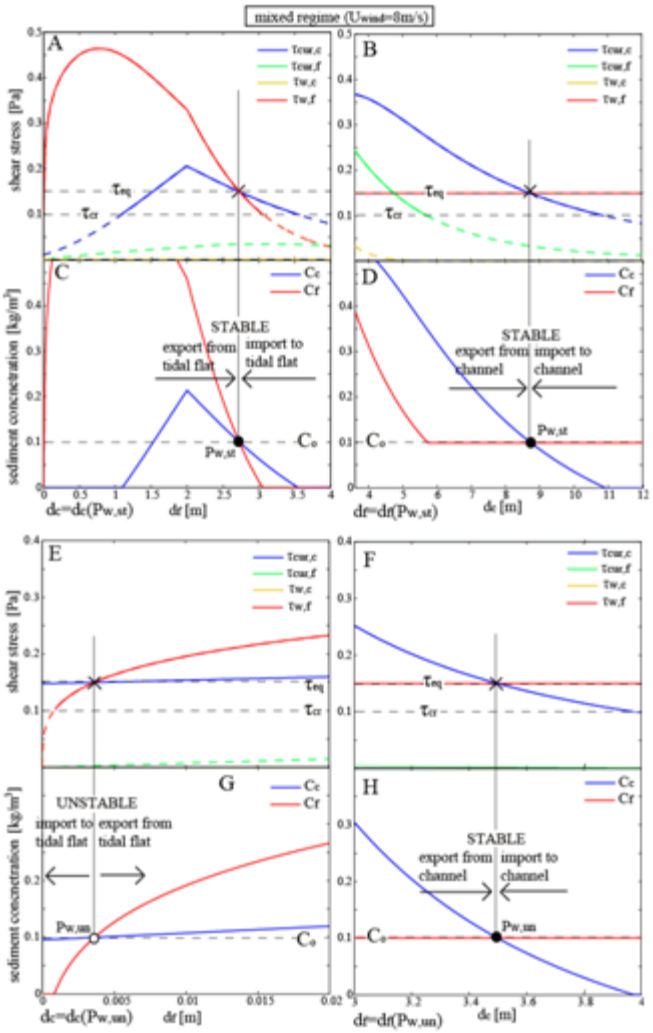

Figure 4.6: Example of mixed regime (U_{wind}=8 m/s, as in Fig. 4.5C). A) Shear stresses and C) sediment concentration, as function of d_f, for a fixed value of d_c, equal to $d_c(P_{w,st})$. Only $\tau_{cur,c}$ and $\tau_{w,f}$ contribute to the reference sediment concentration, because both $\tau_{cur,f}$ and $\tau_{w,c}$ (green and yellow dashed lines) are below τ_{cr}. The point $P_{w,st}$ is stable with respect to variations in tidal flat depth: if the tidal flat becomes shallower than $d_f(P_{w,st})$, C_f becomes greater than C_c and $C_{o,}$ establishing sediment fluxes toward the channel and the open sea. B) Shear stresses and D) sediment concentration, as function of d_c, for a fixed value of d_f, equal to $d_f(P_{w,st})$. The point $P_{w,st}$ is stable with respect to variations in channel depth: if the channel becomes shallower than $d_c(P_{w,st})$, C_c becomes greater than C_f and C_o, establishing sediment fluxes toward the tidal flat and the open sea. E) Shear stresses and G) sediment concentration, as function of d_f, for a fixed value of d_c, equal to $d_c(P_{w,un})$. Only $\tau_{cur,c}$ and $\tau_{w,f}$ contribute to the reference sediment concentration, because both $\tau_{cur,f}$ and $\tau_{w,c}$ (green and yellow dashed lines) are below τ_{cr}. The point $P_{w,un}$ is unstable with respect to variations in tidal flat depth: if the tidal flat

becomes shallower than $d_f(P_{w,un})$, C_f becomes smaller than C_c and C_o, establishing sediment fluxes toward the tidal flat. F) Shear stresses and H) sediment concentration, as function of d_c, for a fixed value of d_f, equal to $d_f(P_{w,un})$. The point $P_{w,un}$ is stable with respect to variations in channel depth: if the channel becomes shallower than $d_c(P_{w,un})$, C_c becomes greater than C_f and C_o, establishing sediment fluxes toward the tidal flat.

The stability of the equilibrium $P_{w,st}$ is revealed by the shear stress and sediment concentration modulations associated to variations in channel and tidal flat depth. If the tidal flat becomes shallower than $d_f(P_{w,st})$, C_f becomes greater than C_c and C_o, leading to sediment concentration gradients and fluxes toward the channel and the open sea, while the opposite gradients are established if the tidal flat becomes deeper than $d_f(P_{w,st})$ (Fig. 4.6C). Analogously, if the channel becomes shallower than $d_c(P_{w,st})$, C_c becomes greater than C_f and C_o, leading to concentration gradients toward the tidal flat and the open sea, while the opposite gradients are established if the channel becomes deeper than $d_c(P_{w,st})$ (Fig. 4.6D).

The equilibrium $P_{w,un}$ is unstable with respect to variations in tidal flat depth: if the tidal flat becomes shallower than $d_f(P_{w,un})$, C_f becomes smaller than C_c and C_o(Fig. 4.6D), leading to a concentration gradient toward the tidal flat, while the opposite gradient is established if the tidal flat becomes deeper than $d_f(P_{cw})$ (Fig. 4.6E,G). Because $P_{w,un}$ is stable with respect to variations in channel depth (Fig. 4.6F,H), this point is a saddle. One limb of the unstable manifold of $P_{w,un}$ connects the saddle to P_c, while the other limb connects the saddle to $P_{w,st}$ (Fig. 4.5B,C). Because the depth associated to $P_{w,un}$ is very small (<0.2 m for wind speed between 0 and 12 m/s), the basin of attraction of the stable point P_c is small, and the phase space is dominated by the new equilibrium point $P_{w,st}$.

The two wave dominated regimes occur for wind speeds such that $\tau_w(d_{cur})>\tau_{cr}$, i.e. the wave shear stress is capable of resuspending sediment at the current dominated equilibrium d_{cur} (4.5D,E). In these regimes the equilibrium point P_s is still characterized by channel and tidal flat with same depth, but now both currents and wave shear stresses contribute to τ_{eq}, and hence the depth of P_s is no more equal to d_{cur} (Eq. 4.17). This equilibrium becomes stable, being controlled by the wave shear stress, which decreases for increasing depths.

In the weakly wave dominated regime the stable equilibrium $P_{w,st}$ persists, and τ_{eq} remains determined by currents in the channel and by waves on the tidal flat (Fig. 4.5D). An additional equilibrium appears, P_{cw}, such that the reference concentration on the tidal flat is determined by a combination of currents and waves (Fig. 4.7A,B). Analogously to the equilibrium $P_{w,st}$, P_{cw} is stable with respect to variations of tidal flat depth (confront Fig. 4.7C with 4.6C). On the other hand, P_{cw} is unstable with respect to variations of channel depth: if the channel becomes shallower than $d_c(P_{cw})$, C_c becomes smaller than C_f and C_o (Fig. 4.7D), leading to concentration gradients toward the channel, while gradients from the channel are established if this becomes deeper than $d_c(P_{cw})$. Contrary to the point $P_{w,un}$, the instability of P_{cw} is dictated by the behavior of the current shear stress on the tidal flat (Fig. 4.7B). As for P_s and $P_{w,un}$, also P_{cw} is a saddle, with one stable and one unstable manifold (Fig. 4.5D). One limb of the unstable manifold connects P_{cw} to $P_{w,st}$, which it is associated to a shallower tidal flat, while the other limb of the unstable manifold connects P_{cw} to P_s, which it is associated to a deeper tidal flat.

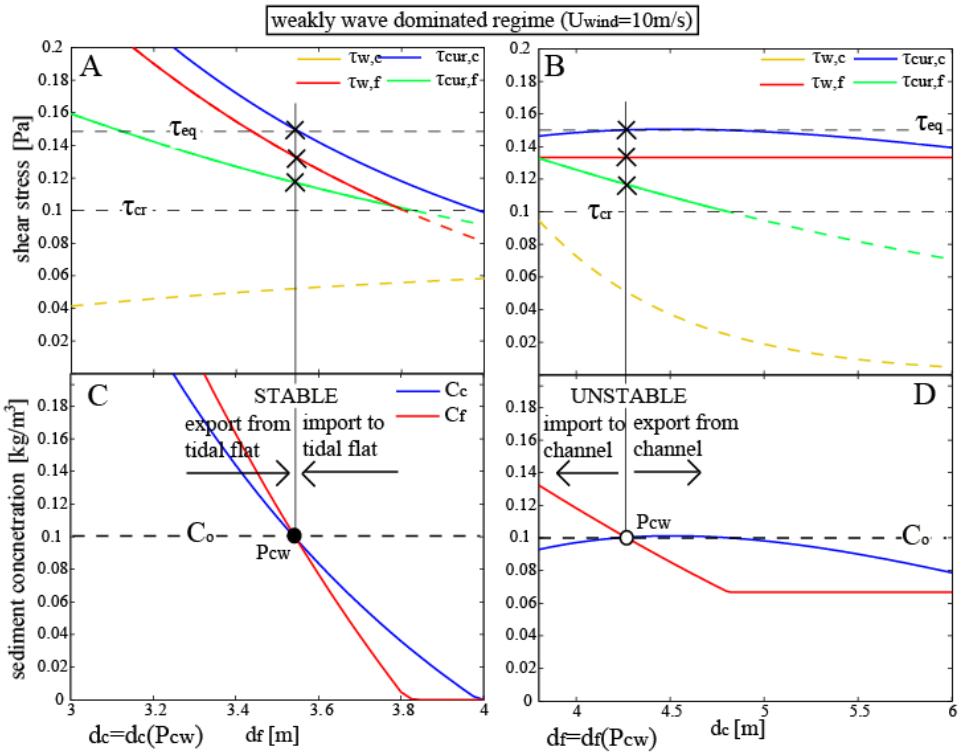

Figure 4.7: Example of weakly wave dominated regime (U_{wind}=10 m/s, as in Fig. 4.5D): in addition to the points $P_{w,st}$ and $P_{w,un,}$ the non-trivial equilibrium P_{cw} is present. A) Shear stresses and C) sediment concentration, as function of d_f, for a fixed value of d_c, equal to $d_c(P_{cw})$. Both $\tau_{w,f}$ and $\tau_{cur,f}$ contribute to the reference sediment concentration on the tidal flat (note that they are both greater than τ_{cr}). The point P_{cw} is stable with respect to variations in tidal flat depth: if the tidal flat becomes shallower than $d_f(P_{cw})$, C_f becomes greater than C_c and C_o, establishing sediment fluxes toward the channel and the open sea. B) Shear stresses and D) sediment concentration, as function of d_c, for a fixed value of d_f, equal to $d_f(P_{cw})$. The point $P_{w,st}$ is unstable with respect to variations in channel depth: if the channel becomes shallower than $d_c(P_{cw})$, C_c becomes smaller than C_f and C_o, establishing sediment fluxes toward the channel.

The strongly wave dominated regime occurs for wind speeds such that the current shear stress on tidal flat associated to $P_{w,st}$ is greater than τ_{cr} (Fig. 4.5E). In this scenario it is no more possible to keep both the wave and the current shear stress on the tidal flat equal or below the equilibrium shear stress, $P_{w,st}$ and P_{cw} disappear, and P_s becomes the only stable equilibrium point.

In summary, the stable point with the largest basin of attraction is P_c for the current dominated regime, $P_{w,st}$ for the mixed and the weakly wave dominated regime, and P_s for the strongly wave dominated regime. The bifurcation diagram as a function of wind speed is showed in Figure 8A, reporting the coordinate of the stable point with the largest basin of attraction.

Figure 8A is also showing the influence of the boundary condition C_o. If more sediments are available at the open sea, then a higher shear stress is needed to balance the input. As a result, a higher C_o decreases the equilibrium depth of P_s, $P_{w,st}$ and P_c.

4.3.2. Relative sea level rise and sediment inputs in the basin ($E_o \neq 0$)

When E_o is different from zero, the model needs a net sediment import when sea level is rising, (E_o>0), or export when large quantities of sediments are discharged in the basin (E_o<0) in order to maintain its morphological equilibrium. In these scenarios the trivial equilibrium P_s persists (Fig. 4.9), and stems from a balance between the longitudinal sediment input-export and the internal gain-loss of sediments:

$Q_c\left(C_c - C_o\right)/b_c = Q_f\left(C_f - C_o\right)/b_f = -E_o L\rho_s$. Without waves, the equilibrium depth of this equilibrium reads:

$$d_{cur,Eo} = a + \left[\rho g n^2 \left(\frac{L2a}{T_\omega/2}\frac{\pi}{2}\right)^2 \left(\left(-\frac{T_\omega \rho_s E_o}{2a} + C_o\right)\frac{\tau_{cr} w_s}{m_e} + \tau_{cr}\right)^{-1}\right]^{3/7}, \text{(Eq. 4.18)}$$

which is valid for both E_o> and E_o <0. For RSLR on the order of 10 mm/yr, the relative difference between this equilibrium and that resulting from Eq. 4.17 (E_o=0) is less than 10^{-2} (compare the position of P_s in Fig. 4.9 for different values of E_o).

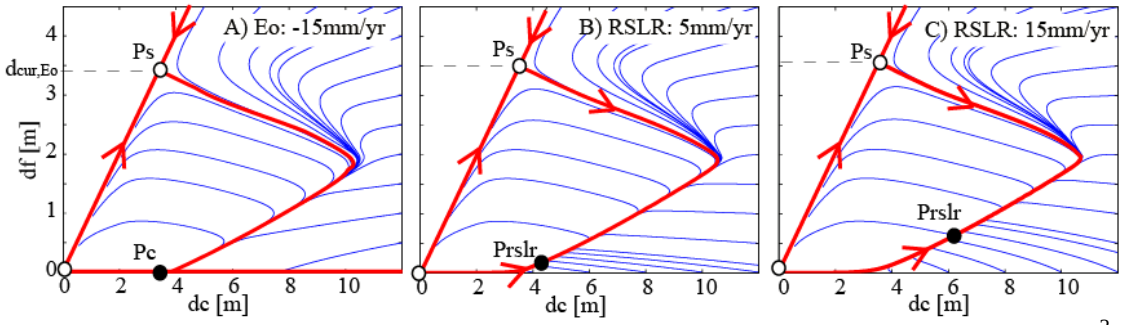

Figure 4.8: Phase space plot of channel and tidal flat depth, with a=1m, C_o=0.1 kg/m^3, L=5km, τ_{cr}=0.1 Pa, b_c/B=0.2, U_{wind}=0, and different values of E_o. For E_o<0 (internal sediment input), the equilibria remain almost unvaried respect to the case with E_o=0. For E_o>0 (RLSR), the stable equilibrium become P_{rslr}, which is not trivial. In both cases, the trivial unstable equilibrium P_s is given by Eq. 4.18.

For very high values of E_o (high RSLR) the system is not able to import enough sediments to maintain a dynamical equilibrium, even reducing the concentration in the channel and tidal flat to zero. This pivoting condition occurs when E_o is greater than the maximum rate of sediment input per unit of area, i.e. $E_o > \frac{2aC_o}{T_\omega \rho_s}$. In this condition the equilibrium expressed by Eq. 4.18 does not hold and the basin drowns. For the parameters selected herein (see Table 1) the drowning occurs for E_o greater than ~78

mm/yr, which is not found in any natural system. Therefore this scenario will not be further considered.

For E_o >0, the trivial equilibrium P_c becomes the non-trivial equilibrium P_{rslr}, characterized by a deep channel and a shallow tidal flat (Fig. 4.9B,C). In this equilibrium $C_o>C_c>C_f$, and hence sediments are transported from the open sea to the channel and form the channel to the tidal flat. Instead, for E_o <0 (exogenous sediment input), the equilibrium point is still characterized by flats at HW.

Wind waves create four regimes also in presence of RSLR, which are qualitatively equivalent to the case with $E_o=0$ (Fig. 4.8B). In the current dominated regime the only stable point is P_{rslr} for $E_o>0$ and P_c for $E_o<0$. For both the mixed and weakly wave dominated regimes the stable point with the largest basin of attraction remains $P_{w,st}$, whose coordinates are only slightly affected by the presence of E_o (increasing value of E_o increases the equilibrium depths of both channel and tidal flat). Finally, in the strongly wave dominated regime, the equilibrium P_s is almost identical to the case with E_o =0.

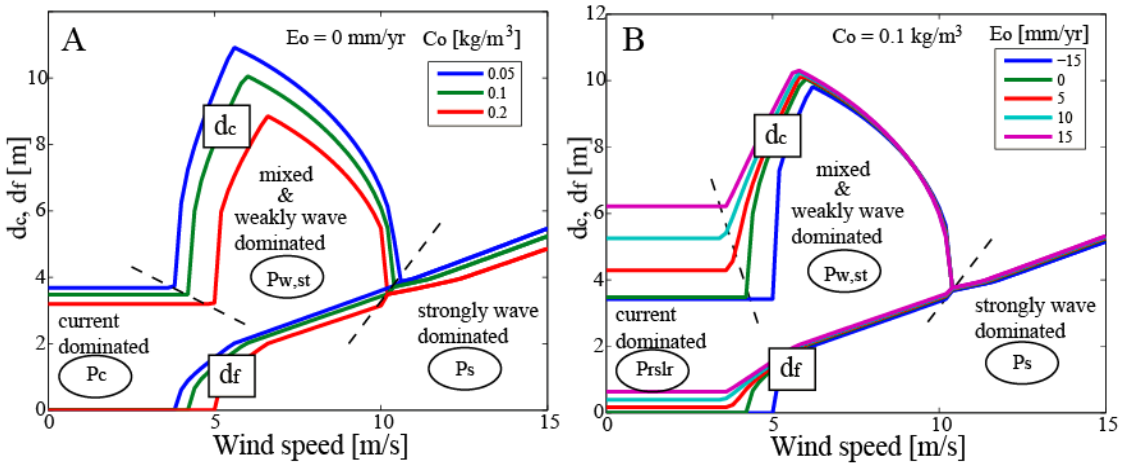

Figure 4.9: A) Stable equilibrium with the largest basin of attraction, (P_c, $P_{w,st}$, or P_s), as function of wind speed, for different C_o and E_o=0. B) Stable equilibrium with the largest basin of attraction, (P_{rslr}, $P_{w,st}$, or P_s), as function of wind speed, for different E_o. For $E_o>0$ (RSLR) the stable equilibrium in the current dominated regime become non-trivial. a=1m, C_o=0.1 kg/m^3, L=5km, τ_{cr}=0.1 Pa, $b_c/B=0.2$.

4.4. Discussion

4.4.1. Is the model a good description of tidal basins?

The choice of only two dynamical variables and the schematization of the tidal dispersion fluxes in three components, Q_c, Q_f and Q_{lat}, allow the construction of a reduced complexity model which admits some analytical treatments. Clearly many processes are neglected in the model, such as ebb-flood asymmetry, spatial variability in the channel and tidal flat, spring-neap modulation, intermittency of wind events, seasonal effects. Neglecting these processes limits the applicability of the model, but allows to systematically explore the coupled dynamics of currents and waves that have been previously ignored.

The proposed model exploits the full potential of dynamical systems analysis, based on equilibrium points, stability, and bifurcations (Phillips, 1992), featuring flow patterns more articulated than those assumed in zero-dimensional dynamical models (e.g., Fagherazzi et al., 2006; Marani et al., 2010). The good agreement with the full hydrodynamic model Delft3D suggests than these flow patterns are realistic.

The assumption that a single current shear stress is sufficient to characterize channel and tidal flat hydrodynamics is questionable. In fact, real flow fields in tidal basins are not uniform in space, especially near the landward boundaries. However, several studied showed that both channel (Friedrichs, 1995) and tidal flat (Friedrichs and Aubrey, 1996; Pritchard et al., 2002) adjust their profile toward a spatially uniform shear stress, suggesting that a single shear stress might be an appropriate choice for long-term modeling purposes.

Our simple model reproduces the transfer of flow from tidal flats to the channel, which constitutes the main hydrodynamic interaction between these two landforms (Fagherazzi and Furbish, 2001). As a result, the current shear stresses on the tidal flat marginally participate to the morphological evolution of the system, and the dynamics is overall driven by currents in the channel and waves on the tidal flat, in accordance with field observations (Allen and Duffy, 1998; Ridderinkof, 2000; Mariotti and Fagherazzi, 2012b).

Finally, we intentionally limited the analysis of the model to a restricted number of parameters, focusing on the bifurcations induced by wave climate and RSLR. The

model could be further explored evaluating different combinations of basin length, tidal range, and critical shear stress.

4.4.2. Model predictions: modulation by wind waves

Without waves and RLSR, the model predicts only trivial equilibria. The unchannalized configuration is unstable, thus capturing the autogenic channelization driven by flow concentration in deeper areas (Eq. 4.8, see also Fagherazzi and Furbish, 2001). Interestingly, the model predicts transient configurations in which the channel initially deepens and then becomes shallower while moving from the unchannalized to the channelized stable equilibrium (D'Alpaos et al., 2006). This behavior cannot be predicted by static models that consider only equilibrium states.

In the mixed regime waves trigger the presence of a non-trivial equilibrium, $P_{w,st}$, with a deep channel and a shallow tidal flat. This equilibrium occurs for wind speeds such that the maximum wave shear stress is greater than τ_{eq}, which is higher than τ_{cr}. In other words, the wave regime needs to be strong enough to overcome the channel dominance. In this equilibrium the reference concentration is maintained by currents in the channel and by waves on the tidal flat. This corresponds to the observation that sediment concentrations are higher in the channel during fair weather (Ridderinkof, 2000; Janssen-Stelder, 2000), and on tidal flats during storms (Dyer et al., 2000; Christiansen et al., 2006). In natural systems the peak concentrations switch between channel and tidal flats depending on wind conditions, while in the model the peak concentrations

occurs simultaneously. Therefore the model should be considered as an average over a characteristic time scale that includes many storms.

While in the mixed regime the concentration on the tidal flat is exclusively controlled by waves, in the weakly wave dominated regime currents contribute to the tidal flat concentration too. This condition allow for the presence of an additional non-trivial equilibrium, P_{wc}. Because this new equilibrium is very close to the point P_c (see Fig. 4.5D), the mixed and the weakly wave dominated regimes can be considered as a single regime, in which the stable point $P_{w,st}$ dominates the dynamics.

Except for the origin, all the unstable points are saddles. Interestingly, the two non-trivial saddles, $P_{w,un}$ and P_{cw}, show a different type of instability: the former is unstable with respect to variations in tidal flat depth, while the latter is unstable with respect to variations in channel depth. Further studies are sought to investigate whether this difference has a geomorphological footprint.

Finally, in the strongly wave dominated regime it is not possible to have equilibrium between a wave dominated tidal flat and a current dominated channel. In this regime waves are strong enough to suppress the formation and persistence of channels, and the flat, unchannalized configuration becomes the only stable equilibrium.

4.4.3. Relative sea level rise (RLSR)

The presence of RLSR allows the system to have non trivial equilibria without the presence of wind waves. Of particular interest is the stable point P_{rslr}, characterized by a

deep channel (d_c>2a) and by a shallow tidal flat (d_f <0.5 m for RLSR of 0-10 mm/yr). Differently from the equilibrium associated with E_o=0, in this scenario a net sediment flux from the open ocean to the channel and from the channel to the tidal flats is present.

4.5. Conclusions

We propose a novel morphological model for the coupled evolution of channels and tidal flats. The model features few fundamental processes: flow repartition between channel and tidal flat and a non monotonic relationship between wave shear stresses and depth. The model uses a simplified hydrodynamic approach, validated with the full Delft3D model applied to a schematic geometry.

According to the model, wind speed is a crucial parameter determining the system dynamics. For low wind speeds, only a trivial stable point is possible, corresponding to a channel without tidal flats. The flat, unchannalized equilibrium configuration is unstable, suggesting that the model captures the morphological instability leading to channel formation.

For intermediate wind speeds, a non-trivial stable equilibrium point with a deep channel and a relatively shallow tidal flat appears. In this scenario, the equilibrium concentration is determined by currents in the channel and by waves on the tidal flats. This equilibrium is likely to represent real tidal flats, in which both wind waves and tidal

currents are relevant. Two additional non-trivial unstable equilibria are present, which affect only a small portion of the phase space.

For elevated wind speeds, the unchannalized basin is the only stable point. In this scenario, waves suppress the instability which leads to channel incision. Further studies are required to explore how the competition between tidal currents and wind waves is affected by other parameters such as basin geometry and tidal amplitude.

Finally, the presence of RLSR allows the system to have a non trivial equilibrium without the presence of wind waves. This equilibrium could be interpreted as a tidal creek bounded by salt marshes, on which resuspension is negligible and inorganic sediments are fed from the channel.

4.6. References

Allen, J.R.L., and Duffy M.J, (1998), Medium-term sedimentation on high intertidal mudflats and salt marshes in the Severn Estuary, SW Britain: the role of wind and tide, Marine Geology, 150, 1–27.

Boon, J.D., (1975), Tidal discharge asymmetry in a salt marsh drainage system, Limnology and Oceanography, 20, 71–80.

Christiansen, C., G. Volund, L.C. Lund-Hansen, and J. Bartholdy, (2006), Wind influence on tidal flat sediment dynamics: Field investigations in the Ho Bugt, Danish Wadden Sea, Marine Geology, 235, 1-4, 75-86.

Collins, J.I., (1972), Prediction of shallow-water spectra. Journal of Geophysical Research, 77, 2693-2707.

D'Alpaos, A., S. Lanzoni, S.M. Mudd, and S. Fagherazzi, (2006), Modeling the influence of hydroperiod and vegetation on the cross-sectional formation of tidal channels, Estuarine, Coastal and Shelf Science, 69, 3-4, 311-324.

Di Silvio, G., C. Dall'Angelo, D. Bonaldo, and G. Fasolato, (2010), Long-term model of planimetric and bathymetric evolution of a tidal lagoon, Continental Shelf Research 30, 894–903,

Dyer, K.R., M.C. Christie, N. Feates, M.J. Fennessy, M. Pejrup, and W. van der Lee, (2000), An investigation into processes influencing the morphodynamics of an intertidal mudflat, the Dollard estuary, the Netherlands: I. Hydrodynamics and suspended sediment, Estuarine Coastal and Shelf Science, 50, 5, 607-625.

Dronkers, J., (1978), Longitudinal dispersion in shallow well-mixed estuaries, Coastal Engineering Conference, 3, 169.

Dronkers, J., (1986), Tidal asymmetry and estuarine morphology, Netherlands Journal of Sea Research, 20, 2-3, 117-131.

Fagherazzi, S., and D.J. Furbish, (2001), On the shape and widening of salt marsh creeks, Journal Geophysical Research,106, C1 , 991-1005, 2001.

Fagherazzi S., P.L. Wiberg, and A.D. Howard, (2003), Tidal flow field in a small basin, Journal Geophysical Research, 108, 3071.

Fagherazzi, S., L. Carniello, L. D'Alpaos, and A. Defina, (2006), Critical bifurcation of shallow microtidal landforms in tidal flats and salt marshes, Proceedings of the National Academy of Sciences of the United States of America, 103, 8337-8341.

Fagherazzi, S., M. Hannion, and P. D'Odorico, (2008), Geomorphic structure of tidal hydrodynamics in salt marsh creeks, Water Resource Research, 44, W02419, 512.

Fagherazzi, S., and P.L. Wiberg, (2009), Controls on fetch, wind waves and wave-generated shear stresses in a shallow coastal lagoon, Journal of Geophysical Research, 114, F03022.

FitzGerald, D.M., (1996), Geomorphic Variability and Morphologic and Sedimentary Controls on Tidal Inlets, Journal of Coastal Research, 23, 47-71.

Friedrichs, C.T., and D.G. Aubrey, (1988), Non-linear Tidal Distortion in Shallow Well-mixed Estuaries: a Synthesis, Estuarine, Coastal and Shelf Science, 27, 521-545.

Friedrichs, C.T., (1995), Stability shear stress and equilibrium cross-sectional geometry of sheltered tidal channels, Journal of Coastal Research, 11, 1062-1074.

Friedrichs, C.T. and D.G. Aubrey, (1996), Uniform bottom shear stress and equilibrium hypsometry of intertidal flats. In: C. Pattiaratchi (Ed.), Mixing Processes in Estuaries and Coastal Seas. American Geophysical Union, Washington, D.C., 405-429.

Janssen-Stelder, B., (2000), The effect of different hydrodynamic conditions on the morphodynamics of a tidal mudflat in the Dutch Wadden Sea, Continental Shelf Research, 20, 1461-1478.

Lesser, G., J. Roelvink, J. Van Kester, and G. Stelling, (2004), Development and validation of a three-dimensional morphological model, Coastal Engineering, 51, 883–915.

Le Hir, P., W. Roberts, O. Cazaillet, M. Christie, P. Bassoullet, and C. Bacher, (2000), Characterization of intertidal flat hydrodynamics, Continental Shelf Research, 20, 12-13, 1433-1459.

Lanzoni, S., and G. Seminara, (2002), Long term evolution and morphodynamic equilibrium of tidal channels, Journal Geophysical Research, 107, C1, 3001.

Li, C.Y., and J. O'Donnell, (1997), Tidally driven residual circulation in shallow estuaries with lateral depth variation, Journal of Geophysical Research-Oceans, 102, C13, 27915-27929.

Marani, M., A. D'Alpaos, S. Lanzoni, L. Carniello, and A. Rinaldo, (2010), The importance of being coupled: Stable states and catastrophic shifts in tidal biomorphodynamics, Journal Geophysical Research, 115, F04004.

Mariotti, G., and S. Fagherazzi, (2010), A numerical model for the coupled long-term evolution of salt marshes and tidal flats, Journal Geophysical Research 115, F01004.

Mariotti, G., and S. Fagherazzi, (2012a), Wind waves on a mudflat: the influence of fetch and depth on bed shear stresses, Continental Shelf Research, special issue: Tidal Flats.

Mariotti, G., and S. Fagherazzi, (2012b), Channels-tidal flat sediment exchange: The channel spillover mechanism, Journal Geophysical Research, 117, C03032.

Okubo, A., (1973), Effects of shortline irregularities on streamwise dispersion in estuaries and other embayments, Netherlands Journal of Sea Research 6, 1–2, 213–224.

Phillips, J.D., (1992), Nonlinear dynamical systems in geomorphology: revolution or evolution?, Geomorphology, 5 3–5, 219–229.

Pritchard, D., A.J. Hogg, and W. Roberts, (2002), Morphological modelling of intertidal mudflats: the role of cross-shore tidal currents, Continental Shelf Research, 22, 1887–1895.

Pritchard, D., and A. J. Hogg, (2003), Cross-shore sediment transport and the equilibrium morphology of mudflats under tidal currents, Journal Geophysical Research, 108, C10, 3313.

Ridderinkhof, H., R. van der Ham, and W. van der Lee, (2000), Temporal variations in concentration and transport of suspended sediments in a channel-flat system in the Ems-Dollard estuary, Continental Shelf Research, 20, 12-13, 1479-1493.

Roberts, W., P. Le Hir, and R.J.S. Whitehouse, (2000), Investigation using simple mathematical models of the effect of tidal currents and waves on the profile shape of intertidal mudflats Continental Shelf Research 20, 1079-1097.

Seminara, G., S. Lanzoni, N. Tambroni, and M. Toffolon, (2009), How long are tidal channels?, Journal of Fluid Mechanics, 1-16.

Speer, P.E., and D.G. Aubrey, (1985), A Study of Non-linear Tidal Propagation in Shallow Inlet/Estuarine Systems. Part II: Theory, Estuarine, Coastal and Shelf Science, 21, 207-224.

Tambroni, N., and G. Seminara, (2006), Are inlets responsible for the morphological degradation of Venice Lagoon?, Journal Geophysical Research, 111, F03013.

Toffolon, M., and S. Lanzoni, (2010), Morphological equilibrium of short channels dissecting the tidal flats of coastal lagoons, Journal Geophysical Research, 115, F04036.

Tonelli, M., S. Fagherazzi, and M. Petti (2010), Modeling wave impact on salt marsh boundaries, Journal Geophysical Research, 115, C09028.

Whitehouse, R., R. Soulsby, W. Roberts, and H. Mitchener, (2000), Dynamics of estuarine muds, 210 pp., Thomas Telford Publishing.

Yang, S., C.T. Friedrichs, Z. Shi, P. Ding, J. Zhu, and Q. Zhao, (2003), Morphological response of tidal marshes, flats and channels of the outer Yangtze river mouth to a major storm, Estuaries, 26, 6, 1416–1425.

Final remarks

The study presented here shows that RSLR affects coastal systems morphology in a dynamical way. Both tidal flat and marsh boundary erosion is predicted to increase with RSLR, threatening the delicate equilibrium of coastal wetlands.

This study also suggests that high sediment availability is a crucial factor for marsh stability. This result advocates for wetland preservation projects based on increasing fluvial sediment input to the coast, through dam removal and controlled river diversions.

Both field measurements and models reveal the morphological coupling between the different compartments of a costal wetland: tidal channels, tidal flats and low salt marsh platform. Additional interactions are expected to occur between other compartments, such as tidal creeks and high marsh platform. Further studies are sought to reveal these interactions, allowing for a better understanding of coastal wetlands, more reliable prediction of their morphological evolution, and optimal anthropogenic interventions.

References

Abdelrhman, M.A., (2007), Modeling coupling between eelgrass Zostera Marina and water flow, Mar. Ecol. Prog. Ser., 338, 81-96.

Allen J.R.L., (2000), Morphodynamics of Holocene salt marshes: a review sketch from the Atlantic and Southern North Sea coasts of Europe, Quaternary Science Review, 19, 12, 1155-1231.

Allen, J.R.L., and P. Somerfield, and F. Gilbert, (2007), Quantifying uncertainty in high-resolution coupled hydrodynamic-ecosystem models, Journal Marine Systems, 64, 1-4, 3-14.

Allen, J.R.L., and Duffy M.J., (1998), Medium-term sedimentation on high intertidal mudflats and salt marshes in the Severn Estuary, SW Britain: the role of wind and tide, Marine Geology, 150, 1–27.

Amos, C.L., N.A. Van Wagoner, and G.R. Daborn, (1988), The influence of subaerial exposure on the bulk properties of fine-grained intertidal sediments from Minas Basin, Bay of Fundy, Estuarine, Coastal and Shelf Science, 27, 1-13.

Ashley, G.M., and M.L. Zeff, (1988), Tidal channel classification for a low-mesotidal salt-marsh, Marine Geology, 82, 1-2, 17-32.

Banas, N.S., B.M. Hickey, P. MacCready, and J. A. Newton, (2004), Dynamics of Willapa Bay, Washington: A highly unsteady, partially mixed estuary, Journal of Physical Oceanography, 34, 11, 2413-2427.

Black, K.S., (1998), Suspended sediment dynamics and bed erosion in the high shore mudflat region of the Humber estuary, UK, Marine Pollution Bulletin, 37, 3-7, 122-133.

Blum, L.K., and R.R. Christian, (2004), Belowground production and decomposition along a tidal gradient in a Virginia salt marsh. In The Ecogeomorphology of Tidal Marshes, eds. S. Fagherazzi, M. Marani, and L.K. Blum, 47–74. Washington, DC: American Geophysical Union.

Boon, J.D., (2004), Secrets of the tide, Horwood Publishing Limited, pp. 210.

Bouws, E., H. Gunther, W. Rosenthal, and C. L. Vincent, (1985), Similarity of the wind wave spectrum in finite depth water. 1 Spectral form, Journal of Geophysical Research, 90, (NC1), 975-986.

Breugem, W.A., and L.H. Holthuijsen, (2007), Generalized Shallow Water Wave Growth from Lake George, Journal of Waterway, Port, Coastal, and Ocean Engineering, 133, 3.

Boon, J.D., and R.J. Byrne, (1981), On basin hypsometry and the morphodynamic response of coastal inlet systems, Marine Geology, 40, 27-48.

Boon, J.D., (1975), Tidal discharge asymmetry in a salt marsh drainage system, Limnology and Oceanography, 20, 71–80.

Boynton, W.R., J.D. Hagy, L. Murray, C. Stokes, and W.M. Kemp, (1996), A comparative analysis of eutrophication patterns in a temperate coastal lagoon, Estuaries 19, 408-421.

Brampton, A. H., (1992), Engineering significance of British saltmarshes, 115–122. In J. R. L. Allen and K. Pye (Eds.), Saltmarshes: Morphodynamics, conservation, and engineering significance.

Cappucci, S., C.L. Amos, T. Hosoe, and G. Umgiesser, (2004), SLIM: a numerical model to evaluate the factors controlling the evolution of intertidal mudflats in Venice Lagoon, Italy, Journal of Marine Sediments, 51, 257-280.

Carniello, L., A. Defina, S. Fagherazzi, and L. D'Alpaos, (2005), A combined wind wave-tidal model for the Venice lagoon, Italy, Journal of Geophysical Research, 110, F04407.

Carniello, L., A. D'Alpaos, and A. Defina, (2009a), Simulation of wind waves in shallow microtidal basins: Application to the Venice Lagoon, Italy. Proceedings of 6th IAHR Symposium on River, Coastal and Estuarine Morphodynamics: RCEM 2009 – Vionnet C.A., Garcia M.H., Latrubesse E.M. and Perillo G.M.E. editors. Taylor & Francis Group, London, ISBN 978-0-415-55426-8, Vol. (2), pp. 907-912.

Carniello, L., A. Defina, and L. D'Alpaos, (2009b), Morphological evolution of the Venice Lagoon: evidence from the past and trend for the future, Journal of Geophysical Rsearch, 114, F04002.

CERC, Coastal Engineering Research Center, (1984), Shore Protection Manual. U.S. Army Coastal Engineering Research Center.

Carling, P.A., J.J. Williams, I.W. Croudace, and C.L. Amos, (2009), Formation of mud ridge and runnels in the intertidal zone of the Severn Estuary, UK. Continental Shelf

Research, 29, 16, 1913-1926.

Chapra, S.C., (1996), Surface Water-Quality Modeling. McGraw-Hill, 784 pp.

Christiansen, C., G. Volund, L. C. Lund-Hansen, and J. Bartholdy, (2006), Wind influence on tidal flat sediment dynamics: Field investigations in the Ho Bugt, Danish Wadden Sea, Marine Geology, 235, 1-4, 75-86.

Christie, M.C., K.R. Dyer, and P. Turner, (1999), Sediment flux and bed level measurements from a macro tidal mudflat, Estuarine Coastal and Shelf Science, 49, 5, 667-688.

Christie, M.C., and Dyer, K.R., (1998), Measurements of the turbid edge over the Skeffling mudflats. In: Black, K.S., Paterson, D.M., Cramp, A. (Eds.) Sedimentary Processes in the Intertidal Zone. Geological Society, London, Special Publication 139, 45-55.

Collins, M.B., X. Ke, and S. Gao, (1998), Tidally-induced Flow Structure Over Intertidal Flats, Estuarine, Coastal and Shelf Science, 46, 233–250.

Collins, J.I., (1972), Prediction of shallow-water spectra. Journal of Geophysical Research, 77, 2693-2707.

Cowell, P.J., M.J.F. Stive, A.W. Niedoroda, H.J. DE Vriend, D.J.P. Swift, G.M. Kaminsky, and M. Capobianco, (2003), The coastal-tract (part 1): a conceptual approach to aggregated modeling of low-order coastal change. Journal of Coastal Research, 19, 4, 812-827.

D'Alpaos, A., S. Lanzoni, M. Marani, S. Fagherazzi, and A. Rinaldo, (2005), Tidal network ontogeny: Channel initiation and early development, Journal of Geophysical Rsearch, 110, F02001.

D'Alpaos, A., S. Lanzoni, M. Marani, and A. Rinaldo, (2010), On the tidal prism–channel area relations, Journal of Geophysical Rsearch, 115, F01003.

D'Alpaos, L., and A. Defina, (2007), Mathematical modeling of tidal hydrodynamics in shallow lagoons: A review of open issues and applications to the Venice lagoon, Computers & Geoscience., 33, 476-496.

D'Alpaos, A., S. Lanzoni, S.M. Mudd, and S. Fagherazzi, (2006), Modeling the influence of hydroperiod and vegetation on the cross-sectional formation of tidal channels Estuarine, Coastal and Shelf Science 69, 3-4, 311-324.

de Brouwer, J.F.C., S. Bjelic, M.G.T. de Deckere, and L.J. Stal, (2000), Interplay between biology and sedimentology in a mudflat (Biezelingse Ham, Westerschelde, The Netherlands), Continental Shelf Research, 20, 10-11, 1159-1177.

Defina, A., L. Carniello, S. Fagherazzi, and L. D'Alpaos, (2007), Self organization of shallow basins in tidal flats and salt marshes, Journal of Geophysical Research, 112, F03001.

Defina, A., (2000), Two-dimensional shallow water equations for partially dry areas, Water Resource Research, 36, 3251– 3264.

de Swart, H E., and J.T.F. Zimmerman, (2009), Morphodynamics of Tidal Inlet Systems, Annual Review of Fluid Mechanics, 41, 203-229.

Deines, K.L., (1999), Backscatter estimation using broadband acoustic Doppler Current Profilers, 249-253 pp., Ieee, New York.

Di Silvio, G., C. Dall'Angelo, D. Bonaldo, and G. Fasolato, (2010), Long-term model of planimetric and bathymetric evolution of a tidal lagoon, Continental Shelf Research, 30, 894–903.

Downing, A., P.D. Thorne, and C E. Vincent, (1995), Backscattering from a suspension in the near-field of a piston transducer, Journal of the Acoustical Society of America, 97, 3, 1614-1620.

Dronkers, J., (1978), Longitudinal dispersion in shallow well-mixed estuaries, Coastal Engineering Conference 3, 169.

Dronkers, J., (1986), Tidal asymmetry and estuarine morphology, Netherlands Journal of Sea Research, 20, 2-3, 117-131.

Dyer, K.R., M.C. Christie, N. Feates, M.J. Fennessy, M. Pejrup, and W. van der Lee, (2000), An investigation into processes influencing the morphodynamics of an intertidal mudflat, the Dollard estuary, the Netherlands: I. Hydrodynamics and suspended sediment, Estuarine Coastal and Shelf Science, 50, 5, 607-625.

Eisma, D., (1997), Intertidal Deposits: River Mouths, Tidal Flats and Coastal Lagoons, Marine Science Series, CRC Press, Boca Raton, 507.

Emory, K.O., and D.G. Aubrey, (1991), Sea levels, land levels and tide gauges. Springer-Verlag, NY.

Fagherazzi, S., and D. J. Furbish, (2001), On the shape and widening of salt marsh creeks, Journal of Geophysical Rsearch, 106, C1, 991-1005, 2001.

Fagherazzi, S., M. Hannion, and P. D'Odorico, (2008), Geomorphic structure of tidal hydrodynamics in salt marsh creeks, Water Resource Research, 44, W02419, 512.

Fagherazzi S., and T. Sun, (2003), Numerical simulations of transportational cyclic steps Computers & Geosciences, 29, 9, 1071-1201.

Fagherazzi S., M. Marani, and L.K. Blum (Editors), (2004), The Ecogeomorphology of Tidal Marshes, American Geophysical Union Coastal and Esturine Studies, Washington DC, Volume 59, 266 pages.

Fagherazzi, S., Carniello L., D'Alpaos L., and A. Defina, (2006), Critical bifurcation of shallow microtidal landforms in tidal flats and salt marshes, Proceeding of the National Academy of Sciences, 103, 22, 8337-8341.

Fagherazzi, S., C. Palermo, M. C. Rulli, L. Carniello, and A. Defina, (2007), Wind waves in shallow microtidal basins and the dynamic equilibrium of tidal flats, Journal of Geophysical Rsearch, 112, F02024.

Fagherazzi, S., and P.L. Wiberg, (2009), The importance of wind conditions, fetch and water levels on wave generated shear stresses in a shallow intertidal basin, Journal of Geophysical Research, 114, F03022.

Fagherazzi, S., and A.M. Priestas, (2010), Sediments and water fluxes in a muddy coastline: interplay between waves and tidal channel hydrodynamics, Earth Surface Processes and Landforms, 35, 3, 284-293.

Fagherazzi, S., P.L. Wiberg, and A.D. Howard, (2003), Tidal flow field in a small basin, Journal of Geophysical Research, 108, C3, 3071.

FitzGerald, D.M., I.V. Buynevich, and B.A. Argow, (2006), Model of tidal inlet and barrier island dynamics in a regime of accelerated sea-level rise, Journal of Coastal Research, 39, 789–795.

FitzGerald, D.M., (1996), Geomorphic Variability and Morphologic and Sedimentary Controls on Tidal Inlets, Journal of Coastal Research, 23, 47-71.

Fredsoe, J. and R. Deigaard, (1993), Mechanics of Coastal Sediement Transport, Advanced Series in Ocean Engineering, Vol. 3, World Scientific, Singapore, 369pp.

Friedrichs, C.T., B.A. Armbrust, and H.E. de Swart, (1998), Hydrodynamics and equilibrium sediment dynamics of shallow, funnel-shaped tidal estuaries. In: J. Dronkers and M. Scheffers (Eds.), Physics of Estuaries and Coastal Seas, Balkema Press, Rotterdam, The Netherlands, p. 315-328.

Friedrichs, C.T., (1995), Stability shear stress and equilibrium cross-sectional geometry of sheltered tidal channels, Journal of Coastal Research, 11, 1062-1074.

Friedrichs, C.T. and D.G. Aubrey, (1996), Uniform bottom shear stress and equilibrium hypsometry of intertidal flats. In: C. Pattiaratchi (ed.), Mixing Processes in Estuaries and Coastal Seas. American Geophysical Union, Washington, D.C., 405-429.

Friedrichs, C.T., and D.G. Aubrey, (1988), Non-linear Tidal Distortion in Shallow Well-mixed Estuaries: a Synthesis, Estuarine, Coastal and Shelf Science, (1988), 27, 521-545.

Friedrichs, C.T., and O.S. Madsen, (1992), Nonlinear Diffusion of the Tidal Signal in Frictionally Dominated Embayments, Journal of Geophysical Research, 97, C4, 5637-5650.

Friedrichs, C.T., (2012), Tidal flat morphodynamics: a synthesis. In: J.D. Hansom and B.W. Flemming (Eds.), Treatise on Estuarine and Coastal Science, Volume 3: Estuarine and Coastal Geology and Geomorphology, Elsevier, in press.

Gartner, J.W., (2004), Estimating suspended solids concentrations from backscatter intensity measured by acoustic Doppler current profiler in San Francisco Bay, California, Marine Geology, 211, 3-4, 169-187.

Geyer, W.R., (1993), The importance of suppression of turbulence by stratification on the estuarine turbidity maximum, Estuaries, 16, 1, 113-125.

Gibbons, D.T., G. Jones, A. Hay, and F. Johnson, (1983), Performance of a new submersible tide-wave recorder, UNESCO, Technical paper in marine science.

Gloor, M., A. Wuest, and M. Munnich, (1994), Benthic boundary mixing and resuspension induced by internal seiches, Hydrobiologia, 284,1, 59-68.

Goda, Y., (1970), New Wave pressure Formulae for Composite Breakwaters, Proceedings of the 14th International Coastal Engineering Conference, 3, 1702-1720.

Green, M.O., and G. Coco, (2007), Sediment transport on an estuarine intertidal flat: Measurements and conceptual model of waves, rainfall and exchanges with a tidal creek, Estuarine Coastal and Shelf Science, 72, 4, 553-569.

Green, M.O., K.P. Black, and C.L. Amos, (1997), Control of estuarine sediment dynamics by interactions between currents and waves at several scales, Marine Geology, 144, 1-3, 97-116.

Hayden, B.P., M. Santos, G. Shao, and R.C. Kochel, (1995), Geomorphological controls on coastal vegetation at the Virginia Coast Reserve, Geomorphology, 13, 1-4, 283-300.

Holthuijsen, L.H., N. Booij, and T.H.C. Herbers, (1989), A prediction model for stationary, short-crested waves in shallow water with ambient currents, Coastal Engineering, 13, 23-54.

Hickey, B.M., and N.S. Banas, (2003), Oceanography of the US Pacific Northwest Coastal Ocean and estuaries with application to coastal ecology, Estuaries, 26, 4B, 1010-1031.

Hill, P.S., J.P. Newgard, B.A., Law, and T.G. Milligan, (2011), Linking suspended floc dynamics to the spatial distribution of sediment texture on the Shoalwater Bay tidal complex in Willapa Bay, Continental Shelf Research, submitted to special issue: Tidal Flats.

Hoitink, A.J.F., and P. Hoekstra, (2005), Observations of suspended sediment from ADCP and OBS measurements in a mud-dominated environment, Coastal Engineering, 52, 2, 103-118.

Hoitink, A.J.F., P. Hoekstra, and D.S. van Maren, (2003), Flow asymmetry associated with astronomical tides: Implications for the residual transport of sediment, Journal of Geophysical Research, 108, C10.

Hsu, T.J., S.N. Chen, and A.S. Ogston, (2011), A numerical investigation of fine sediment transport across intertidal flats, Continental Shelf Research, submitted to special issue: Tidal Flats.

Janssen-Stelder, B., (2000), The effect of different hydrodynamic conditions on the morphodynamics of a tidal mudflat in the Dutch Wadden Sea, Continental Shelf Research, 20, 1461-1478.

James, W.F., J.W. Barko, and G.B. Malcolm, (2004), Shear stress and sediment resuspension in relation to submersed macrophyte biomass, Hydrobiologia, 515, 181–191.

Jarrett, J.T., (1976), Tidal prism-inlet area relationships, Gen. Invest. Tidal Inlets Rep. 3, 32 pp., U.S. Army Coastal Eng. Res. Cent., Fort Belvoir, VA.

Kamphuis, J.W., (1975), Friction factor under oscillatory waves, Journal of Waterway, Port, Coastal, and Ocean Engineering., 101, 135– 144.

Ke, X.K., M.B. Collins, and S.E. Poulos, (1994), Velocity structure and sea-bed roughness associated with intertidal (sand and mud) flats and salt-marshes of the wash, UK, Journal of Coastal Research, 10, 3, 702-715.

Kirwan, M.L., and A.B. Murray, (2007), A coupled geomorphic and ecological model of tidal marsh evolution, Proceedings of the National Academy of Sciences of the United States of America, 104, 15, 6118-6122.

Kornman, B.A., and E.M.G.T. de Deckere, (1998), Temporal variation in sediment erodibility and suspended sediment dynamics in the Dollard estuary. In: Black, K. S., Paterson, D. M., Cramp, A. (Eds.), Sedimentary Processes in the Intertidal Zone, Geological Society, London, Special Publications 139, pp. 231–241.

Lacy, J.R., M.T. Stacey, J.R. Burau, and S.G. Monismith, (2003), Interaction of lateral baroclinic forcing and turbulence in an estuary, Journal of Geophysical Research, 108, C3, 3089.

Lanzoni, S., and G. Seminara, (2002), Long term evolution and morphodynamic equilibrium of tidal channels, Journal of Geophysical Research, 107, C1, 3001.

Law, B.A., T.G. Milligan, P.S. Hill, J. Newgard, R.A. Wheatcroft, and P.L. Wiberg, (2011), Bed sediment texture on the Shoalwater Bay tidal complex, Willapa Bay: role of flocculation, Continental Shelf Research, submitted to special issue: Tidal Flats.

Lawson, S.E., P.L. Wiberg, K.J. McGlathery, and D.C. Fugate, (2007), Wind-driven sediment suspension controls light availability in a shallow coastal lagoon, Estuaries and Coasts 30, 1, 102-112.

Lawson, S.E., (2004) Sediment suspension as a control on light availability in a coastal lagoon, M.S. Thesis, University of Virginia, Charlottesville, VA, 119pp.

Lawson, S.E., (2008), Physical and biological controls on sediment and nutrient fluxes in a temperate lagoon, Ph.D. Thesis, University of Virginia, Charlottesville, VA, 187pp.

Le Hir, P., W. Roberts, O. Cazaillet, M. Christie, P. Bassoullet, and C. Bacher, (2000), Characterization of intertidal flat hydrodynamics, Continental Shelf Research, 20, 12-13, 1433-1459.

Le Hir, P., Y. Monbet, and F. Orvain, (2007), Sediment erodability in sediment transport modelling: Can we account for biota effects?, Continental Shelf Research, 27, 8, 1116-1142.

Le Hir, P., W. Roberts, O. Cazaillet, M. Christie, P. Bassoullet, and C. Bacher, (2000), Characterization of intertidal flat hydrodynamics, Continental Shelf Research, 20, 12-13, 1433-1459.

Lesser, G., J. Roelvink, J. Van Kester, and G. Stelling, (2004), Development and validation of a three-dimensional morphological model, Coastal Eng., 51, 883– 915.

Le Hir, P., W. Roberts, O. Cazaillet, M. Christie, P. Bassoullet, and C. Bacher, (2000), Characterization of intertidal flat hydrodynamics, Continental Shelf Research, 20, 12-13, 1433-1459.

Li, C.Y., and J. O' Donnell, (1997), Tidally driven residual circulation in shallow estuaries with lateral depth variation, Journal of Geophysical Research, 102, C13, 27915-27929.

Li, C.Y., and A. Valle-Levinson, (1999), A two-dimensional analytic tidal model for a narrow estuary of arbitrary lateral depth variation: The intratidal motion, Journal of Geophysical Research, 104, C10, 23525-23543.

Li, C.Y., and J. O' Donnell, (2005), The effect of channel length on the residual circulation in tidally dominated channels, Journal of Physical Oceanography, 35, 10, 1826-1840.

Marani, M., A. D'Alpaos, S. Lanzoni, L. Carniello, and A. Rinaldo, (2007), Biologically-controlled multiple equilibria of tidal landforms and the fate of the Venice lagoon, Geophysical Research Letters, 34, L11402.

Marani, M., A. D'Alpaos, S. Lanzoni, L. Carniello, and A. Rinaldo, (2010), The importance of being coupled: Stable states and catastrophic shifts in tidal biomorphodynamics, Journal of Geophysical Research, 115, F04004, 15.

Mariotti, G., and S. Fagherazzi, (2012a), Wind waves on a mudflat: the influence of fetch and depth on bed shear stresses, Continental Shelf Research, special issue: Tidal Flats.

Mariotti, G., and S. Fagherazzi, (2012b), Channels-tidal flat sediment exchange: The channel spillover mechanism, Journal of Geophysical Research, 117, C03032.

Mariotti G., and Fagherazzi S., (2010c), A numerical model for the coupled long-term evolution of salt marshes and tidal flats, Journal of Geophysical Research, 115, F01004.

Mariotti, G., and S. Fagherazzi, (2011), Asymmetric fluxes of water and sediments in a mesotidal mudflat channel, Continental Shelf Research, 31, 1, 23-36.

Moeller, I., T. Spencer, and J.R. French, (1996), Wave attenuation over saltmarsh surfaces: Preliminary results from Norfolk, England, Journal of Coastal Research, 12, 4, 1009-1016.

Möeller, I., T. Spencer, J.R French., D.J. Leggett and M. Dixon, (1999), Wave transformation over salt marshes: A field and numerical modelling study from north Norfolk, England, Estuarine Coastal and Shelf Science, 49, 3, 411-426.

Möeller I., (2006), Quantifying saltmarsh vegetation and its effect on wave height dissipation: Results from a UK East coast saltmarsh, Estuarine, Coastal and Shelf Science, 69, 337-351.

Morris, J.T., and B. Haskin, (1990), A 5-yr record of aerial primary production and stand characteristics of Spartina alterniflora, Ecology, 71, 6, 2209-2217.

Morris, J.T., P.V. Sundareshwar, C.T. Nietch, B. Kjerfve, and D.R. Cahoon, (2002) Responses of coastal wetlands to rising sea level, Ecology, 83, 2869-2877.

Morris, J.T., (2006), Competition among marsh macrophytes by means of geomorphological displacement in the intertidal zone, Estuarine, Coastal and Shelf Science, 69, 395-402.

Mudd, S.M., Fagherazzi S., Morris J.T., and Furbish D.J., (2004), Flow, sedimentation, and biomass production on a vegetated salt marsh in South Carolina: toward a predictive model of marsh morphologic and ecologic evolution, in Fagherazzi, S., M. Marani, and L.K. Blum, (Eds.) The Ecogeomorphology of Salt Marshes, Estuarine and Coastal Studies Series, American Geophysical Union, Washington D.C., pp. 165-187.

Mudd, S.M., S. Fagherazzi, J.T. Morris, and D.J. Furbish., (2004), Flow, Sedimentation, and Biomass Production on a Vegetated Salt Marsh in South Carolina: Toward a Predictive Model of Marsh Morphologic and Ecologic Evolution, Coastal and Estuarine Studies.

Mota Oliveira, I.B, (1970), Natural flushing ability in tidal inlets. Proceedings Coastal Engineering Conference, 12th, Washington, DC, 3, 1827–1845. Washington, DC.

Nerem, R., T. van Dam, and M. Schenewerk, (1998), Chesapeake Bay subsidence monitored as wetland loss continues, EOS 79, 156–157.

Nichols, M.M., and J.D. Boon, (1994), Sediment transport processes in coastal lagoons, in Coastal Lagoon Processes, B.. Kjerfve (Ed.), Elsevier, 157-217.

Nidzieko, N. J., (2010), Tidal asymmetry in estuaries with mixed semidiurnal/diurnal tides, Journal of Geophysical Research, 115, C08006.

Nikuradse, J., (1933), Stromungsgesetz in rauhren rohren, vDI Forschungshefte 361 (English translation: Laws of flow in rough pipes), Tech. Rep. NACA Technical Memorandum 1292. National Advisory Commission for Aeronautics, Washington, D. C., USA (1950).

Nowacki, D.J., and A.S. Ogston, (2011), Water and sediment transport of channel-flat systems in a mesotidal mudflat: Willapa Bay, Washington, Continental Shelf Research, submitted to special issue: Tidal Flats.

Oertel, G.F., G.T.F. Wong, and J.D. Conway, (1989), Sediment accumulation at a fringe marsh during transgression, Oyster, Virginia, Estuaries, 12, 18-26.

Oertel, G F., (2001), Hypsographic, hydro-hypsographic and hydrological analysis of coastal bay environments, Great Machipongo Bay, Virginia, Journal of Coastal Research, 17, 4, 775-783.

Okubo, A., (1973), Effects of shortline irregularities on streamwise dispersion in estuaries and other embayments, Netherlands Journal of Sea Research, 6, 1–2, 213–224.

Parchure, T.M., and A.J. Metha, (1985), Erosion of soft cohesive sediment deposits, Journal of Hydraulic Engineering- ASCE, 111 (10), 1308-1326.

Parker, G., M.H. Garcia,Y. Fukushima, and W. Yu, (1987), Experiments on turbidity currents aver an erodible bed, Journal of Hydraulic Research, 25, 1, 123-147.

Pejrup, M., (1988), Suspended sediment transport across a tidal flat, Marine Geology, 82, 3-4, 187-198.

Peterson, C., K. Scheidegger, P. Komar, and W. Niem, (1984), Sediment composition and hydrography in 6 high-gradient estuaries of the northwestern united-states, Journal of Sedimentary Petrology, 54, 1, 86-97.

Phillips, J.D., (1992), Nonlinear dynamical systems in geomorphology: revolution or evolution? Geomorphology, 5 3–5, 219–229.

Pizzuto, J.E., and T.S. Meckelnburgts, (1989), Evaluation of a linear bank erosion equation, Water resources research, 25, 5, 1005-1013.

Postma, H., (1961), Transport and accumulation of suspended matter in the dutch Wadden Sea, Netherland journal of sea research, 1, 148-190.

Pritchard, D., (2005), Suspended sediment transport along an idealized tidal embayment: settling lag, residual transport and the interpretation of tidal signals, Ocean Dynamics, 55, 2, 124-136.

Pritchard, D., A.J. Hogg, and W. Roberts (2002), Morphological modelling of intertidal mudflats: the role of cross-shore tidal currents, Continental Shelf Research, 22, 11-13, 1887-1895.

Pritchard, D., A.J. Hogg, and W. Roberts, (2002), Morphological modelling of intertidal mudflats: the role of cross-shore tidal currents, Continental Shelf Research, 22, 1887–1895.

Pritchard, D., and A.J. Hogg, (2003), Cross-shore sediment transport and the equilibrium morphology of mudflats under tidal currents, Journal of Geophysical Research, 108, C10, 3313.

Press, W.H., S.A. Teukolsky, W.T. Vetterling, and B.P. Flannery, (1992), Numerical Recipes (second ed.), Cambridge University Press, Cambridge

Ralston, D.K., and M.T. Stacey, (2005), Longitudinal dispersion and lateral circulation in the intertidal zone, Journal of Geophysical Research, 110, C07015.

Ralston, D.K., and M.T. Stacey, (2007), Tidal and meteorological forcing of sediment transport in tributary mudflat channels, Continental Shelf Research, 27, 10-11, 1510-1527.

Randerson, P.F., (1979), A simulation of salt-marsh development and plant ecology. In: Knights, B., A.J. Phillips (Eds.), Estuarine and Coastal Land Reclamation and Water Storage, Sazon House, Farnborough, 48-67.

Ridderinkhof, H., R. van der Ham, and W. van der Lee, (2000), Temporal variations in concentration and transport of suspended sediments in a channel-flat system in the Ems-Dollard estuary, Continental Shelf Research, 20, 12-13, 1479-1493.

Roberts, W., P. Le Hir, and R.J.S. Whitehouse, (2000), Investigation using simple mathematical models of the effect of tidal currents and waves on the profile shape of intertidal mudflats, Continental Shelf Research, 20, 10-11, 1079-1097.

Robinson, S.E., (1994), Clay mineralogy and sediment texture of environments in a barrier island-lagoon system, M.S. Thesis, University of Virginia, 102pp.

Ruddy G., C.M. Turley, T.E.R. Jones, (1998), Ecological interaction and sediment transport on an intertidal mudflat I. Evidence for a biologically mediated sediment-water interface. In: Black, K.S., Paterson, D.M., Cramp, A. (Eds.) Sedimentary Processes in the Intertidal Zone, Geological Society, London, Special Publication, 139, 135-148.

Sainflou, M., (1928), Treatise on Vertical Breakwaters. Annals des Ponts et Chaussee, (Translated by W.J. Yardoff, U.S. Army Corps of Engineers.).

Schwimmer, R.A., (2001), Rates and Processes of Marsh Shoreline Erosion in Rehoboth Bay, Delaware, U.S.A, Journal of Coastal Research, 17, 3, 672-683.

Schwimmer, R.A., and J.E. Pizzuto, (2000), A Model for the Evolution of Marsh Shorelines, Journal of Sedimentary Research, 70, 5, 1026-1035.

Seminara, G., Meanders, (2006), Journal of Fluid Mechanics, 554, 271-279.

Seminara, G., S. Lanzoni, N. Tambroni, and M. Toffolon, (2009), How long are tidal channels? Journal of Fluid Mechanics, 1-16.

Simpson, J.H., J. Brown, J. Matthews, and G. Allen, (1990), Tidal straining, density currents, and stirring in the control of estuarine stratification, Estuaries, 13, 2, 125-132.

Sommerfield, C.K., and K.C. Wong, (2011), Mechanisms of sediment flux and turbidity maintenance in the Delaware Estuary, Journal of Geophysical Research, 116, C01005.

Song, Y., and D.B. Haidvogel, (1994), A semi-implicit ocean circulation model using a generalized topography-following coordinate, Journal of Computational Physics., 115, 1, 228–244.

Soulsby, R.L., and K.R. Dyer, (1981), The form of the near-bed velocity profile in a tidally accelerating flow, Journal of Geophysical Research, 86, NC9, 8067-8074.

Soulsby, R.L. (1997), Dynamics of Marine Sands, pp. 250, Thomas Telford Publications, London, Thomas Telford Publications.

Soulsby, R.L., (1995), Bed shear-stresses due to combined waves and currents, in Advances in Coastal Morphodynamics, edited by M.J.F. Stive et al., pp. 4-20 – 4-23, Delft Hydraulic, Delft, Netherlands.

Speer, P.E., and D.G. Aubrey, (1985), A Study of Non-linear Tidal Propagation in

Shallow Inlet/Estuarine Systems. Part II: Theory, Estuarine, Coastal and Shelf Science, 21, 207-224.

Stacey, M.T., and D.K. Ralston, (2005), The scaling and structure of the estuarine bottom boundary layer, Journal of Physical Oceanography, 35, 1, 55-71.

Stive, M.J.F., J.A. Roelvink, and H.J. DeVriend, (1990), Large scale coastal evolution concept, Proceedings 22nd Coastal Engineering Conference, 1962–1974.

Tambroni, N., and G. Seminara, (2006), Are inlets responsible for the morphological degradation of Venice Lagoon?, Journal Geophysical Research, 111, F03013.

Tanimoto, K., K. Moto, S. Ishizuka, and Y. Goda, (1976), An Investigation on Design Wave Force Formulae of Composite-Type Breakwaters, Proceedings of the 23rd Japanese Conference on Coastal Engineering, pp 11-16 (in Japanese).

Talke, S.A., and M.T. Stacey, (2008), Suspended sediment fluxes at an intertidal flat: The shifting influence of wave, wind, tidal, and freshwater forcing, Continental Shelf Research, 28, 6, 710-725.

Tilburg, C.E., and R.W. Garvine, (2004), A Simple Model for Coastal Sea Level Prediction, Weather and Forecasting, 19, 3, 511-519.

Tolhurst, J., E.C. Defew, R.G. Perkins, A. Sharples, and D.M. Paterson, (2006), The effects of tidally-driven temporal variation on measuring intertidal cohesive sediment erosion threshold, Aquatic Ecology, 40, 4, 521-531.

Tolhurst, J., E.C. Defew, J.F.C. de Brouwer, K. Wolfstein, L.J. Stal, and D.M. Paterson, (2006b), Small-scale temporal and spatial variability in the erosion threshold and properties of cohesive intertidal sediments, Continental Shelf Research, 26, 351-362.

Tolhurst, T.J., C.W. Watts, S. Vardy, J.E. Saunders, M.C. Consalvey, and D.M. Paterson, (2008), The effects of simulated rain on the erosion threshold and biogeochemical properties of intertidal sediments, Continental Shelf Research, 28, 10-11, 1217-1230.

Toffolon, M., and S. Lanzoni, (2010), Morphological equilibrium of short channels dissecting the tidal flats of coastal lagoons, Journal Geophysical Research, 115, F04036.

Tonelli, M., S. Fagherazzi, and M. Petti, (2010), Modeling wave impact on salt marsh boundaries, Journal Geophysical Research, 115, C09028.

Trenhaile, A. S., (2009), Modeling the erosion of cohesive clay coasts, Coastal Engineering, 56 (1), 59-72.

Tucker, M.J., and E.G. Pitt, (2001), Waves in ocean engineering, 521 pp., Elsevier, The Netherlands.

Uncles, R.J., and J.A. Stephens, (2000), Observations of currents, salinity, turbidity and intertidal mudflat characteristics and properties in the Tavy Estuary, UK, Continental Shelf Research, 20, 12-13, 1531-1549.

Uncles, R.J., R.C.A. Elliott, and S.A. Weston, (1986), Observed and computed lateral circulation patterns in a partly mixed estuary, Estuarine Coastal and Shelf Science, 22, 4, 439-457.

Umgiesser, G., D.M. Canu, A. Cucco, and C. Solidoro, (2004), A finite element model for the Venice Lagoon, Development, set up, calibration and validation, Journal of Marine Systems, 51, 1-4, 123-145.

van de Koppel, J., D. van der Wal, J.P. Bakker, and P.M.J. Herman, (2005), Self-organization and vegetation collapse in salt marsh ecosystems, American Naturalist, 165, 1, E1-E12.

van Rijn, L.C., (2007), Unified view of sediment transport by currents and waves. I: Initiation of motion, bed roughness, and bed-load transport, Journal of Hydraulic Engineering, 133, 6, 649-667.

Vogel S., (1994), Life in moving fluids: the physical biology of flow, 2nd edn. Princeton University Press, Princeton, NJ.

Waeles, B., P. Le Hir, and R. Silva Jacinto, (2004), Modélisation morphodynamique cross-shore d'un esrtan vaseux, Comptes Rendus Geoscience 336, 1025-1033 (in French, with abridged English version).

Warner, J.C., D.H. Schoellhamer, C.A. Ruhl, and J.R. Burau, (2004), Floodtide pulses after low tides in shallow subembayments adjacent to deep channels, Estuarine Coastal and Shelf Science, 60, 2, 213-228.

Whitehouse, R.J.S., and H.J. Mitchener, (1998), Observations of the morphodynamics behavior of an intertidal mudflat at different timescales, In: Black, K.S., Paterson, D.M., Cramp, A. (Eds.) Sedimentary Processes in the Intertidal Zone. Geological Society, London, Special Publication, 139, 255-271.

Whitehouse, R., R. Soulsby, W. Roberts, and H. Mitchener, (2000), Dynamics of estuarine muds, 210 pp., Thomas Telford Publishing.

Wiberg, P.L., and C.R. Sherwood, (2008), Calculating wave-generated bottom orbital velocities from surface-wave parameters, Computers & Geosciences, 34, 10, 1243-1262.

Wiber, P.L., R. Wheatcroft, P. Hill, T. Milligan, B. Law and J. Newgard, (2011), Sediment erodibility on a tidal flat: channel complexes in southern Willapa Bay, Continental Shelf Research, submitted to special issue: Tidal Flats.

Williams, J.J., P.A. Carling, C.L. Amos, and C. Thompson, (2008), Field investigation of ridge-runnel dynamics on an intertidal mudflat, Estuarine Coastal and Shelf Science, 79, 2, 213-229.

Winterwerp, J.C., (2011), Fine sediment transport by tidal asymmetry in the high-concentrated Ems River: indications for a regime shift in response to channel deepening, Ocean Dynamics, 61, 2-3, 203-215.

Woodroffe, (2003), Coasts. Form, processes and evolution, Cambridge University press, 623pp.

Yang, S., C.T. Friedrichs, Z. Shi, P. Ding, J. Zhu, and Q. Zhao, (2003), Morphological response of tidal marshes, flats and channels of the outer Yangtze river mouth to a major storm, Estuaries, 26, 6, 1416–1425.

Young, I. R., and L. A. Verhagen, (1996), The growth of fetch-limited waves in water of finite depth. Part 1: Total energy and peak frequency, Coastal Engineering, 29, 1–2,

47–78.

Curriculum Vitae

Giulio Mariotti

A. Education

- Boston University, Coastal Geomorphology, Ph.D. candidate, (2008 – present).
- University of Florence (Italy), Environmental engineering, M.Sc., (2008), 110/110 cum laude.
- University of Florence (Italy), Environmental engineering, B.Sc., (2006), 110/110 cum laude.

B. Honors and Awards

- Fellow of the 2011 GFD summer program at Woods Hole Oceanographic Institution (Woods Hole, MA).
- Awarded as best student of the Engineering College (University of Florence) for the highest graduation vote achieved in the shortest time during the academic year 2005/2006.

C. Research and Experience

- Teaching fellow (2010), Boston University, Boston, MA.
- Research assistant (2008-present), Boston University, Boston, MA.
- Boston University Marine Program, (2008), Boston University, Boston, MA.

- S.E.A. program, cruise C-220, (2008), Sea Education Association, Woods Hole, MA.
- Visiting student for 5 months, (2006), Denmark Technical University, Copenhagen, Denmark.
- Certificate of expert technician in fluvial and coastal measurements, (2006), Centre of Research and Advanced Education for Hydrogeological Risk Prevention (CERAFRI), Lucca, Italy.
- Reviewer for Geophysical Research Letters, Water Resources Research, Continental Shelf Research, Geomorphology, Limnology and Oceanography: Methods.

D. Projects involved in

- VCR 5, Virginia Coast Reserve LTER, (NSF), (2008-present)
- Tidal Flats DRI, (ONR), (2009-2010)
- ETBC Collaborative Research: Feedbacks between nutrient enrichment and intertidal sediments: erosion, stabilization, and landscape evolution, (NSF), (2009-present).

E. Peer-reviewed publications

- Mariotti, G., and S. Fagherazzi, (2011), Asymmetric fluxes of water and sediments in a mesotidal mudflat channel, *Continental Shelf Research*, 31,1, 23-36.
- Mariotti, G., and S. Fagherazzi (2010), A numerical model for the coupled long-term evolution of salt marshes and tidal flats, *J. Geophys. Res.*, 115, F01004.
- Mariotti, G., S. Fagherazzi, P. L. Wiberg, K. J. McGlathery, L. Carniello, and A. Defina, (2010), Influence of storm surges and sea level on shallow tidal basin erosive processes, *J. Geophys. Res.*, 115, C11012.

- Fagherazzi, S., G. Mariotti, J. H. Porter, K. J. McGlathery, and P. L. Wiberg, (2010), Wave energy asymmetry in shallow bays, *Geophys. Res. Lett.*, 37, L24601.

F. Papers under review and other publications

- Mariotti, G., Fagherazzi, S., (2011), Wind waves on a mudflat: the influence of fetch and depth on bottom shear stresses, submitted to *Continental Shelf Research*, Special Issue: Tidal Flats.
- Mariotti, G., Fagherazzi, S., (2011), Channels-tidal flat sediment exchange: the channel spillover mechanism, (accepted with minor revisions) *J. Geophys. Res*.
- Fagherazzi S., Mariotti G., (2011), Bottom Shear Stresses in Runnels Flanking a Mudflat Channel submitted to *J. Geophys. Res*.
- Mariotti, G., N. Lebovitz, (2011), A low dimensional model for shear turbulence in Plane Poiseuille Flow: an example to understand the edge. Proceeding of the 52nd WHOI GFD summer school, shear turbulence: onset and structure.